DECLASSIFIED

[redacted]

2/13

6-15-71

Copy 383

NASA MEMO 12-29-58L

NASA MEMO 12-29-58L

[redacted]

[redacted]

NASA

MEMORANDUM

Declassified by authority of NASA [redacted]
Classification Change Notices No. [redacted] 212
Dated ** [redacted] 31 MAR 1971

EFFECTS OF AFTERBODY SHAPE AND HOT JET EXHAUSTS ON PRESSURES, TEMPERATURES, AND DRAG OF A TWIN-ENGINE FIGHTER-AIRPLANE MODEL HAVING AN OVERHANGING FUSELAGE

By Edwin E. Lee, Jr., and Leland B. Salters, Jr.

Langley Research Center
Langley Field, Va.

[redacted]

[redacted]

NATIONAL AERONAUTICS AND
SPACE ADMINISTRATION
WASHINGTON
January 1959

[redacted]

DECLASSIFIED

[redacted]

NATIONAL AERONAUTICS AND SPACE ADMINISTRATION

MEMORANDUM 12-29-58L

EFFECTS OF AFTERBODY SHAPE AND HOT JET EXHAUSTS ON PRESSURES, TEMPERATURES, AND DRAG OF A TWIN-ENGINE FIGHTER-AIRPLANE MODEL HAVING AN OVERHANGING FUSELAGE*

By Edwin E. Lee, Jr., and Leland B. Salters, Jr.

SUMMARY

An investigation of a twin-engine fighter-airplane model has been conducted in the Langley 16-foot transonic tunnel to determine the effects of afterbody shape and jet operation on drag. Hot turbojet exhausts were simulated with hydrogen peroxide gas generators by using scaled nonafterburning nozzles. Afterbody pressures and temperatures, base drag coefficients, afterbody pressure drag, and pitching moments of the fuselage-tail combination are presented for various conditions within a range of test variables including Mach numbers from 0.85 to 1.05, angles of attack of 0° and 4°, and ratios of total jet pressure to free-stream static pressure from 1 to 7.

The results show that removing the lower portion of the basic afterbody to increase the clearance between the fuselage and the jets increased the drag at subsonic speeds with and without jet operation. Extending the engine compartments and maintaining the geometry in the vicinity of the jet exits similar to the geometry of the basic model had little effect on afterbody drag. At subsonic speeds, jet operation generally increased the afterbody pressures but decreased the base pressures of each configuration. Because of the compensating nature of these effects, no significant overall drag penalties resulted from jet operation.

INTRODUCTION

An extensive investigation of the jet interference phenomena associated with a powered model of a long range, twin-jet fighter airplane

---

*Title, Unclassified.

[redacted]

having an overhanging fuselage has been conducted in the Langley 16-foot transonic tunnel. The purpose of this investigation was twofold: to provide an understanding of the nature of the jet interference effects associated with this configuration; and, to consider possible means of reducing the drag level at high subsonic cruising speeds. One phase of the investigation, which was concerned with drag reduction, considered changes in the fuselage-tail forces and moments obtained by modifying the fuselage ahead of the jet exits and is reported in reference 1.

The present paper is concerned with the extent to which the aerodynamic forces and moments are affected by the complex fuselage shape in the region behind the jet exits, and with establishing an understanding of the relationship between this shape and the afterbody pressures and temperatures resulting from jet operation. Again, as in reference 1, the subsonic cruising condition will be emphasized in the consideration of the effects of geometry and engine operation on drag.

Tests of the powered, twin-jet, fighter model incorporating three different overhanging afterbodies were conducted through the Mach number range from 0.85 to 1.05 at angles of attack of 0° and 4°, with the jet total-pressure ratio varying from 1.0 to 7 at a constant jet stagnation temperature of approximately 1,360° F. Fuselage-tail forces and moments and surface pressures and temperatures in the vicinity of the jet exits were measured. The average Reynolds number based on the wing mean aerodynamic chord was approximately 5.0×10^6.

SYMBOLS

A	axially projected area
A_b	base area, $A_e - A_j$, sq ft
$C_{D,a}$	afterbody drag coefficient, $\frac{1}{S}\int C_p \, dA$
$C_{D,b}$	base drag coefficient, $\bar{C}_{p,b}A_b/S$
$\Delta C_{D,j}$	incremental drag coefficient due to jet operation, $(C_{D,a} + C_{D,b})_{\text{jet on}} - (C_{D,a} + C_{D,b})_{\text{jet off}}$
C_m	fuselage-tail pitching-moment coefficient, $\frac{M_Y}{q_\infty S\bar{c}}$

[redacted]

$\Delta C_{m,j}$	incremental fuselage-tail pitching-moment coefficient due to jet operation, $C_{m,\text{jet on}} - C_{m,\text{jet off}}$
C_p	pressure coefficient, $\frac{p_l - p_\infty}{q_\infty}$
$\bar{C}_{p,b}$	average base pressure coefficient
$\bar{c}$	mean aerodynamic chord of basic wing (fig. 2), in.
d	diameter, in.
M	Mach number
M_Y	fuselage-tail pitching moment about $0.286\bar{c}$, in-lb
p	static pressure, lb/sq ft
p_t	total pressure, lb/sq ft
q	dynamic pressure, lb/sq ft
S	basic wing area, sq ft
T	total temperature, $^{\circ}$F
t	measured model surface temperature, $^{\circ}$F
x	longitudinal distance from shroud exit, positive rearward, in.
y	lateral distance from model plane of symmetry, positive to right looking forward, in.
z	vertical distance from plane containing jet center lines, positive upward, in.
α	angle of attack of fuselage reference line (fig. 2), deg
β	boattail angle, deg
δ	nozzle to shroud exit spacing, in.
ϕ	meridian angle at engine base (fig. 3), deg

[redacted]

θ	temperature parameter, $\dfrac{\left(t_l - T_\infty\right)}{\left(T_j - T_\infty\right)}$

Subscripts:

b	base
e	shroud exit
j	jet
l	local
∞	free stream

APPARATUS AND METHODS

Wind Tunnel and Support System

The tests were conducted in the Langley 16-foot transonic tunnel, which is a single-return atmospheric wind tunnel having an octagonal, slotted test section and continuous air-exchange capabilities.

The model was supported at the wing tips by the bifurcate sting shown in figures 1 and 2, with the wing acting as an integral part of the support system. A strain-gage balance connected to the wing center section measured the forces and moments of the fuselage-tail component only. Strength requirements necessitated the reduction in basic wing span indicated in figure 2.

Models

Details of the basic twin-jet fighter-model configuration used in this investigation are given in figure 2. The model was constructed primarily of steel with plastic overlays used in the nose-canopy section and on parts of the wing surface near the root. The inlets were faired to streamline contours without altering the plan-form geometry of the normally open inlet. In order to permit the fuselage-tail component to deflect the six-component strain-gage balance, a clearance gap, filled with a flexible spongy material, was maintained between the wing and fuselage.

Two jet simulators of the type shown in figure 7(a) of reference 2 were supported in the fuselage from the center section of the wing

[redacted]

(support system). The scaled nonafterburning nozzles, used throughout the investigation, had a discharge coefficient of 0.98 typical of sonic nozzle operation. No secondary air flow was used in this investigation. Details of the jet exits are shown in figure 3. Also shown in this figure are the flexible seals installed between the simulator tailpipes and the engine shrouds to prevent flow into the engine bases in the event of air leakage through joints in the forward portion of the fuselage.

The influence of the geometry of the fuselage overhang on the fuselage-tail forces and moments and the relationship between this geometry and the jet effects were investigated by modifying the basic model configuration as shown in figure 4. In order to simplify terminology, the lower portion of the fuselage overhang is referred to as the afterbody throughout the remainder of the text.

Configuration I is representative of the basic twin-jet fighter and is used as the standard of comparison in discussing the results. Configuration II was obtained from configuration I by cutting away a portion of the afterbody profile between the engine exhausts for the purpose of increasing the radial clearance between the afterbody surface and jet boundaries. The resulting profile is indicated by the dashed curve in figure 4.

Configuration III (identical to basic configuration of ref. 1) is representative of an extended tailpipe version of the airplane and was obtained by adding an extension to the engine compartment section of the basic model which resulted in a shortening of the afterbody. The engine shrouds were displaced 3 inches to the rear, and the geometry of the afterbody surface in the vicinity of the exits was held generally similar to that of configuration I. The relative position of the shroud and nozzle exits, shown in figure 3, was maintained by extending the simulator tailpipes. The overall model length was identical for all configurations.

Photographs showing the complex geometry of the various afterbodies are presented in figure 5. The vertical ridge at the downstream end of the shroud cutout indicates the approximate position of the shroud exit relative to the afterbody. In photograph 5(b), the comparatively shorter length of the afterbody portion of configuration III is obvious. The general similarity of the afterbody profiles of configurations I and III in the vicinity of the jet exits may also be seen. The cross-sectional area distribution of the complete model configurations and of the afterbody sections alone are presented in figures 6 and 7, respectively.

[redacted]

Instrumentation

For all configurations tested, the left engine shroud and base and the left side of the afterbody were instrumented with pressure orifices at the angular locations shown in figure 3. A limited number of thermocouples, peened into the model surface, were also included in some of the orifice rows on the afterbody. In the photographs of figure 5, the afterbody instrumentation is shown for rows at $\phi = 30^\circ$ and 90° and at the fuselage bottom center line, with the black circular and diamond symbols indicating orifices and thermocouples, respectively. Coordinates of the individual orifice and thermocouple locations on the shroud, base, and afterbody of each configuration are presented in tables I, II, and III. Pressures were measured with fast response electrical transducers and mercury manometers. Fuselage-tail forces and moments were measured by an internal strain-gage balance, and a strain-gage pendulum-type attitude indicator was used to measure model angle of attack. Electrical outputs of the pressure transducers, thermocouples, and balance were transmitted to recording oscillographs; and pressure data, taken on mercury manometers, were photographically recorded.

Tests

The investigation was conducted at Mach numbers of 0.85, 0.95, 1.00, and 1.05 and at angles of attack of 0° and 4° with a corresponding Reynolds number variation of 4.67×10^6 to 5.45×10^6. At each test Mach number and angle of attack, the jet simulator units were operated through a cycle of jet pressure ratios of 1, 3, 5, and 1, where a value of 1 has been assigned to the initial and final jet-off conditions. At Mach numbers of 1.00 and 1.05 a jet pressure ratio of 7 was included in the cycle. The jet stagnation temperature was approximately 1,360° F throughout the investigation.

Data Reduction and Accuracies

The data obtained from oscillograph records and photographic film were converted to punch cards and reduced to coefficient form by machine computation. On the basis of the known characteristics of the instrumentation and data reduction procedures, the data are believed to be accurate to within the following limits:

M_∞	±0.005
α, deg	±0.1
C_p	±0.02
$p_{t,j}/p_\infty$	±0.2
$C_{D,a}$	±0.0005
$C_{D,b}$	±0.0003

[redacted]

The drag-coefficient accuracies quoted apply to values obtained by pressure integrations. In the particular phase of the overall investigation reported herein, fuselage-tail drag measurements were impaired by both balance temperature compensation problems (ref. 1) and a lack of some of the internal pressure measurements required in the determination of external drag. Consequently, only fuselage-tail pitching-moment data are presented, and no specific accuracy can be quoted.

The effects of support-system interference on the data have been discussed previously in references 1 and 3. It is believed that interference effects on any given configuration are small and become insignificant with regard to configuration comparisons.

RESULTS

The results of the investigation are presented first in terms of pressure data measured on the engine shrouds, bases, and afterbodies, with the effects of fuselage shape and jet operation summarized separately for each of these regions. Relative drag performance of the different afterbodies is then established by using integrated pressure data. Individual jet effects on the shroud, base, and afterbody are used to indicate the general nature of the jet effects on the drag of each configuration as a whole. A limited amount of balance data is also presented to illustrate the influence of fuselage geometry and jet exhaust on fuselage-tail pitching moment.

Manometer data from configuration III are presented in figure 8 to show the typical shape of the longitudinal pressure distributions and the effects of Mach number and angle of attack on the shrouds. Longitudinal pressure distributions (manometer data) on the shrouds of the different configurations are compared in figure 9 at selected cruising conditions ($M = 0.85$, $\alpha = 4^\circ$) with the jets off (jet pressure ratio of 1.0) and with the jets operating at a pressure ratio of 2.7. In order to illustrate jet effects on the shrouds above Mach number 0.85, pressures measured by electrical transducers on both the shroud and the adjacent fuselage immediately upstream of the exit are plotted against angular position in figure 10 for each configuration. Individual base pressures (see fig. 3) for the different configurations are presented in figure 11, and averages of the individual values are plotted against pressure ratio in figure 12 to summarize the influence of geometry and jet operation on the base region over the full Mach number, angle-of-attack, and jet-pressure-ratio range. In figures 13 to 15 basic afterbody pressure data for the three configurations are presented for the full range of test variables. In order to illustrate more readily the effect of model attitude on afterbody pressures, a limited amount of data taken for configuration III at $\alpha = 8^\circ$ is presented in figure 16.

[redacted]

Pressure distributions from the different afterbodies are compared in figure 17 to show the effect of the fuselage modifications. The influence of jet pressure ratio on afterbody pressures is illustrated in figure 18. Afterbody surface-temperature data, indicating the region of maximum heating, are given in figures 19 and 20 for specific cruising conditions. A final summary of the influence of geometry and jet operation on the base and afterbody drag, and the fuselage-tail pitching moment is provided by figures 21, 22, and 23.

DISCUSSION

Pressure Distributions

Aside from a general decrease in pressure with increasing Mach number, which is typical of transonic speeds, the engine shroud pressure distributions of figure 8 indicate that pressure recovery was incomplete. This defect resulted in the negative base annulus pressure coefficients of figures 11 and 12 (jet off) and these values, combined with the large base area associated with twin-engine nonafterburning operation, could be expected to have a significantly detrimental effect from the standpoint of cruise drag. Of additional interest in figure 8 is the marked reduction in pressure at the faired step (see figs. 1(c) and 3), which forms the transition from the sloping engine compartment surface to the cylindrical section of the shrouds. In view of the dependence of pressure recovery and the resulting level of base annulus pressures on the surface geometry in the region ahead of the exits (see ref. 1), it is suspected that the faired step may contribute somewhat to the detrimental conditions existing in the vicinity of the base.

The influence of fuselage geometry on the shroud pressure distributions at selected cruising conditions is illustrated in figure 9. The most significant difference occurred between configurations I and III. The more negative pressure values of configuration III, indicative of reduced pressure recovery, apparently resulted from the increase in fuselage cross-sectional area corresponding to the extension of the engine compartments, which reduced the local effective boattailing of the fuselage ahead of the shrouds. (See fig. 6 and ref. 1.) The effect of jet operation (figs. 9 and 10) was found to be generally favorable over the Mach number and jet-pressure-ratio range with no appreciable increase in shroud pressures indicated for pressure ratios less than 5 at subsonic speeds and less than 7 at supersonic speeds.

Figure 12 shows that fuselage geometry had no marked effect on the base annulus pressures at subsonic speeds either with or without jet operation. These data also indicate that the jets had an aspirating effect on the base at pressure ratios up to approximately 5 over the

[redacted]

Mach number range. The pressure ratio at which the jet effects tended to become favorable was apparently more dependent on fuselage geometry at supersonic speeds than at subsonic speeds. The occurrence of minimum base annulus pressures at or near a jet pressure ratio of 3 is significant at subsonic speeds since this pressure ratio corresponds to cruising operation.

The basic data of figures 13, 14, and 15 indicate that the distribution of pressures over the afterbodies was generally characterized by negative coefficients immediately downstream of the exits followed by positive values over the rear portion of the afterbody for all test conditions. With increasing Mach number the pressures in the vicinity of the exits experienced the typical transonic variation, increasing slightly up to Mach number 0.95 and decreasing again at supersonic speeds. Increasing the angle of attack to 8° (fig. 16) produced only slight increases in pressure over the afterbodies. In figure 17 the comparison of jet-off pressure distributions for the afterbodies shows that removing the fairing between the exhausts (configuration II) reduced the pressures near the exits and increased the pressures over the rear portion of the afterbody. Because of the bluntness of this afterbody immediately behind the exits (see fig. 7), the decrease in pressure in this region could be expected to have a considerably unfavorable influence on afterbody drag. In general, the pressure coefficients of configuration III were slightly more negative than those of the basic model (configuration I) along most of the afterbody length. The preceding remarks appear to hold generally true during jet operation through a pressure ratio of 5.

In general the effect of jet operation on each afterbody (see fig. 18) was to increase the pressures for a distance of about 3 shroud diameters downstream of the exits for pressure ratios up to 5 at all Mach numbers. Comparison of the data for the three afterbodies shows that the most noticeable differences occurred with configuration II. The pressures over the rear of the configuration II afterbody, in contrast to the others, exhibited a consistent decrease with jet operation at each Mach number; this result indicated that the blunted fairing caused the jets to be drawn toward the afterbody surface. At supersonic speeds and high pressure ratios, the reduction in pressure appearing in the data of configurations I and III at $\frac{x}{d_e} \approx 1$ was eliminated by relieving the afterbody profile. This marked pressure reduction in the vicinity of the exits of configurations I and III is attributed to the aspirating effect of the jets on the afterbody surface. Approximations of the jet boundary shape obtained by using the still-air data of reference 4 indicate that the maximum diameter of the jet bulb occurred in the vicinity of the low pressure peak. This aspirating phenomena is also indicated in references 5 and 6 for twin and single sonic jets

[redacted]

discharging adjacent to an overhanging fuselage at comparable pressure ratios and Mach numbers.

Temperature Distributions

In the process of obtaining the model afterbody temperatures of figures 19 and 20, no attempt was made to provide structural similitude with the prototype. The thermocouples measured the surface temperature of the heavy afterbody shells which varied from 1/2 to 1 inch in thickness. Because of the mass involved, the establishment of temperature equilibrium is doubtful although data obtained with the test conditions maintained constant for the longest possible duration were used in these figures. The data, though necessarily qualitative, afford some indication of the distribution of temperatures along the afterbodies and the location of regions of maximum heating.

Figure 20 shows that modifying the basic afterbody to configuration II failed to produce any significant reduction in the surface temperatures. In view of the increased radial spacing provided by this modification, the more forward location of the region of maximum heating and the existence of elevated temperatures along the entire length of the afterbody indicate that the blunt shape behind the exits caused a considerable displacement of the jets toward the afterbody surface. These results are consistent with differences between the afterbody pressure data of configurations I and II noted previously. The surface temperatures of configuration III were generally lower than those of the basic model. This result is attributed in part to the increased taper in width. In addition, horizontal-tail pressures obtained from other investigations of this model in the 16-foot tunnel showed that a downward change in the local flow direction resulted from the rearward displacement of the shrouds. This change would have tended to keep the jets away from the fuselage by reducing any upward motion of the flow field and the exhaust gases due to the upswept afterbody profile and the model attitude ($\alpha = 4^{\circ}$).

Force Data

The base drag data of figure 21, computed by use of the area ratios and average pressure coefficients of figures 3 and 12, respectively, show the general similarity of the subsonic base drag level for all configurations at a pressure ratio of 3. A comparison of the jet-off values with those at a pressure ratio of 3 for Mach number 0.85 and $\alpha = 4^{\circ}$ indicates that the aspirating effect of the jets increased the base drag of all configurations by approximately 0.0010 so that a total value of about 0.0025 was obtained at cruising conditions.

[redacted]

The drag of each afterbody was obtained for Mach numbers of 0.85 and 0.95 at $\alpha = 4^\circ$ by integrating the pressure data. The results, plotted in figure 22, show that the removal of the fairing between the jets (configuration II) resulted in an increase in afterbody drag at subsonic speeds and that this increase was approximately 0.0015 at the selected cruising conditions. Reducing afterbody length (configuration III) and maintaining the geometry in the vicinity of the exits similar to that of the basic configuration had little effect on afterbody drag. Although the effect of the complete fuselage geometry modification on the overall drag could not be evaluated because of balance difficulties previously mentioned, the data of figure 22 indicate that any major difference in the drag levels of configurations I and III would not be associated with the afterbody section.

Figure 22 also indicates that jet operation had a favorable effect on afterbody drag at subsonic speeds and jet pressure ratios up to 5. Corresponding base drag values are included in the figure to permit a direct comparison of the opposing jet effects on the base and afterbody. At a pressure ratio of 3 for both Mach numbers shown, the favorable effect on the afterbody tended to compensate for all or most of the adverse effect on the base. This tendency is further illustrated by the combined jet effects on the base and afterbody, which are also presented in figure 22 $\left(\Delta C_{D,j}\right)$. These values are believed to be indicative of the overall jet effects on each configuration, since the major influence of the jets was associated with the base and afterbody regions of the model. From consideration of these results and the fact that small favorable effects could also be expected from the engine shrouds and the upper portion of the fuselage, it appears that no significant adverse jet effects were associated with any of the configurations tested, insofar as the subsonic Mach number range was concerned.

Jet-off pitching-moment data measured by the six-component balance (fig. 23) showed very little change between values for configurations I and II but did indicate some noticeable difference between the values for configurations I and III over the entire Mach number range. The latter difference was found from other available data to be due primarily to a change in tail loading with the shrouds moved rearward and indicates that the angularity of the flow field at the rear of the fuselage was altered in such a way as to reduce the effective angle of attack of the tail (nose-up increment, fig. 23). This change in local flow angularity was mentioned previously with regard to afterbody temperatures. The pressure data of figure 17 tend to confirm this slight effect.

Jet operation at subsonic speeds and pressure ratios up to 5 produced small nose-down pitching-moment increments (fig. 23) which were consistent with the positive pressure increments induced on the afterbodies.

[redacted]

SUMMARY OF RESULTS

An investigation of the effects of afterbody shape and simulated turbojet exhaust on the pressures, temperatures, and drag of a twin-jet fighter-type airplane model having an overhanging fuselage showed the following results pertaining to subsonic cruising operating conditions:

1. Cutting away the lower portion of the afterbody to increase the radial spacing between the surface and the jet boundaries increased the afterbody drag. This modification failed to produce any significant reduction in the afterbody surface temperatures which existed on the basic configuration.

2. Extending the engine compartments and maintaining the geometry in the vicinity of the exits similar to that of the basic configuration had little effect on afterbody drag. In general, surface temperatures were considerably reduced from those of the basic configuration.

3. Jet operation increased the pressures on the engine shrouds and afterbody and reduced the pressures in the base annulus of each configuration. Because of the compensating nature of these effects, no significant overall drag penalties resulted from jet operation.

Langley Research Center,
National Aeronautics and Space Administration,
Langley Field, Va., September 11, 1958.

[redacted]

REFERENCES

1. Foss, Willard E., Jr., Runckel, Jack F., and Lee, Edwin E., Jr.: Effects of Boattail Area Contouring and Simulated Turbojet Exhaust on the Loading and Fuselage-Tail Component Drag of a Twin-Engine Fighter-Type Airplane Model. NACA RM L58C04, 1958.

2. Runckel, Jack F., and Swihart, John M.: A Hydrogen Peroxide Turbojet-Engine Simulator for Wind-Tunnel Powered-Model Investigations. NACA RM L57H15, 1957.

3. Norton, Harry T., Jr., and Swihart, John M.: Effect of a Hot-Jet Exhaust on Pressure Distributions and External Drag of Several Afterbodies on a Single-Engine Airplane Model at Transonic Speeds. NACA RM L57J04, 1957.

4. Love, Eugene S., and Grigsby, Carl E.: Some Studies of Axisymmetric Free Jets Exhausting From Sonic and Supersonic Nozzles Into Still Air and Into Supersonic Streams. NACA RM L54L31, 1955.

5. Mitcham, Grady L.: A Summary of the Longitudinal and Lateral Stability and Control Characteristics Obtained From Rocket-Model Tests of a Swept-Wing Fighter-Type Airplane at Mach Numbers From 0.5 to 1.0. NACA RM L56K19, 1957.

6. Cornette, Elden S., and Ward, Donald H.: Transonic Wind-Tunnel Investigation of the Effects of a Heated Propulsive Jet on the Pressure Distributions Along a Fuselage Overhang. NACA RM L56A27, 1956.

[redacted]

[redacted]

TABLE I

COORDINATES OF THERMOCOUPLE AND PRESSURE-ORIFICE LOCATIONS ON CONFIGURATION I

Instrumentation		Model station, in.	y, in.	z, in.	x/d_e
Row	Type*				
Shroud					
$\phi = 180^\circ$	m	66.52	-2.94	-2.91	-2.37
	m	70.27	-2.94	-2.50	-1.43
	m	72.15	-2.94	-2.49	-.96
	m	74.02	-2.94	-2.30	-.50
	m	74.65	-2.94	-2.20	-.34
	t	75.27	-2.94	-2.10	-.18
$\phi = 255^\circ$	m	70.27	-5.35	-0.65	-1.43
	m	72.15	-5.31	-.65	-.96
	m	74.02	-5.14	-.60	-.50
	m	74.65	-5.06	-.57	-.34
	t	75.27	-4.97	-.54	-.18
$\phi = 330^\circ$	m	70.27	-4.20	2.18	-1.43
	m	72.15	-4.18	2.16	-.96
	m	74.02	-4.09	1.99	-.50
	m	74.65	-4.05	1.90	-.34
	t	75.27	-4.00	1.82	-.18
Base					
$\phi = 30^\circ$	t	74.90	-1.99	1.66	-0.28
90°	t	74.90	-1.02	0	-.28
120°	t	74.90	-1.28	-.95	-.28
180°	t	74.90	-2.94	-1.92	-.28
255°	t	74.90	-4.79	-.50	-.28
330°	t	74.90	-3.90	1.66	-.28
Afterbody					
Shoulder	th	76.89	-2.92	3.32	0.22
	th	80.27	-2.55	3.73	1.07
	th	85.28	-2.05	4.27	2.32
	th	90.28	-1.50	4.72	3.57
$\phi = 30^\circ$	t	75.27	-1.81	2.18	-0.18
	t	75.89	-1.80	1.97	-.03
	t	76.53	-1.79	2.02	.13
	th	76.89	-1.75	2.07	.22
	t	77.15	-1.73	2.09	.29
	t	78.40	-1.51	2.29	.60
	t	79.65	-1.52	2.47	.91
	th	80.28	-1.47	2.55	1.07
	t	80.90	-1.42	2.64	1.23
	t	83.40	-1.23	2.99	1.85
	th	85.28	-1.09	3.23	2.32
	t	85.90	-1.05	3.32	2.48
	t	88.40	-.87	3.60	3.10
	th	90.29	-.74	3.84	3.57
	t	90.91	-.71	3.90	3.73
	t	93.40	-.54	4.18	4.35
	t	95.90	-.37	4.48	4.98
	t	98.41	-.20	4.81	5.60
	th	99.02	.01	4.92	5.76
$\phi = 60^\circ$	th	80.28	-0.50	1.46	1.07
	th	85.27	-.31	2.66	2.32
$\phi = 75^\circ$	t	75.25	-0.61	0.66	-0.19
$\phi = 90^\circ$	t	75.89	-0.71	0.00	-.03
	t	76.53	-.71	0.00	.13
	th	76.91	-.67	-.01	.23
	t	77.16	-.63	.01	.29
	t	78.41	-.47	.01	.60
	t	79.66	-.30	.02	.91
	th	80.28	-.23	-.02	1.07
	t	80.90	-.14	0.00	1.23
$\phi = 120^\circ$	t	75.34	-0.86	-1.18	-0.16
	th	76.92	-.89	-1.02	.23
Fuselage bottom center line	t	75.27	-0.01	-1.47	-0.18
	t	75.92	-0.00	-1.35	-.02
	t	76.52	-0.00	-1.24	.13
	t	77.17	-0.00	-1.10	.29
	t	78.41	-0.00	-.85	.60
	t	85.91	.01	2.54	2.48
	th	90.27	.01	3.63	3.57

*t = transducer.
m = manometer.
th = thermocouple.

[redacted]

[redacted]

TABLE II

COORDINATES OF THERMOCOUPLE AND PRESSURE ORIFICE LOCATIONS ON CONFIGURATION II

Instrumentation		Model station, in.	y, in.	z, in.	x/d_e
Row	Type*				
Shroud					
φ = 180°	m	66.52	-2.94	-2.91	-2.37
	m	70.27	-2.94	-2.50	-1.43
	m	72.15	-2.94	-2.49	-.96
	m	74.02	-2.94	-2.30	-.50
	m	74.65	-2.94	-2.20	-.34
	t	75.27	-2.94	-2.10	-.18
φ = 255°	m	70.27	-5.35	-0.65	-1.43
	m	72.15	-5.31	-.65	-.96
	m	74.02	-5.14	-.60	-.50
	m	74.65	-5.06	-.57	-.34
	t	75.27	-4.97	-.54	-.18
φ = 330°	m	70.27	-4.20	2.18	-1.43
	m	72.15	-4.18	2.16	-.96
	m	74.02	-4.09	1.99	-.50
	m	74.65	-4.05	1.90	-.34
	t	75.27	-4.00	1.82	-.18
Base					
φ = 30°	t	74.90	-1.99	1.66	-0.28
90°	t	74.90	-1.02	0	-.28
120°	t	74.90	-1.28	-.95	-.28
180°	t	74.90	-2.94	-1.92	-.28
255°	t	74.90	-4.79	-.50	-.28
330°	t	74.90	-3.90	1.66	-.28
Afterbody					
Shoulder	th	76.92	-2.95	3.85	0.23
	th	80.27	-2.55	4.52	1.07
	th	85.29	-1.92	4.84	2.32
φ = 30°	t	75.23	-1.70	2.06	-0.19
	t	75.90	-1.77	1.97	-.02
	t	76.51	-1.39	2.29	.13
	th	76.92	-1.37	2.51	.23
	t	77.18	-1.36	2.58	.30
	t	78.42	-1.29	2.82	.60
	t	79.66	-1.17	2.96	.91
	th	80.27	-1.12	3.04	1.07
	t	80.91	-1.07	3.13	1.23
	t	83.41	-.94	3.49	1.85
	th	85.29	-.75	3.68	2.32
	t	85.92	-.68	3.76	2.48
	t	88.41	-.51	4.06	3.10
	th	90.27	0	4.19	3.57
	t	90.91	-.32	4.41	3.73
	t	93.41	-.13	4.79	4.35
	t	95.91	0	5.23	4.98
	t	98.39	0	5.64	5.60
	th	99.07	0	5.74	5.77
	t	99.65	0	5.84	5.91
φ = 60°	th	76.92	-0.39	1.34	0.23
	th	80.27	-.03	1.87	1.07
φ = 75°	t	75.25	-0.58	0.51	-0.19
φ = 90°	t	75.90	-0.74	-0.09	-0.02
	t	76.52	-.16	-.11	.13
φ = 120°	t	75.27	-0.83	-1.16	-0.18
Fuselage bottom center line	t	75.29	0	-1.48	-0.18
	t	75.92	.01	-1.37	-.02
	t	76.54	.01	-1.24	.13
	t	77.17	0	-1.12	.29
	t	80.96	-.03	2.06	1.24
	t	83.39	-.04	2.71	1.85
	th	85.29	0	3.14	2.32
	t	85.91	0	3.29	2.48

*t = transducer.
m = manometer.
th = thermocouple.

[redacted]

TABLE III

COORDINATES OF THERMOCOUPLE AND PRESSURE ORIFICE LOCATIONS ON CONFIGURATION III

Instrumentation		Model station, in.	y, in.	z, in.	x/d_e
Row	Type*				
Shroud					
ϕ = 180°	m	69.52	-2.94	-2.91	-2.37
	m	73.27	-2.94	-2.50	-1.43
	m	75.15	-2.94	-2.49	-.96
	m	77.02	-2.94	-2.30	-.50
	m	77.65	-2.94	-2.20	-.34
	t	78.27	-2.94	-2.10	-.18
ϕ = 255°	m	73.27	-5.35	-0.65	-1.43
	m	75.15	-5.31	-.65	-.96
	m	77.02	-5.14	-.60	-.50
	m	77.65	-5.06	-.57	-.34
	t	78.27	-4.97	-.54	-.18
ϕ = 330°	m	73.27	-4.20	2.18	-1.43
	m	75.15	-4.18	2.16	-.96
	m	77.02	-4.09	1.99	-.50
	m	77.65	-4.05	1.90	-.34
	t	78.27	-4.00	1.82	-.18
Base					
ϕ = 30°	t	77.90	-1.99	1.66	-0.28
90°	t	77.90	-1.02	0	-.28
120°	t	77.90	-1.28	-.95	-.28
180°	t	77.90	-2.94	-1.92	-.28
255°	t	77.90	-4.79	-.50	-.28
330°	t	77.90	-3.90	1.66	-.28
Afterbody					
Shoulder	th	79.89	-2.50	3.02	0.22
	th	83.27	-2.12	3.24	1.07
ϕ = 30°	t	73.26	-1.62	2.19	-1.44
	t	78.26	-1.73	2.02	-.19
	t	78.90	-1.85	1.87	-.03
	t	79.53	-1.80	1.90	.13
	th	79.89	-1.77	1.96	.22
	t	80.15	-1.75	1.99	.29
	t	81.40	-1.64	2.17	.60
	t	82.65	-1.54	2.36	.91
	th	83.27	-1.49	2.46	1.07
	t	83.90	-1.43	2.55	1.23
	t	86.39	-1.25	2.93	1.85
	th	88.29	-1.05	3.09	2.32
	t	88.91	-1.03	3.14	2.48
	t	91.40	-.86	3.56	3.10
	th	93.28	-.73	3.78	3.57
	t	93.91	-.66	3.86	3.73
	t	96.41	-.48	4.18	4.35
	t	98.90	-.28	4.53	4.98
	th	99.03	0	4.40	5.01
ϕ = 60°	th	83.27	-0.48	1.29	1.07
ϕ = 75°	t	78.25	-0.61	0.56	-0.19
ϕ = 90°	t	78.89	-0.72	-0.06	-0.03
	t	79.52	-.71	-.08	.13
	th	79.89	-.67	-.07	.22
	t	80.15	-.64	-.07	.29
	t	81.40	-.48	-.08	.60
	t	82.65	-.33	-.08	.91
ϕ = 120°	t	78.26	-0.84	-1.29	-0.18
Fuselage bottom center line	t	78.28	-0.01	-1.55	-0.18
	t	78.89	.01	-1.43	-.03
	t	79.51	0	-1.32	.13
	th	79.89	0	-1.24	.22
	t	80.15	.01	-1.19	.29
	t	81.40	.01	-.93	.60
	th	83.27	0	-.51	1.07
	t	83.90	.01	-.28	1.23
	th	88.29	-.02	2.25	2.32
	t	88.93	0	2.48	2.48

*t = transducer.
m = manometer.
th = thermocouple.

[redacted]

DECLASSIFIED

[redacted]

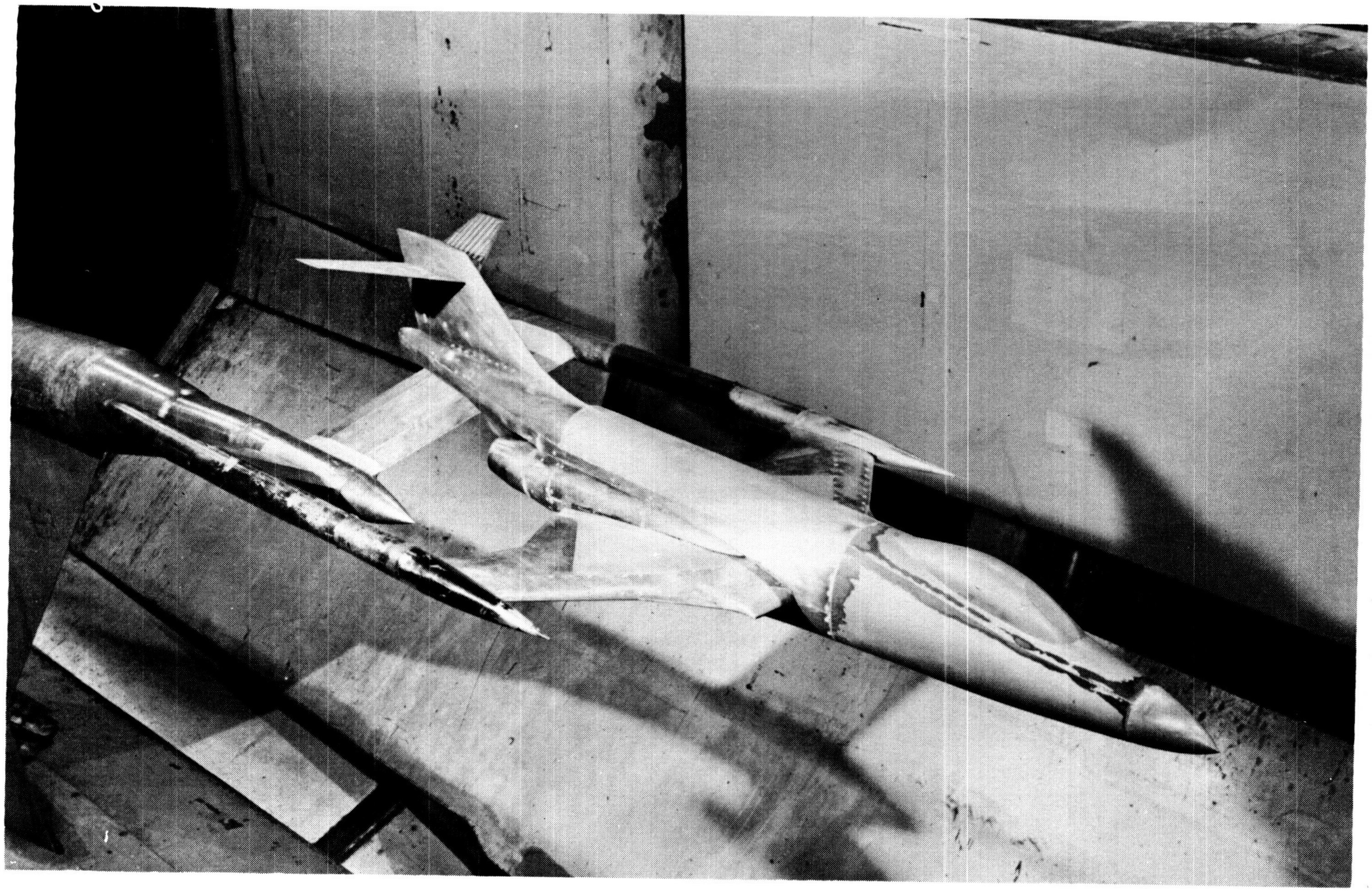

(a) Three-quarter front view. L-95566

Figure 1.- Typical installation of twin jet-exit model and bifurcate sting-support system in tunnel test section.

[redacted]

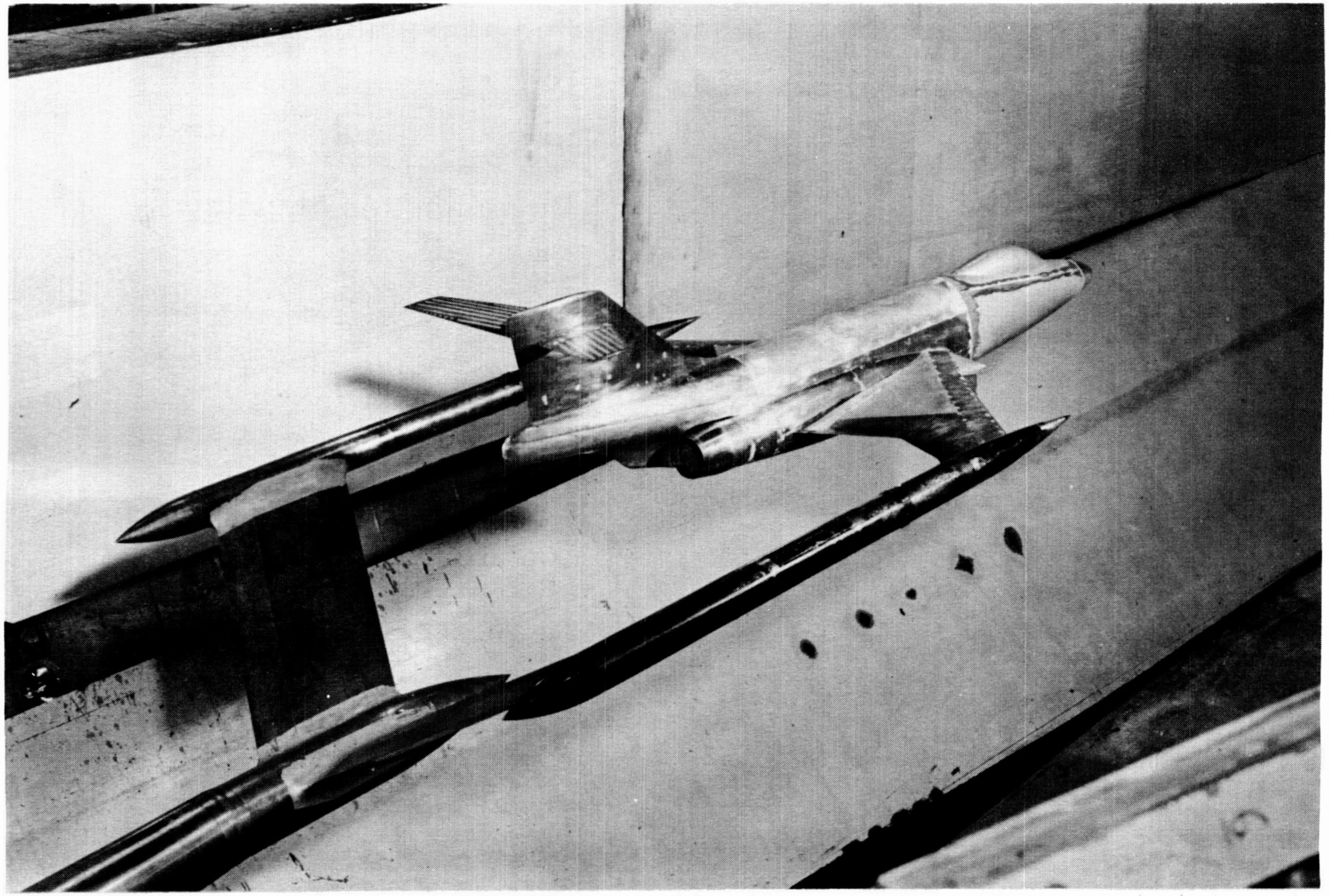

(b) Three-quarter rear view. L-95567

Figure 1.- Continued.

[redacted]

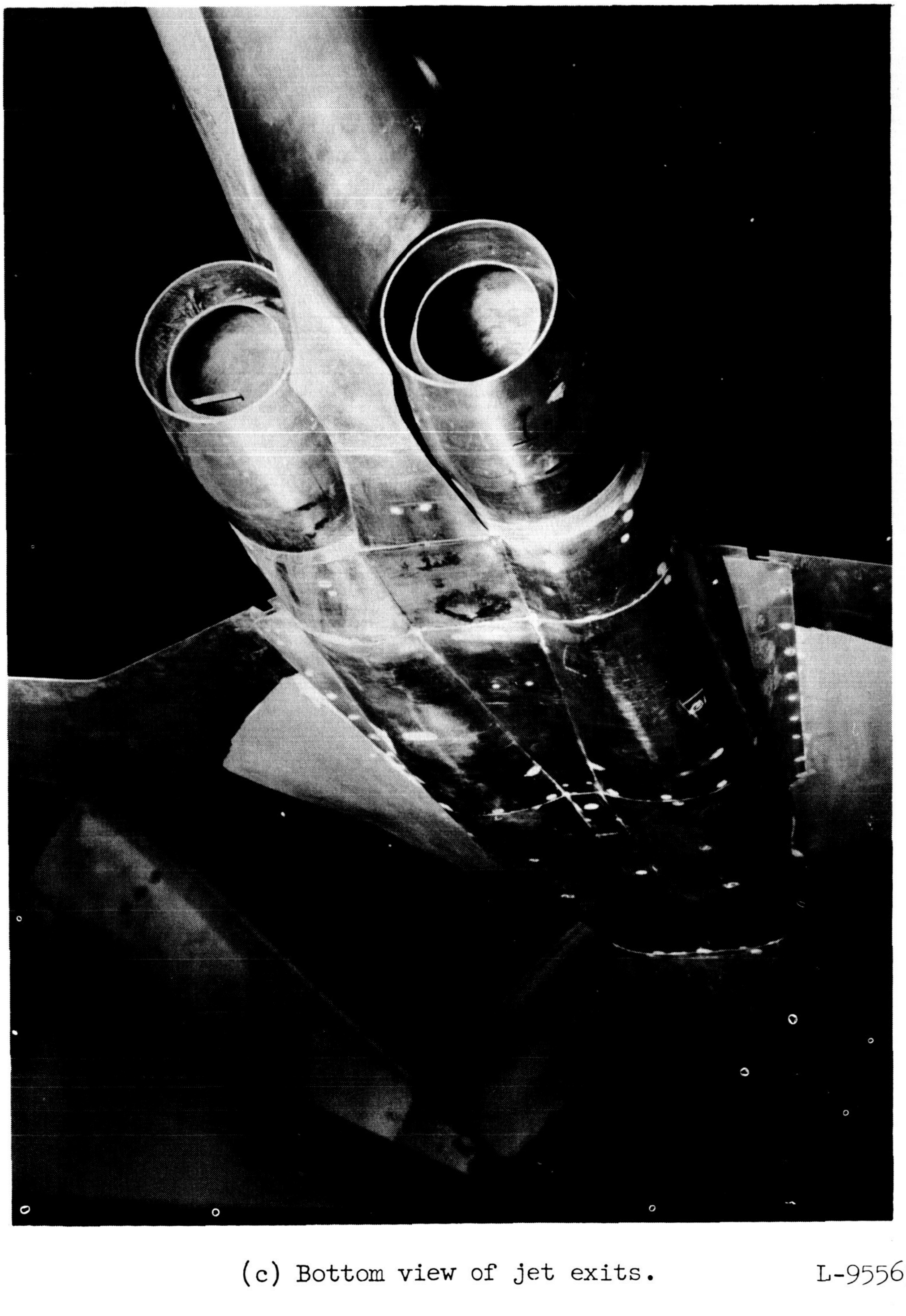

(c) Bottom view of jet exits. L-95565

Figure 1.- Concluded.

[redacted]

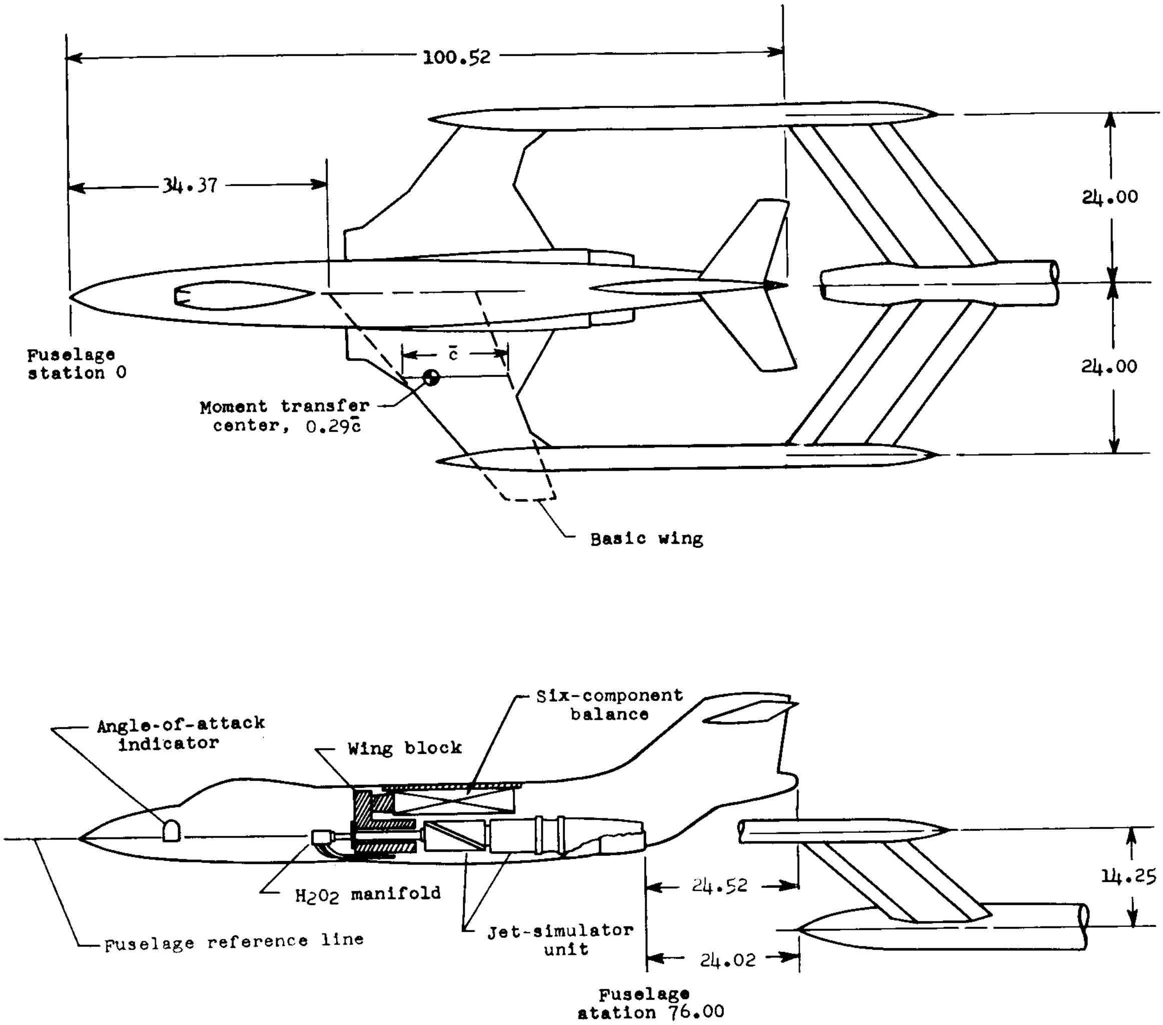
100.52
34.37
24.00
24.00
Fuselage station 0
c̄
Moment transfer center, 0.29c̄
Basic wing
Angle-of-attack indicator
Wing block
Six-component balance
H_2O_2 manifold
Fuselage reference line
Jet-simulator unit
24.52
24.02
14.25
Fuselage station 76.00

ITEM	WING, BASIC (SHOWN BY DASHED LINES)	HORIZONTAL TAIL	VERTICAL TAIL
Area, sq ft	5.75	1.17	1.18[2]
Span, ft	4.95	1.97	0.94
Aspect ratio	4.28	3.30	
Mean aerodynamic chord, ft	1.28	0.62	1.46[2]
Taper ratio	0.28	0.46	
Incidence angle, deg	1.00	0.00	
Dihedral angle, deg	0.00	10.00	
Sweepback of leading edge, deg	41.12	39.80	52.00
Sweepback of trailing edge, deg	19.42	20.93	16.60
Root airfoil section	NACA 65A007[1]	65A007	65A007
Tip airfoil section	NACA 65A006[1]	65A006	65A007

[1] The wing airfoil sections were modified forward of the 16.04-percent-chord line by extending the chord 5 percent and incorporating 1.67 percent positive camber.

[2] Basic, excluding dorsal.

Figure 2.- Sketch of basic model and geometrical details. All dimensions are in inches unless otherwise noted.

[redacted]

Exit variables	Configuration I	Configuration II	Configuration III
Shroud exit sta.	76.000	76.000	79.000
d_e	3.985	3.985	4.001
d_j	2.858	2.858	2.833
δ	.610	.610	.640
A_b/S	.01461	.01461	.01514

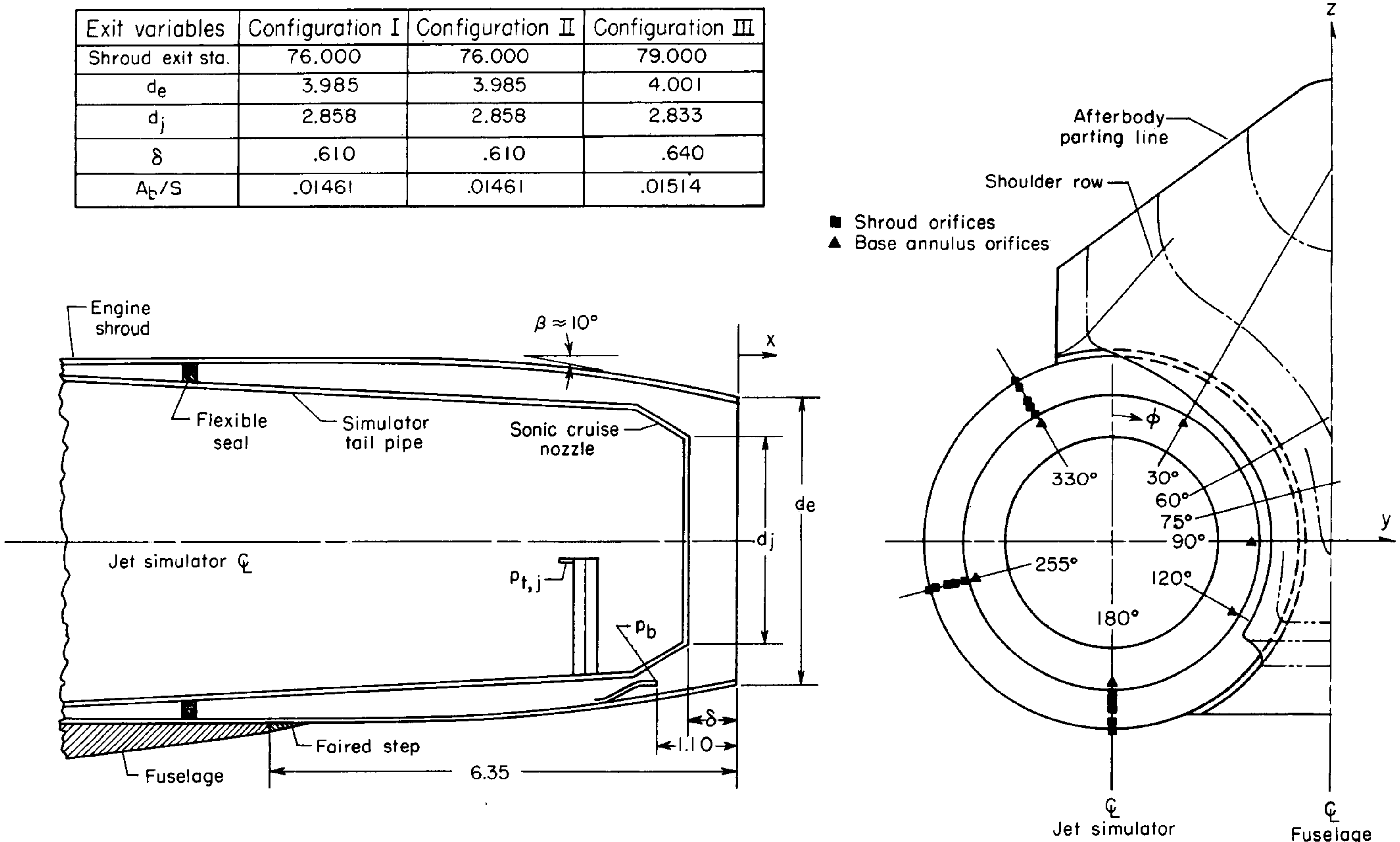

Afterbody parting line
Shoulder row
■ Shroud orifices
▲ Base annulus orifices
z
y
ϕ
330°
30°
60°
75°
90°
255°
120°
180°
℄ Jet simulator
℄ Fuselage
Engine shroud
$\beta \approx 10°$
x
Flexible seal
Simulator tail pipe
Sonic cruise nozzle
de
dj
Jet simulator ℄
$p_{t,j}$
p_b
δ
1.10
Faired step
Fuselage
6.35

Note: Afterbody instrumentation located at shoulder; ϕ = 30°, 60°, 75°, 90°, and 120°; and fuselage center line. For orifice and thermocouple coordinates, see Tables I, II, and III.

Figure 3.- Jet exit geometry and typical arrangement of pressure instrumentation. Base area ratios are given for two engines. All dimensions are in inches unless otherwise noted.

[redacted]

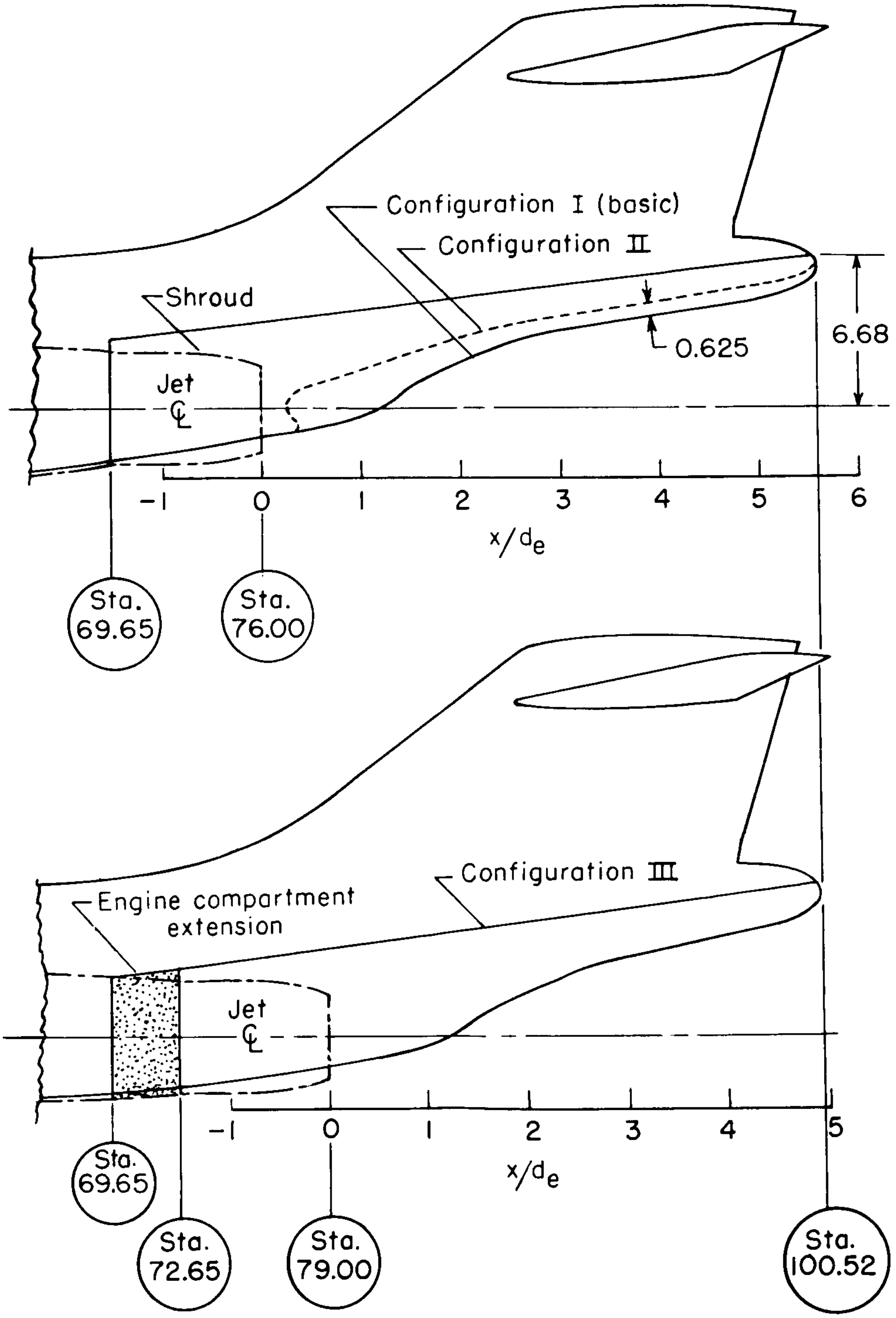
Configuration I (basic)
Configuration II
Shroud
Jet
℄
0.625
6.68
-1
0
1
2
3
4
5
6
x/d_e
Sta. 69.65
Sta. 76.00
Configuration III
Engine compartment extension
Jet
℄
-1
0
1
2
3
4
5
x/d_e
Sta. 69.65
Sta. 72.65
Sta. 79.00
Sta. 100.52

Figure 4.- Sketch showing the fuselage modifications investigated.

[redacted]

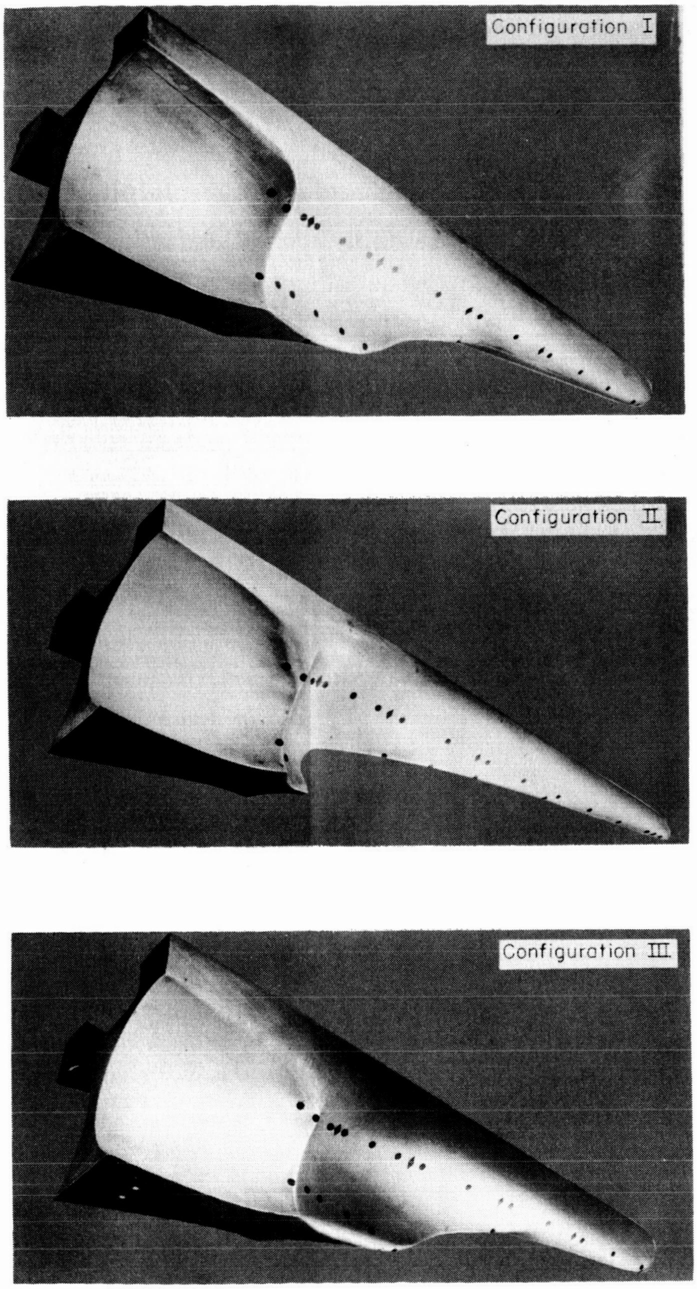
Configuration I
Configuration II
Configuration III

(a) Three-quarter bottom view. L-58-2559

Figure 5.- Photographs of the three afterbodies. Circular and diamond symbols indicate pressure orifice and thermocouple locations, respectively. Orifice rows (top to bottom) are for $\phi = 30^\circ$, 90° and fuselage bottom center line.

[redacted]

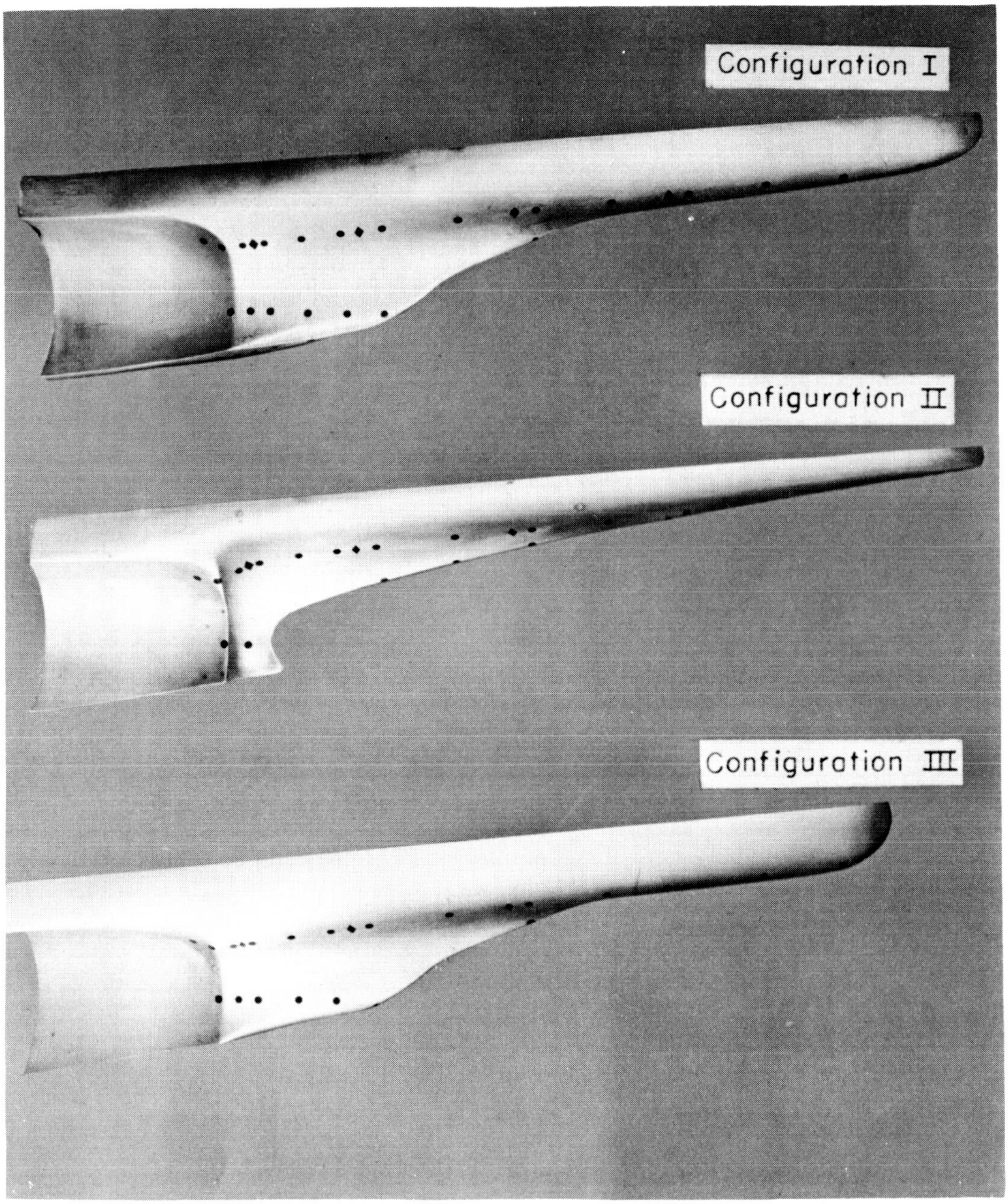
Configuration I
Configuration II
Configuration III

(b) Side view. L-58-382.1

Figure 5.- Concluded.

[redacted]

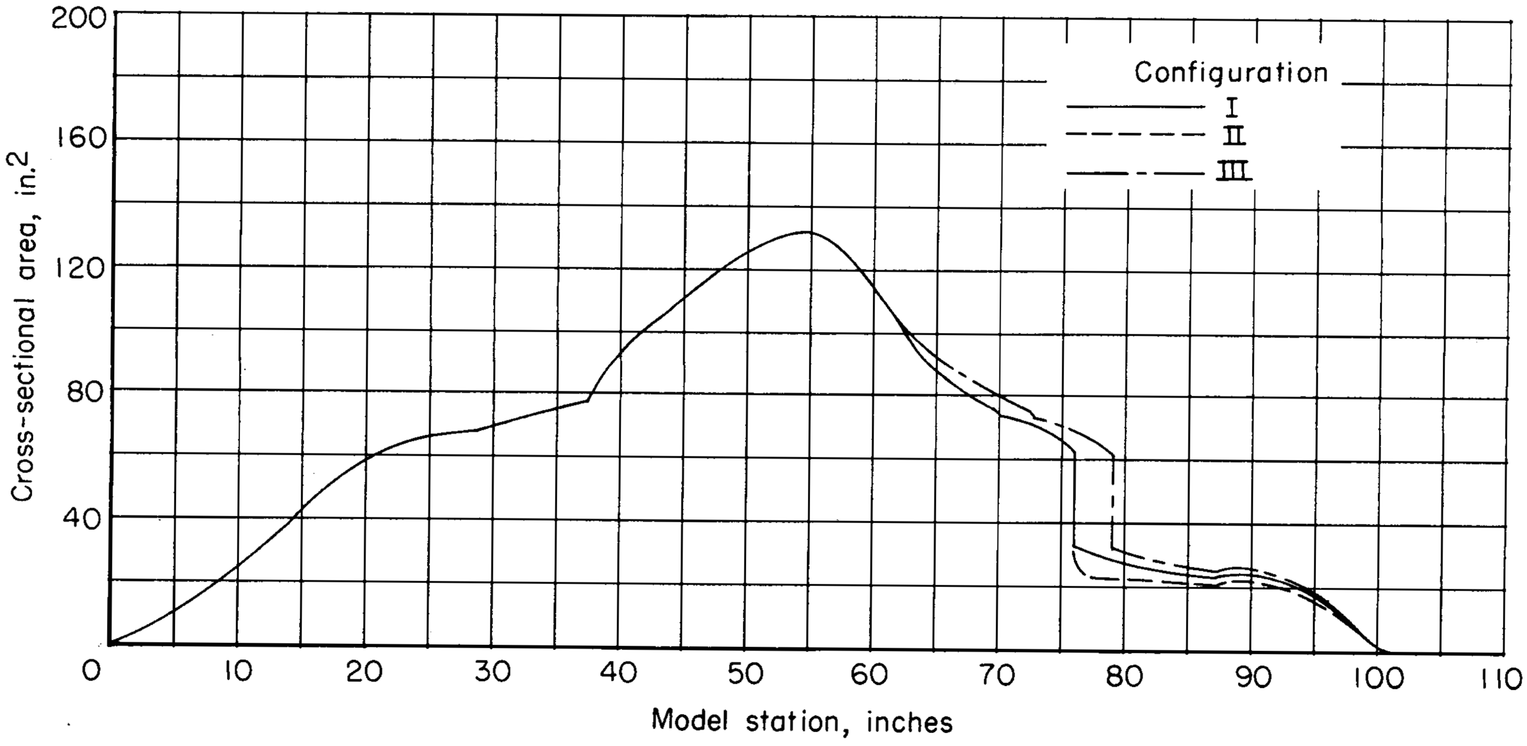

Figure 6.- Model cross-sectional area distributions.

[redacted]

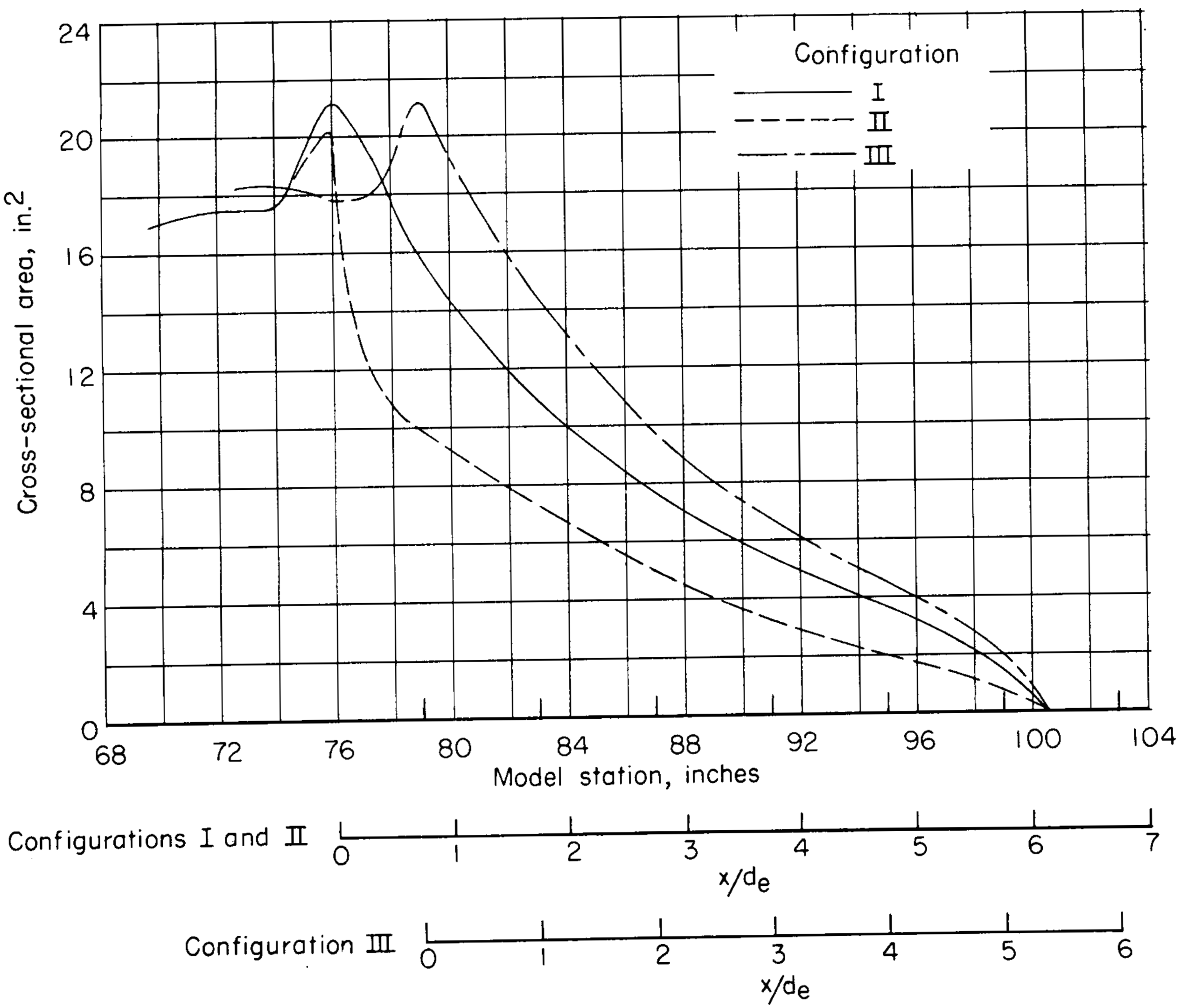

Figure 7.- Afterbody cross-sectional area distribution.

[redacted]

DECLASSIFIED

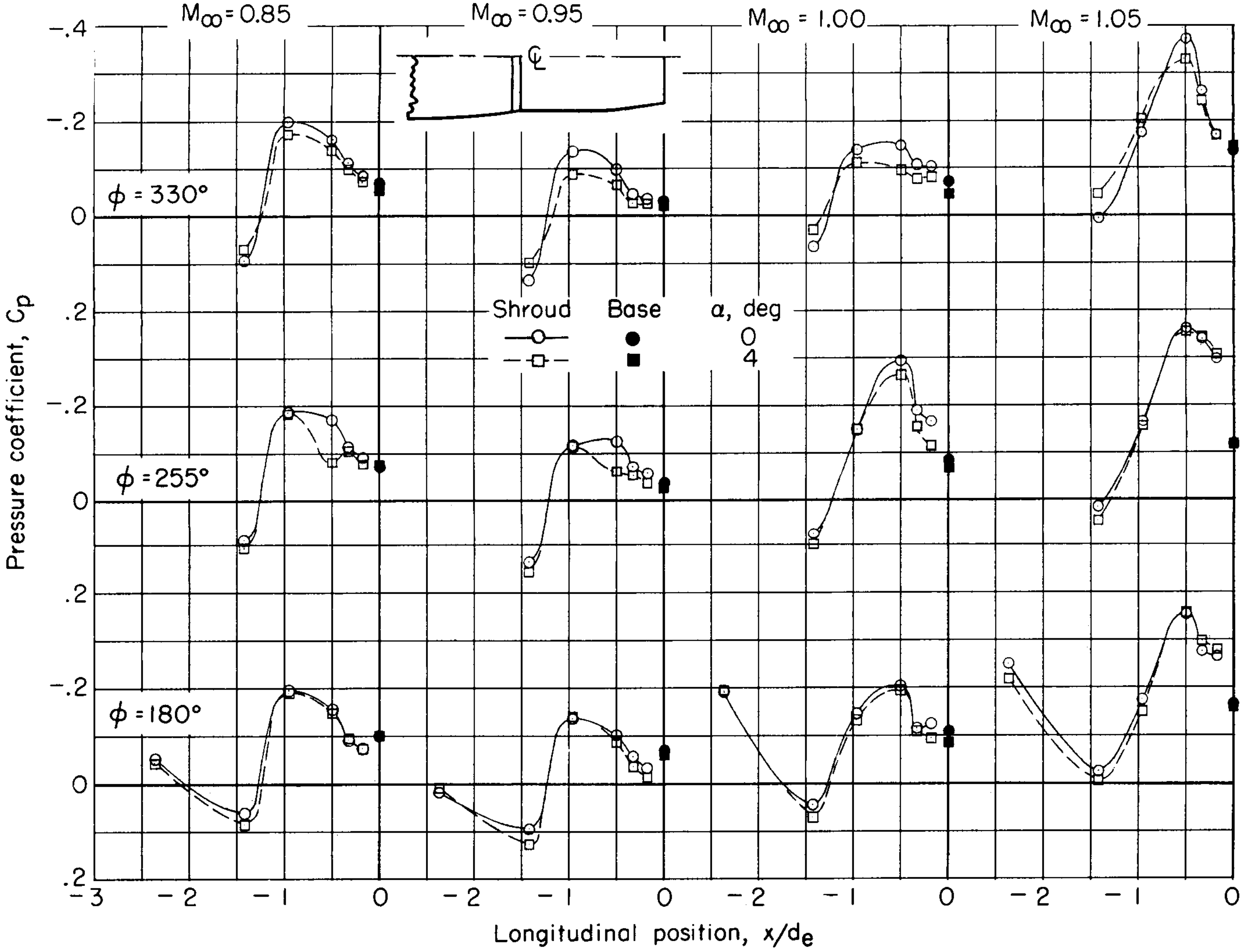

Figure 8.- Effect of Mach number and angle of attack on engine shroud pressure distributions. Configuration III; jets off.

[redacted]

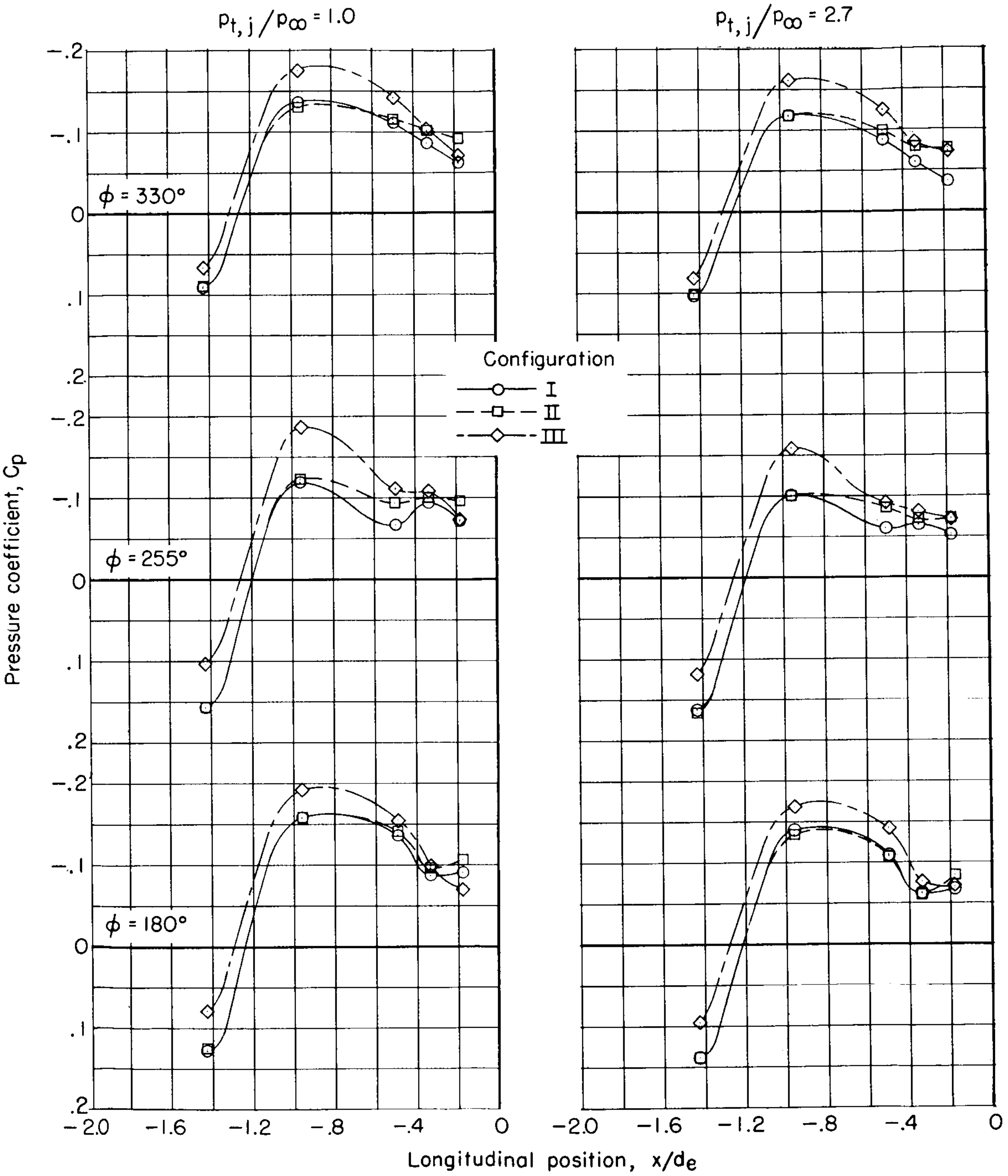

Figure 9.- Comparison of engine-shroud longitudinal pressure distributions of the three model configurations with and without jet operation. M_{∞} = 0.85; α = 4°.

[redacted]

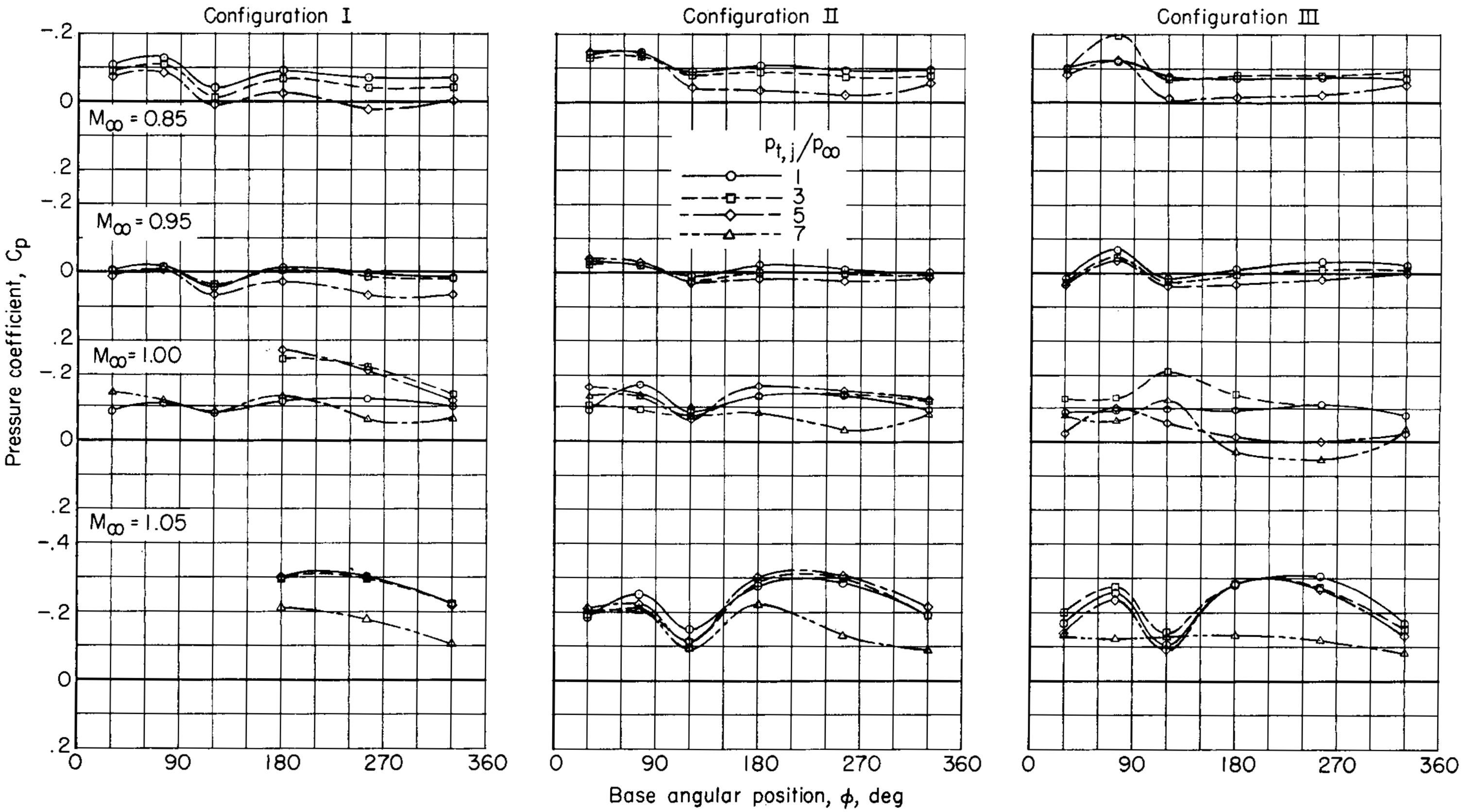

Figure 10.- Effect of jet operation on shroud pressures near base. $x/d_e = -0.18$; $\alpha = 4^\circ$.

[redacted]

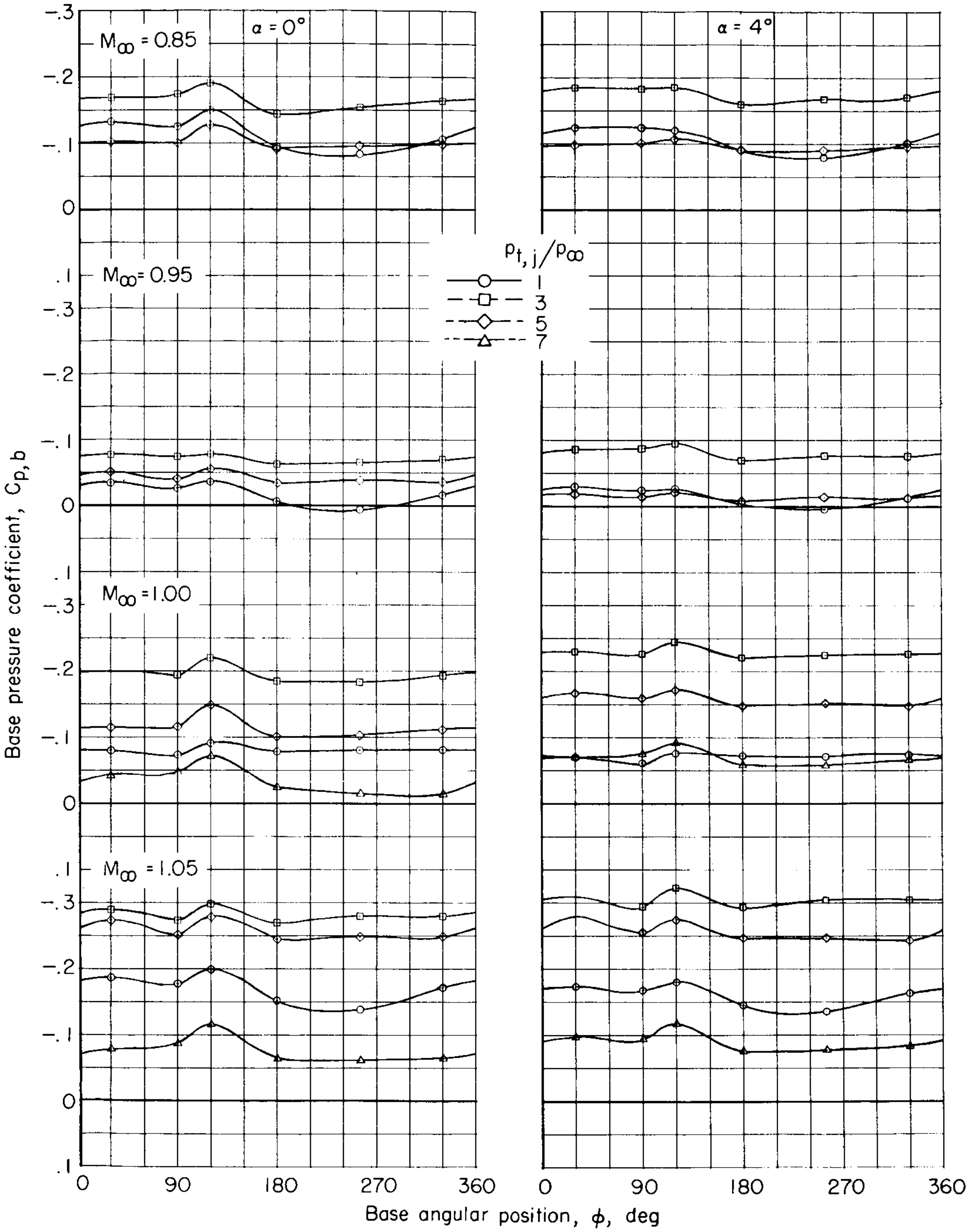

(a) Configuration I.

Figure 11.- Variation of circumferential base pressure distribution with jet pressure ratio.

[redacted]

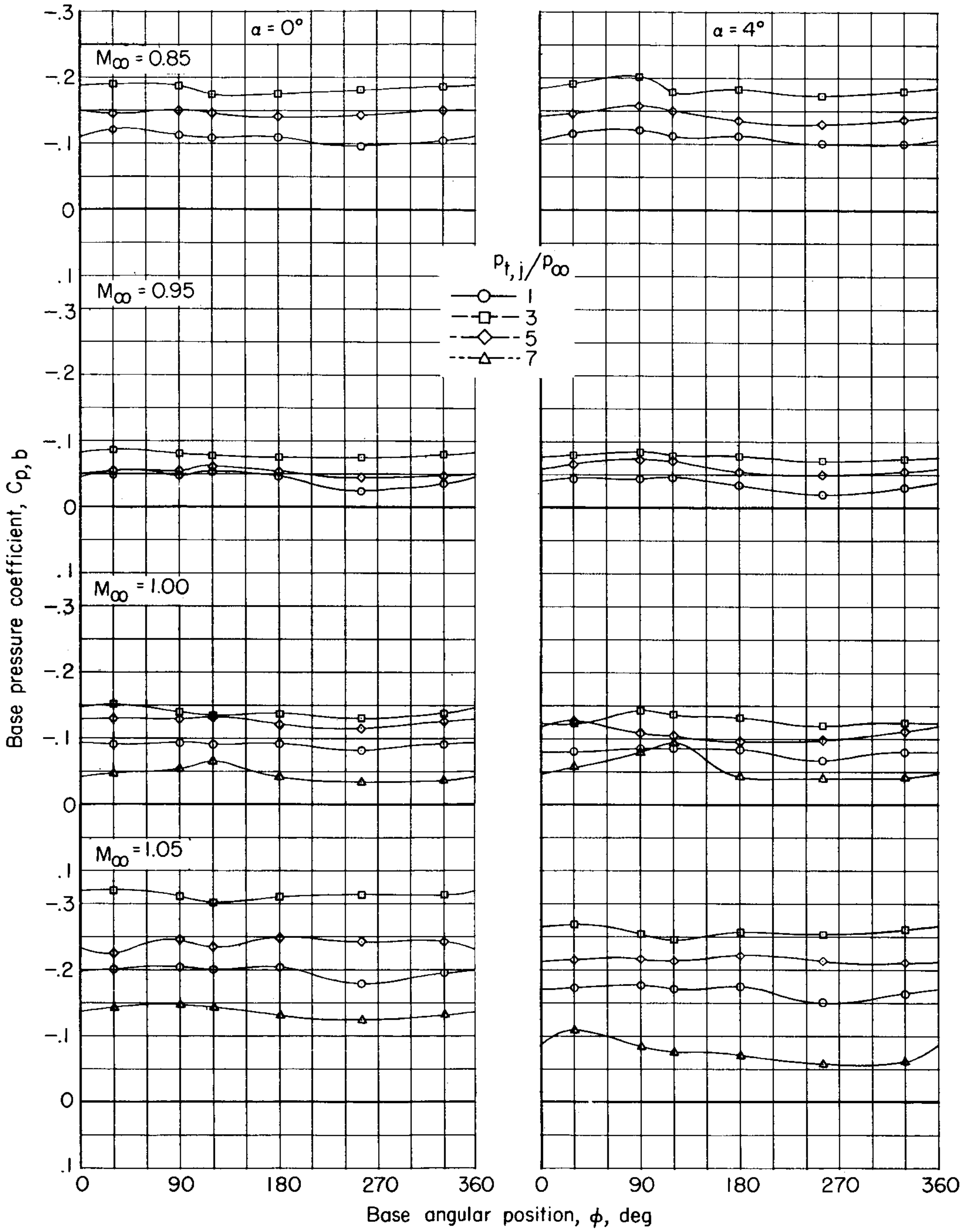

(b) Configuration II.

Figure 11.- Continued.

[redacted]

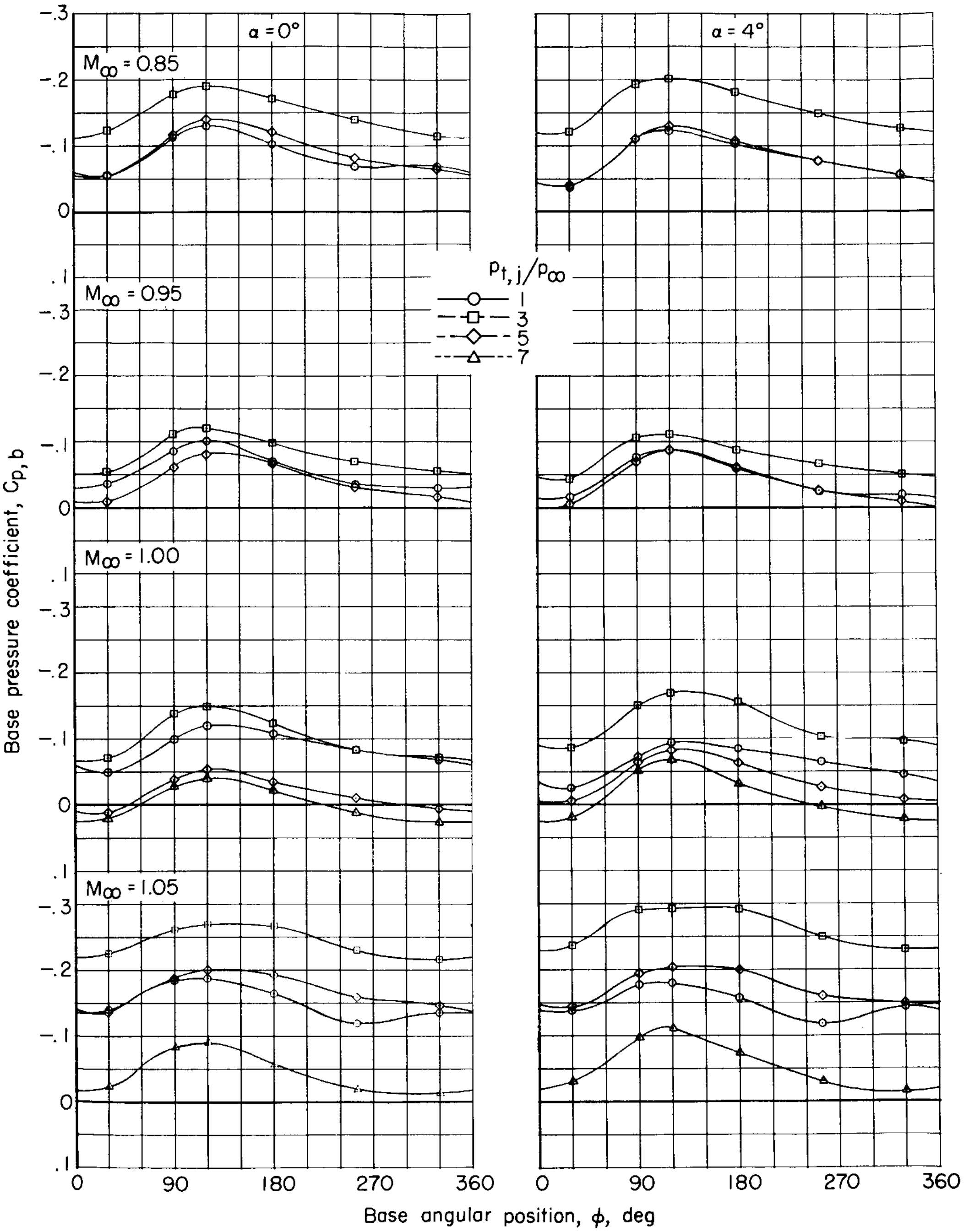

(c) Configuration III.

Figure 11.- Concluded.

[redacted]

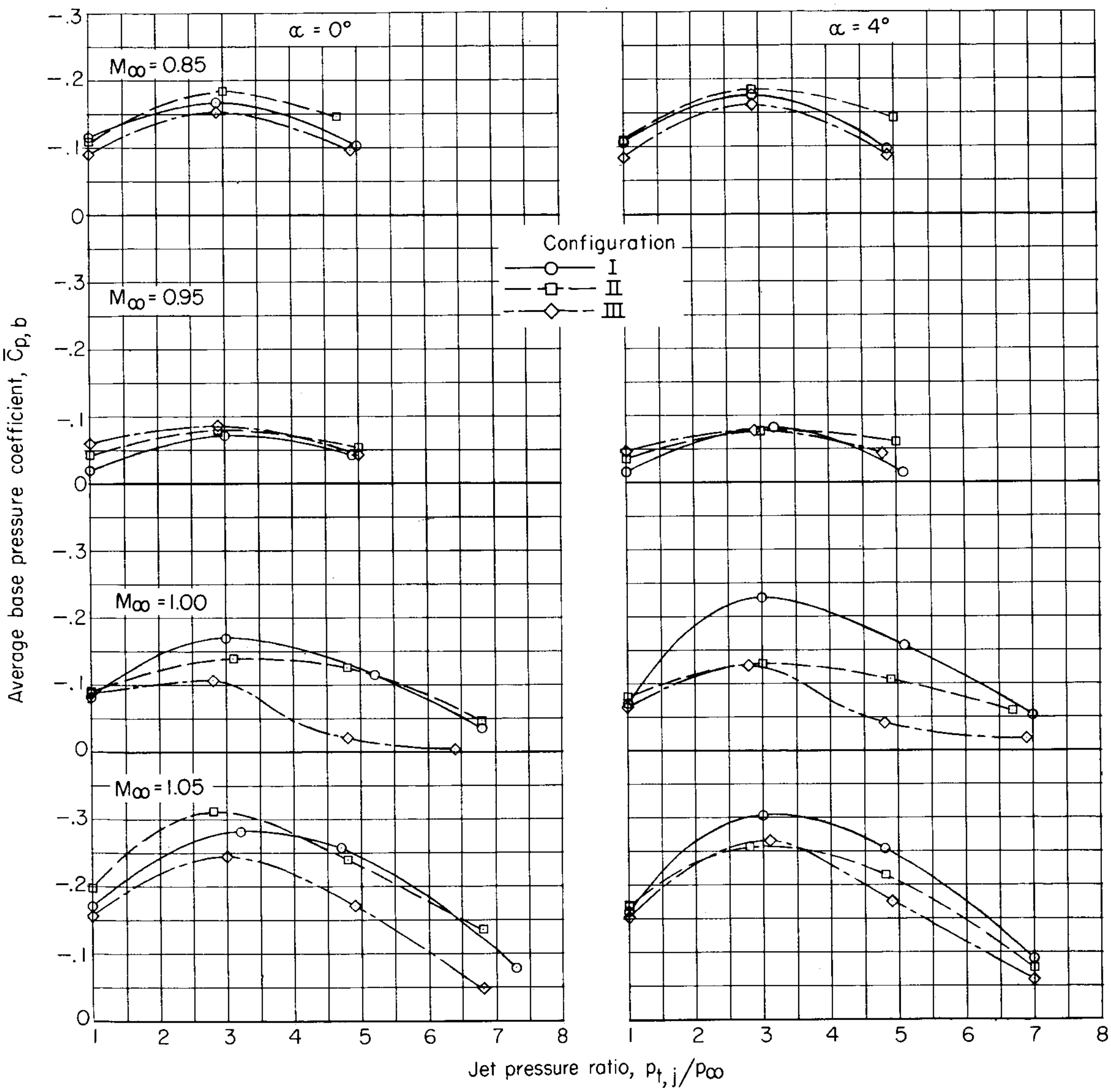

Figure 12.- Jet effects on average base pressure coefficient of various model configurations.

[redacted]

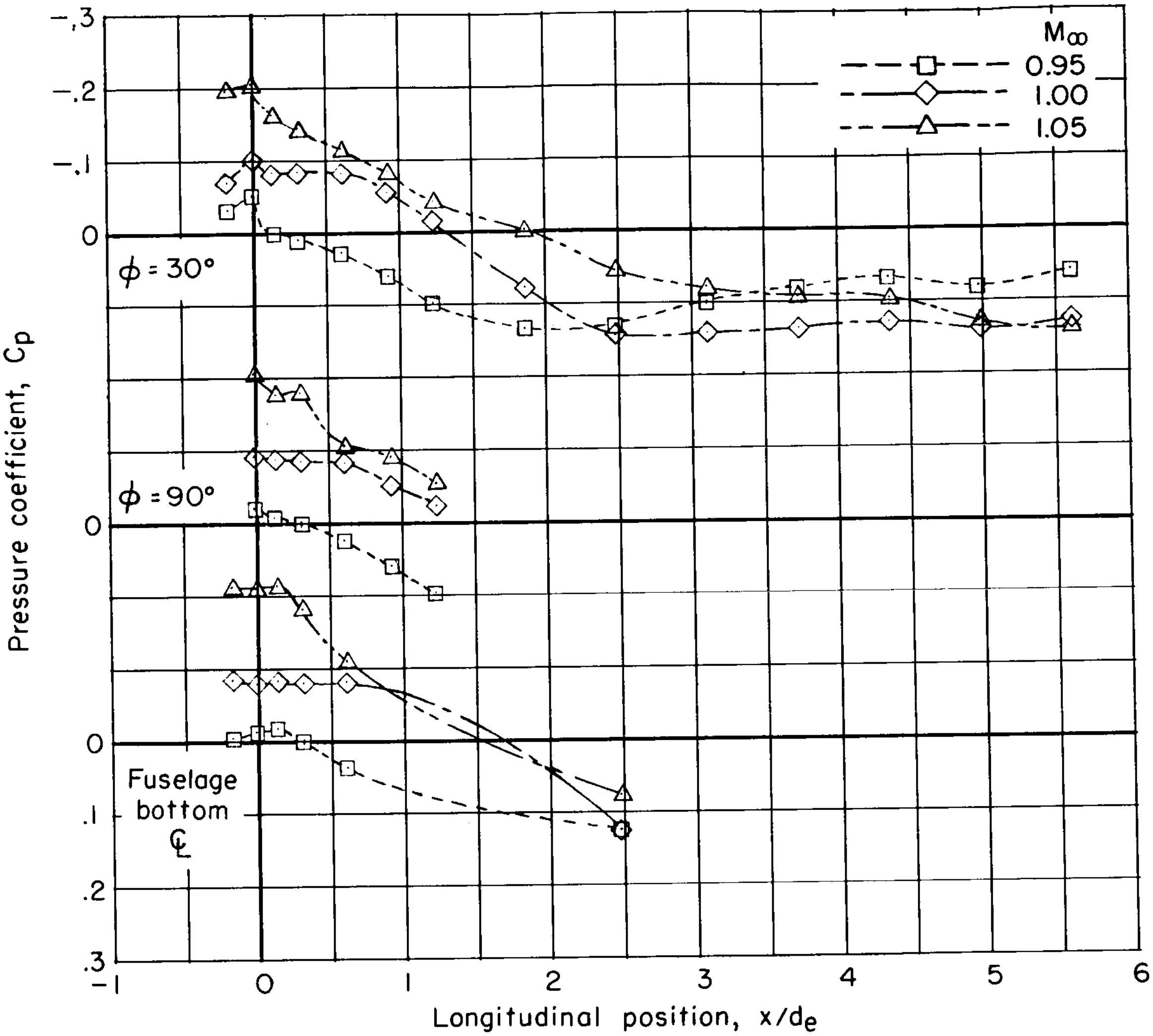

(a) $\alpha = 0^\circ$; $\frac{p_{t,j}}{p_\infty} = 1$.

Figure 13.- Variation of afterbody pressure distributions with Mach number for various jet pressure ratios and angles of attack. Configuration I.

[redacted]

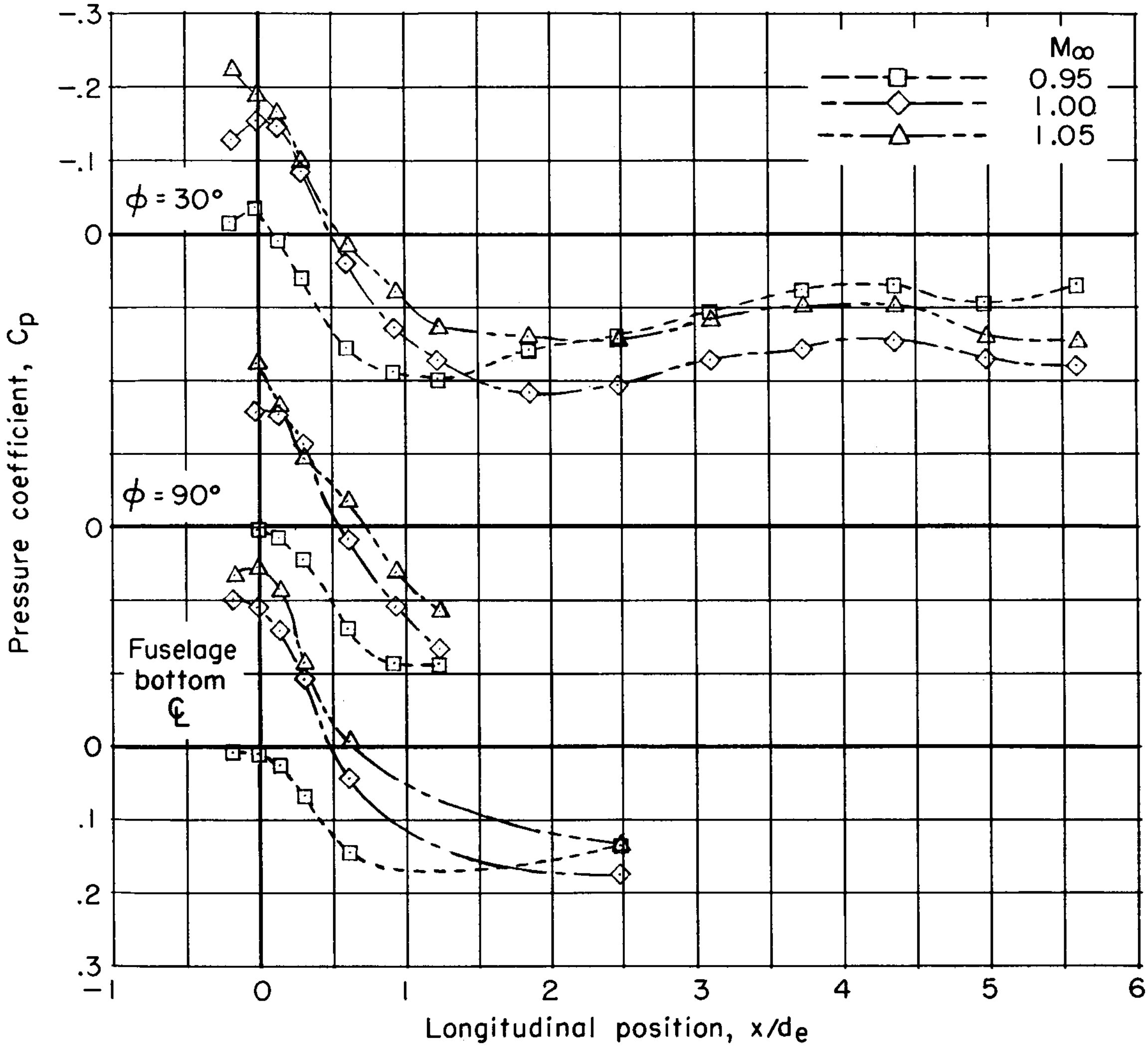

(b) $\alpha = 0^\circ;\ \frac{p_{t,j}}{p_\infty} = 3.$

Figure 13.- Continued.

[redacted]

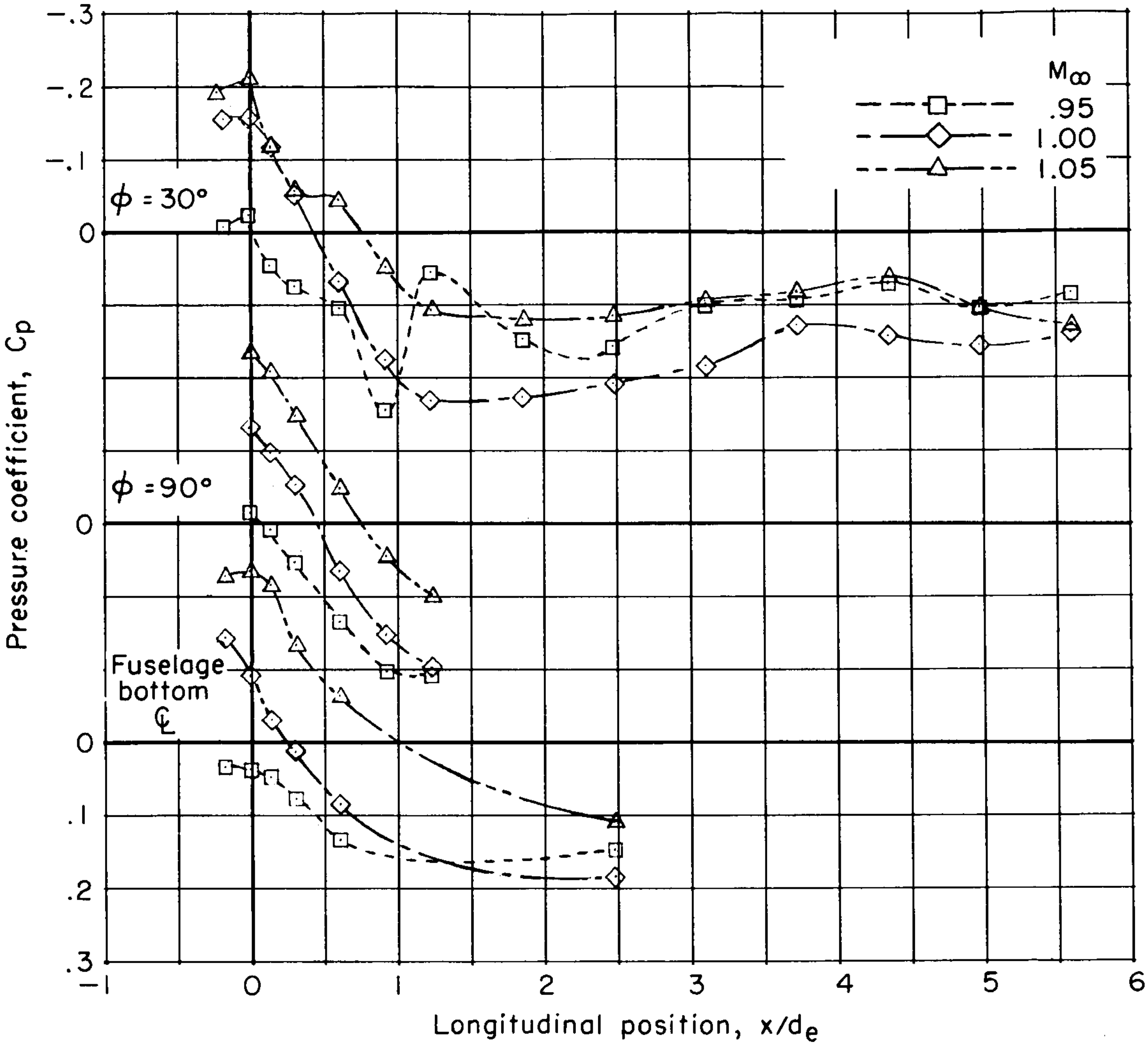

(c) $\alpha = 0^\circ; \; \frac{p_{t,j}}{p_\infty} = 5.$

Figure 13.- Continued.

[redacted]

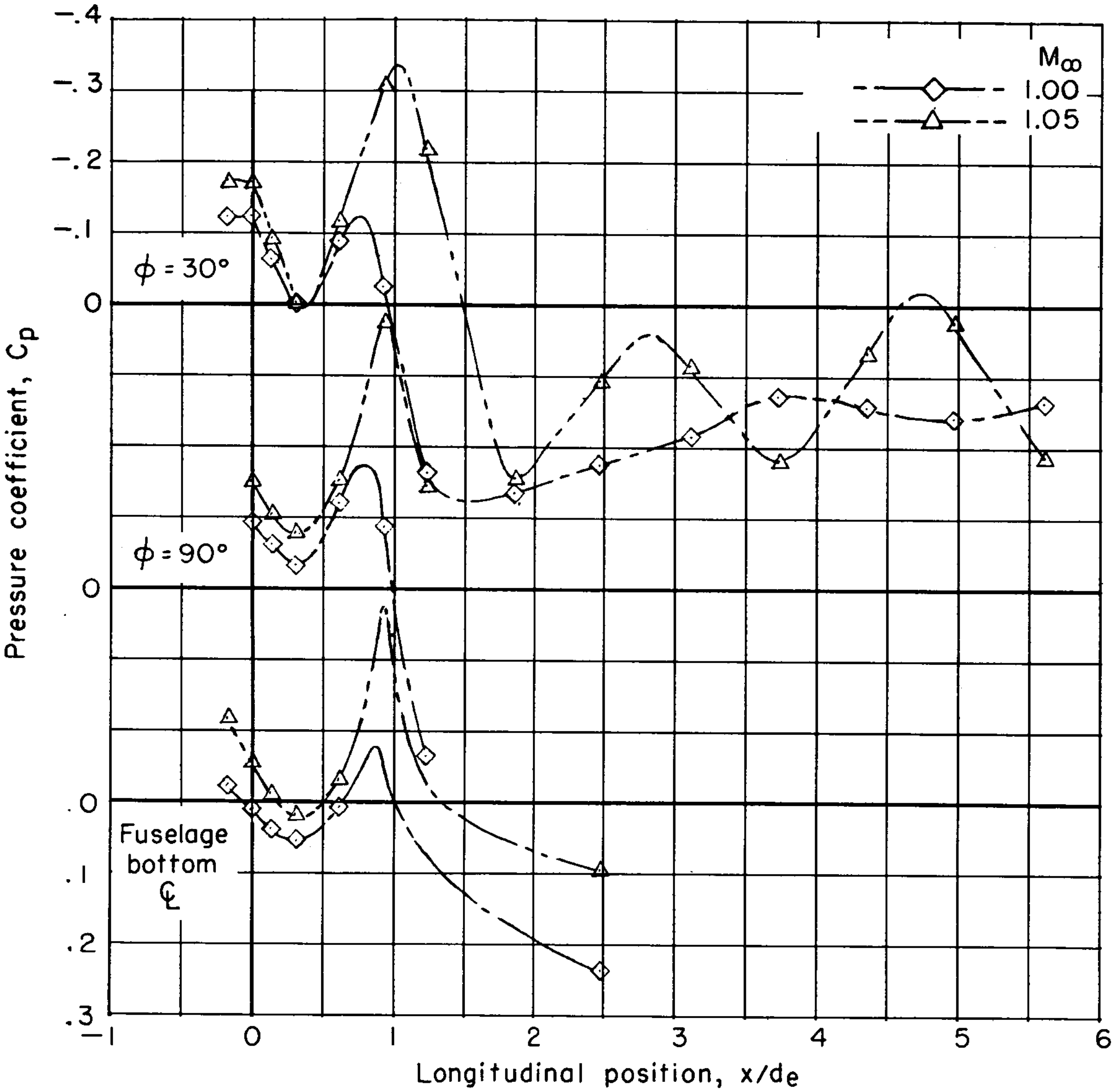

(d) $\alpha = 0^{\circ}$; $\frac{p_{t,j}}{p_\infty} = 7$.

Figure 13.- Continued.

[redacted]

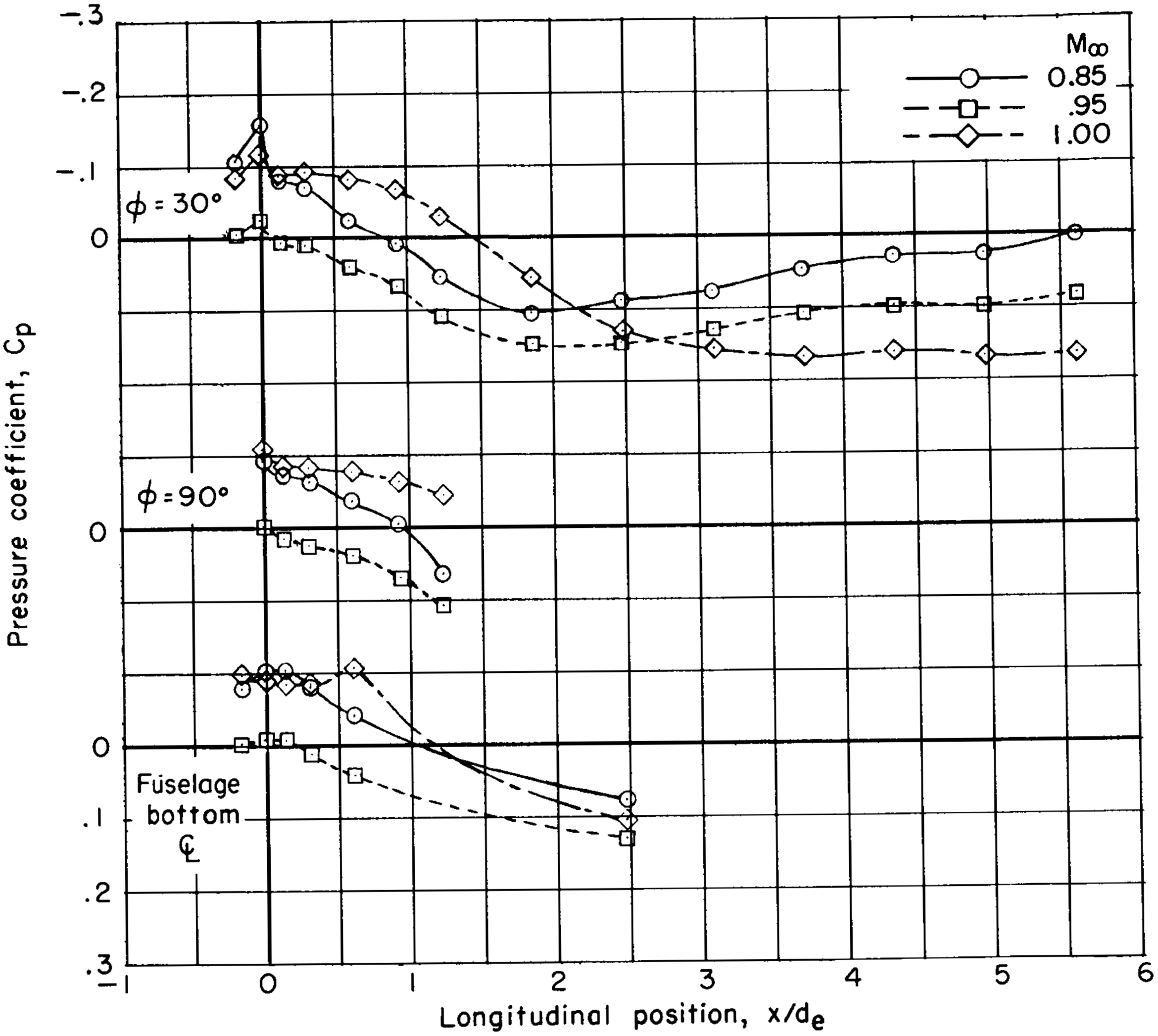

(e) $\alpha = 4^\circ;\ \dfrac{p_{t,j}}{p_\infty} = 1.$

Figure 13.- Continued.

[redacted]

DECLASSIFIED

[redacted]

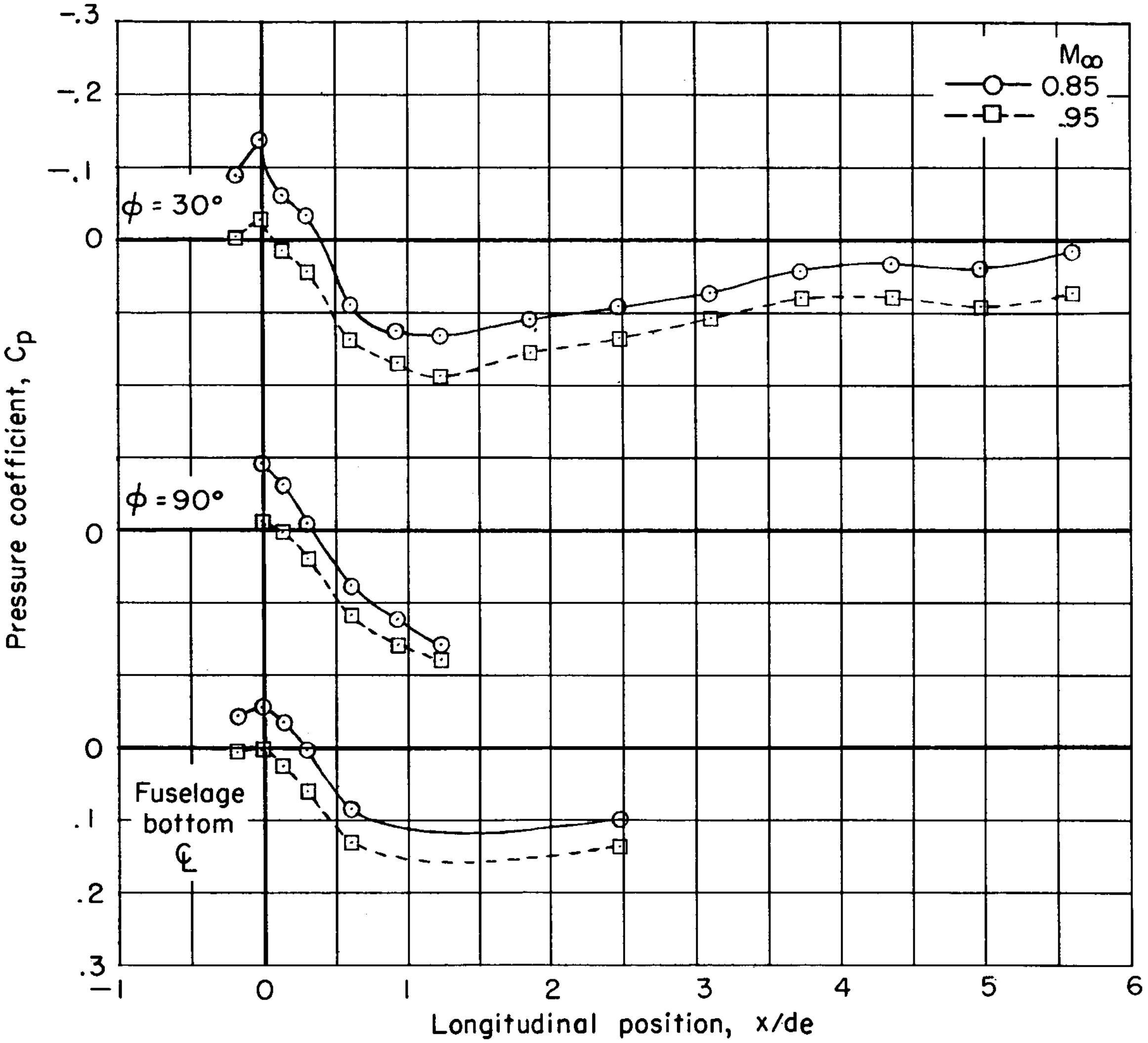

(f) $\alpha = 4^\circ$; $\frac{p_{t,j}}{p_\infty} = 3$.

Figure 13.- Continued.

[redacted]

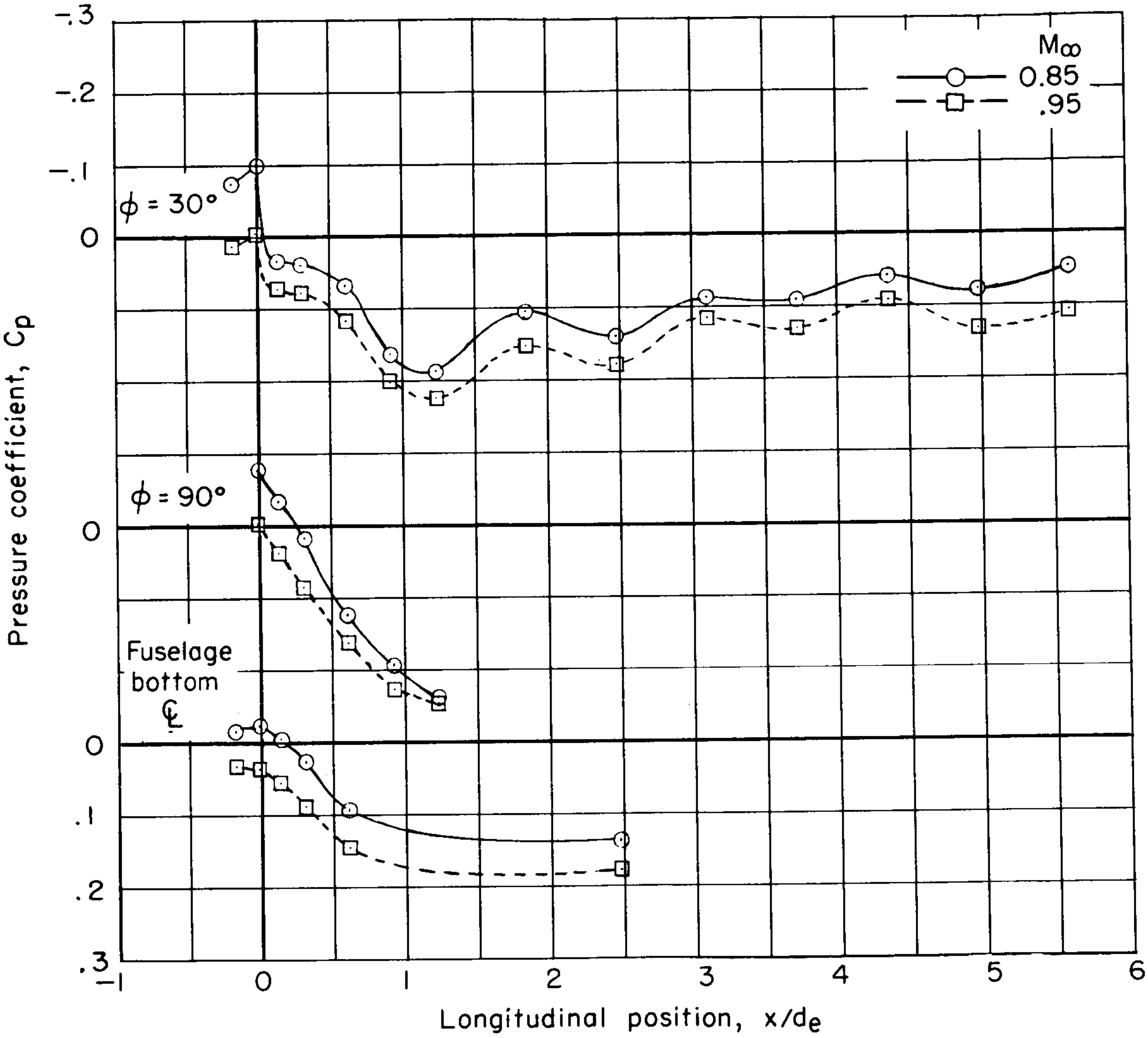

(g) $\alpha = 4^\circ;\ \frac{p_{t,j}}{p_\infty} = 5.$

Figure 13.- Continued.

[redacted]

DECLASSIFIED

[redacted]

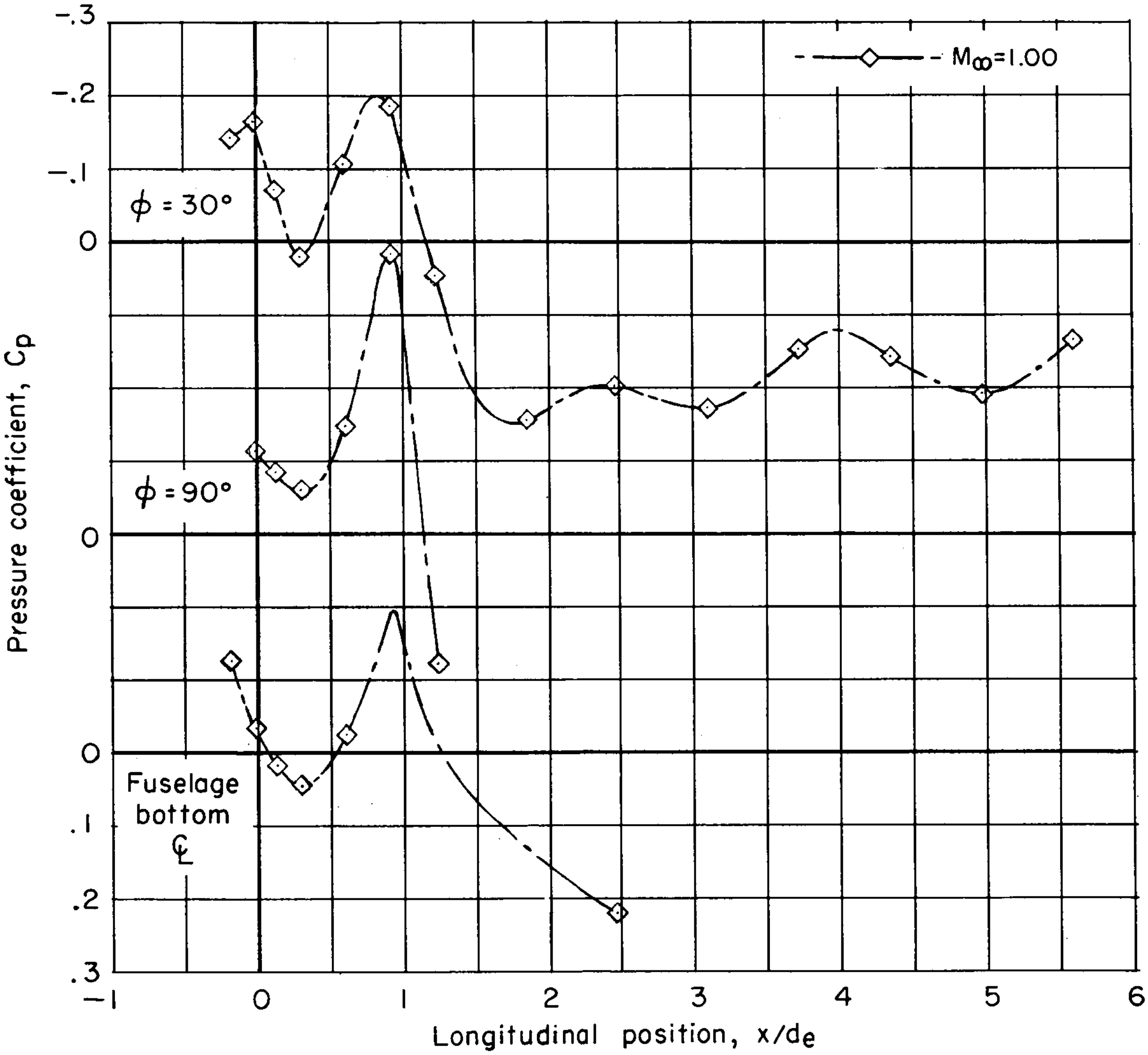

(h) $\alpha = 4^{\circ}; \ \frac{p_{t,j}}{p_{\infty}} = 7.$

Figure 13.- Concluded.

[redacted]

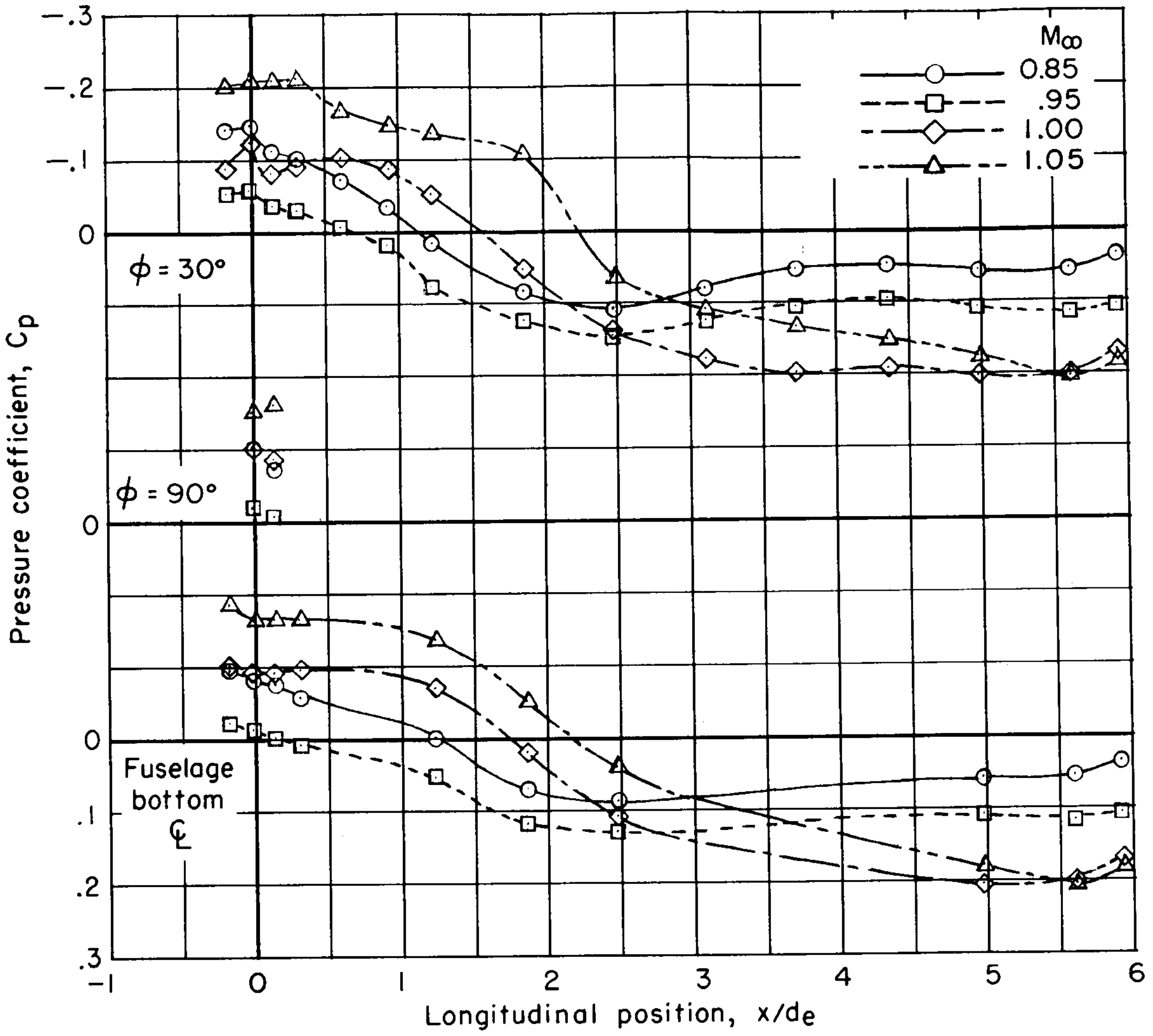

(a) $\alpha = 0^\circ$; $\frac{p_{t,j}}{p_\infty} = 1$.

Figure 14.- Variation of afterbody pressure distributions with Mach number for various jet pressure ratios and angles of attack. Configuration II.

[redacted]

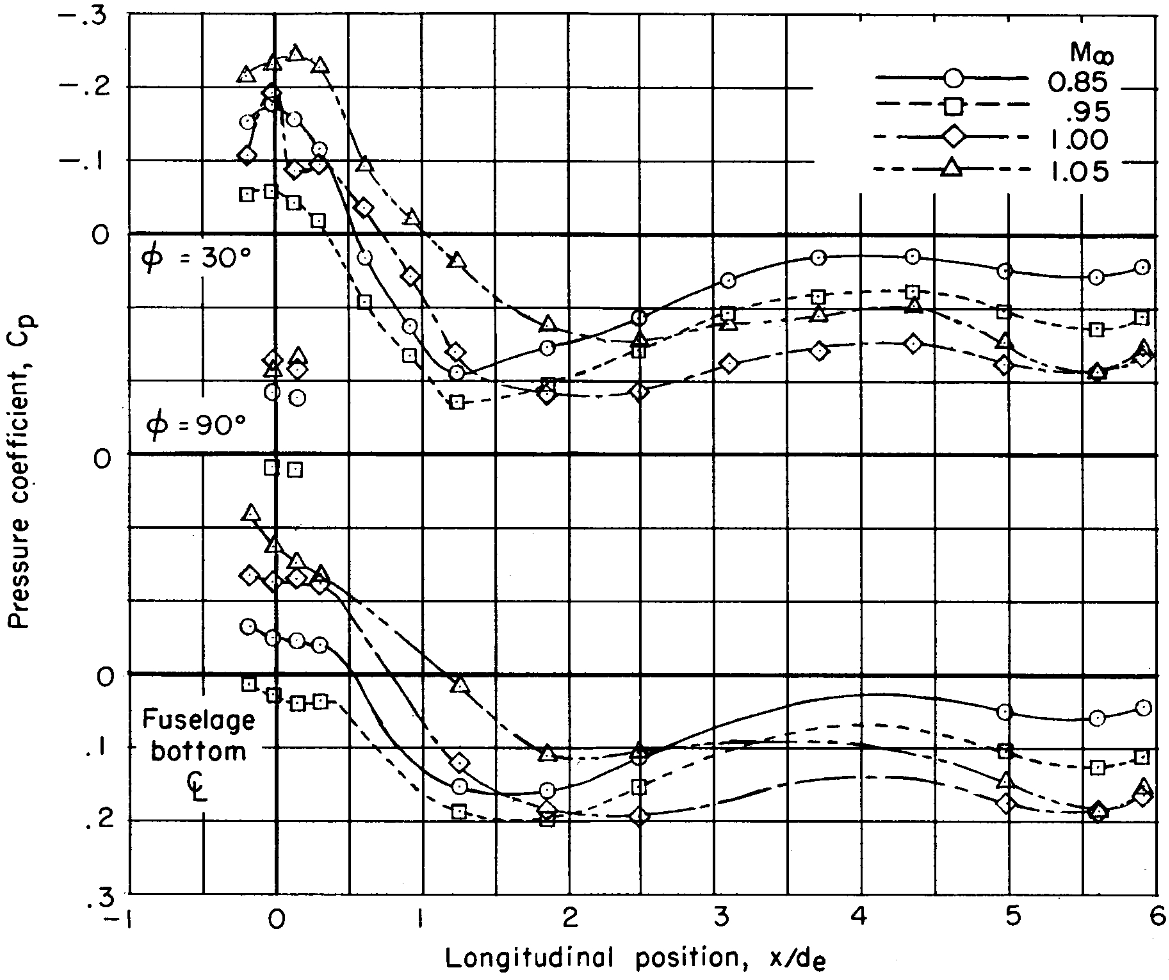

(b) $\alpha = 0^\circ$; $\dfrac{p_{t,j}}{p_\infty} = 3$.

Figure 14.- Continued.

[redacted]

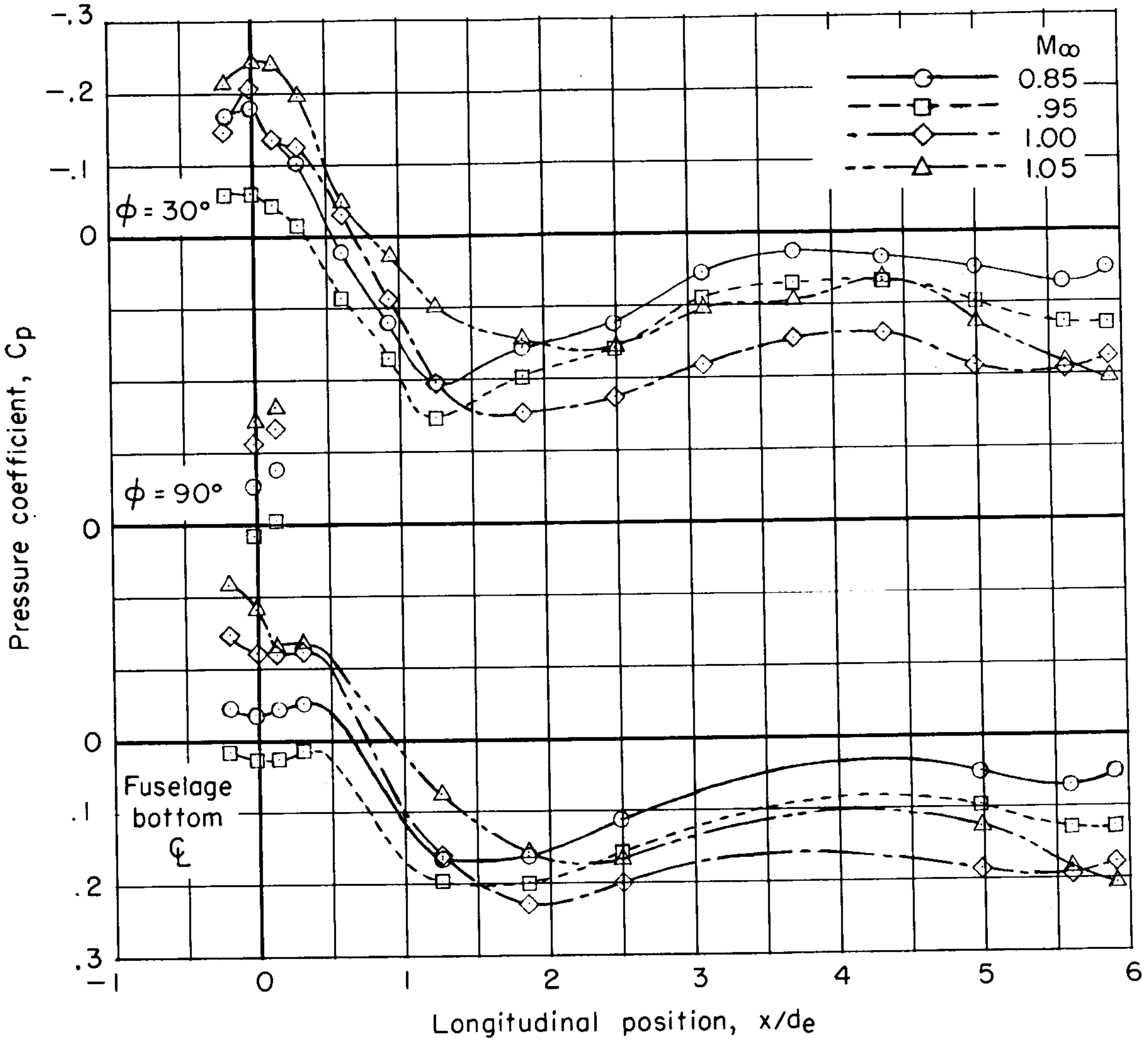

(c) $\alpha = 0^\circ$; $\frac{p_{t,j}}{p_\infty} = 5$.

Figure 14.- Continued.

[redacted]

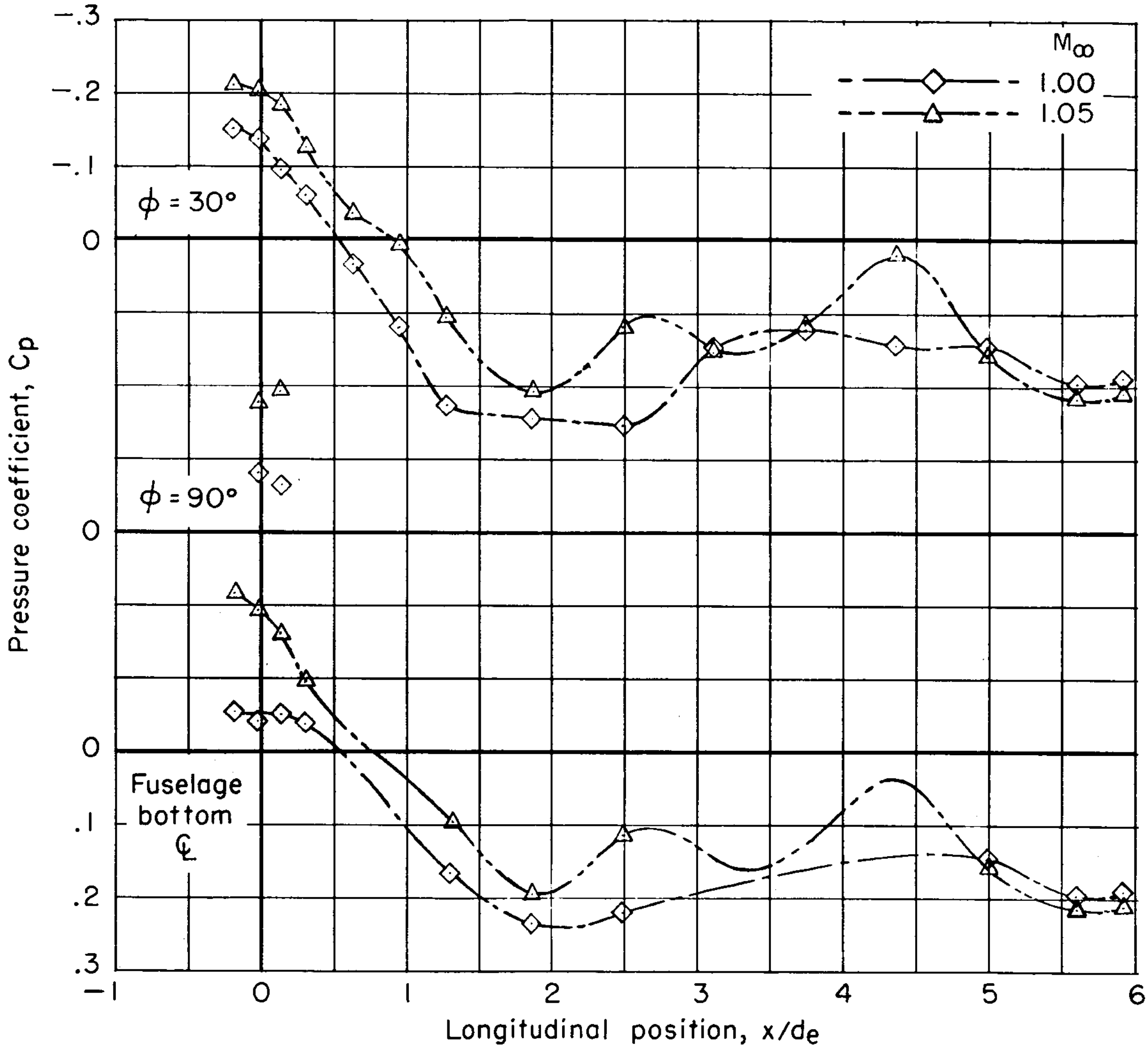

(d) $\alpha = 0^{\circ}; \frac{p_{t,j}}{p_\infty} = 7.$

Figure 14.- Continued.

[redacted]

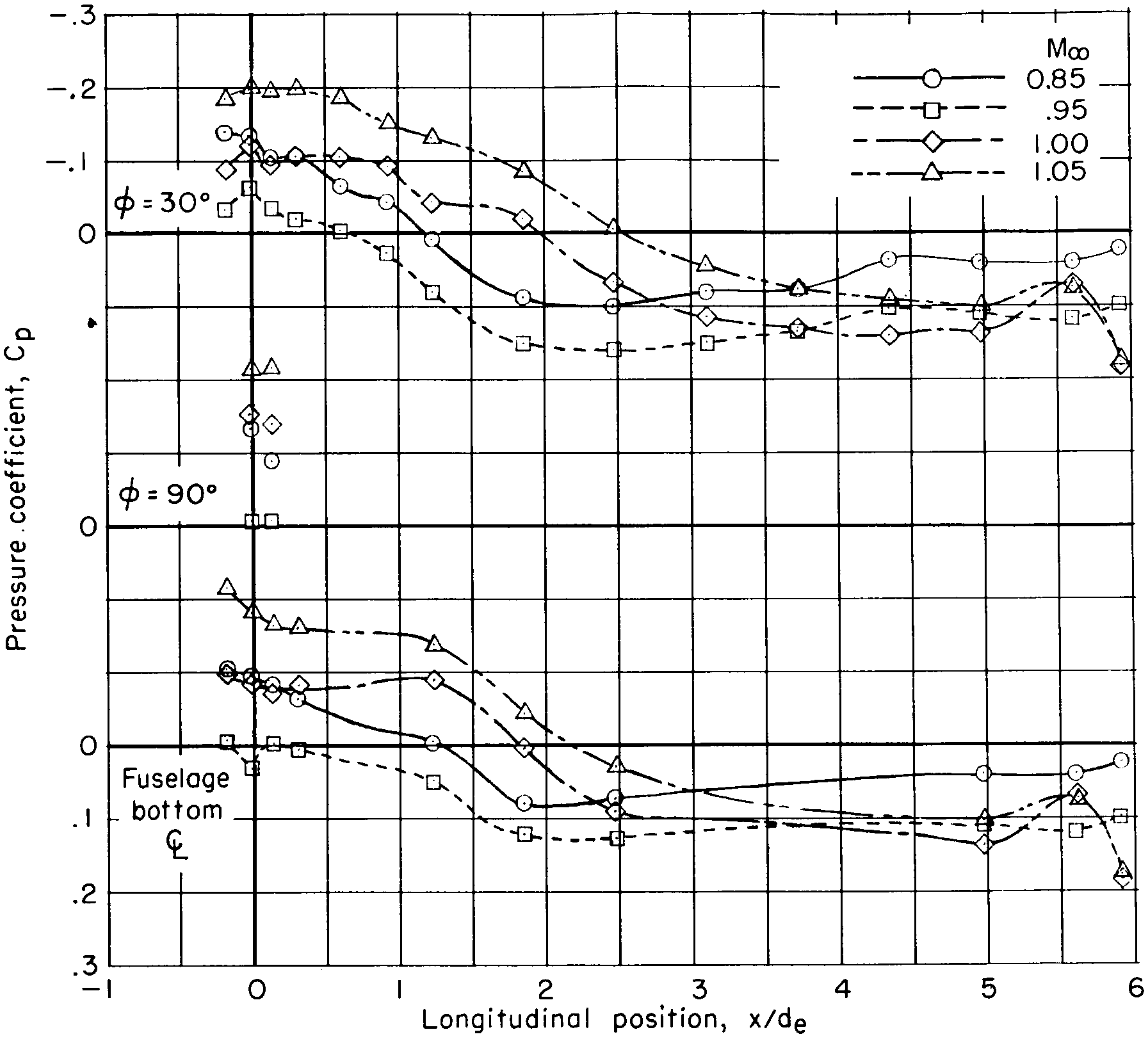

(e) $\alpha = 4^{\circ}$; $\frac{p_{t,j}}{p_\infty} = 1$.

Figure 14.- Continued.

[redacted]

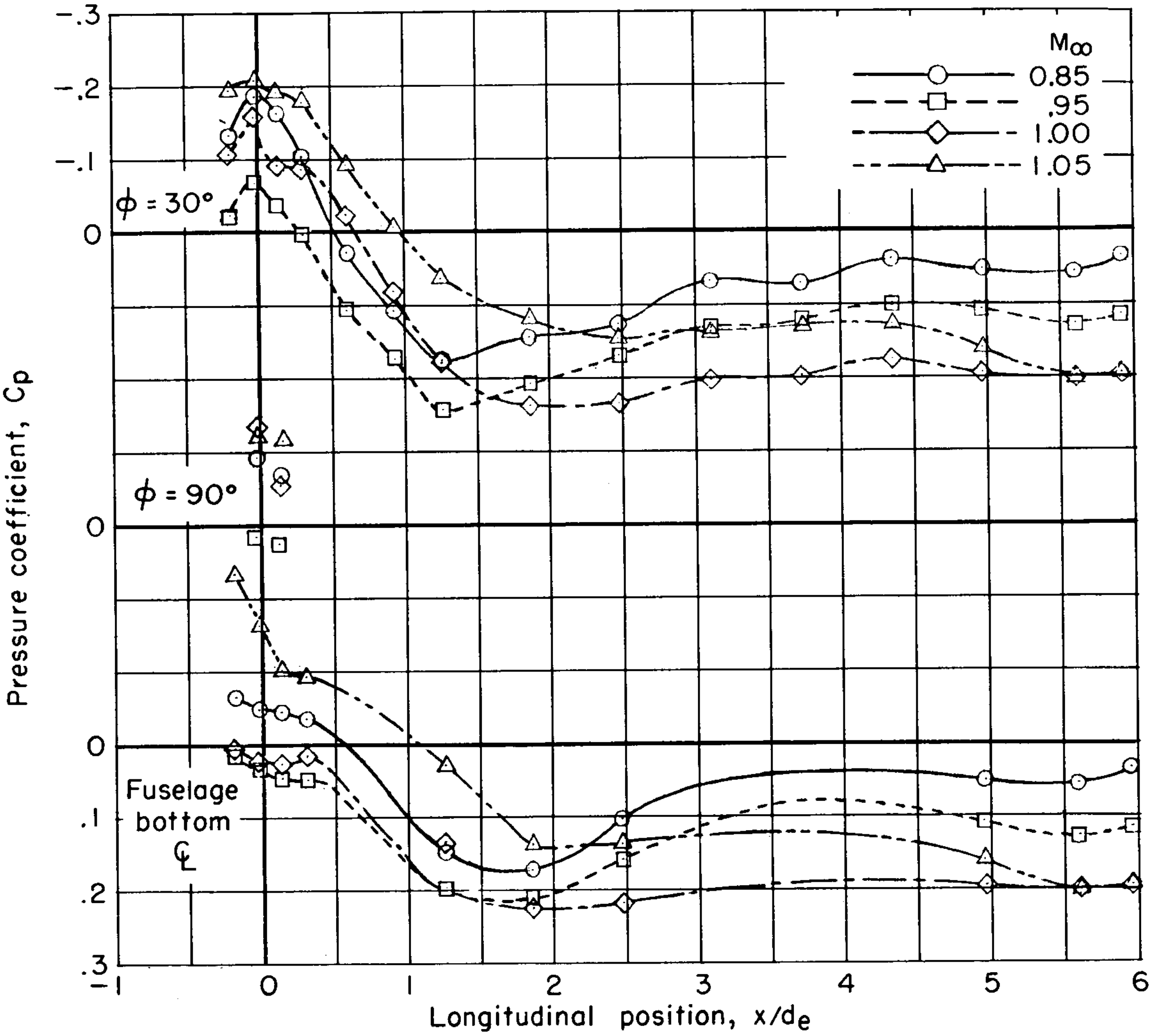

(f) $\alpha = 4^\circ$; $\frac{p_{t,j}}{p_\infty} = 3$.

Figure 14.- Continued.

[redacted]

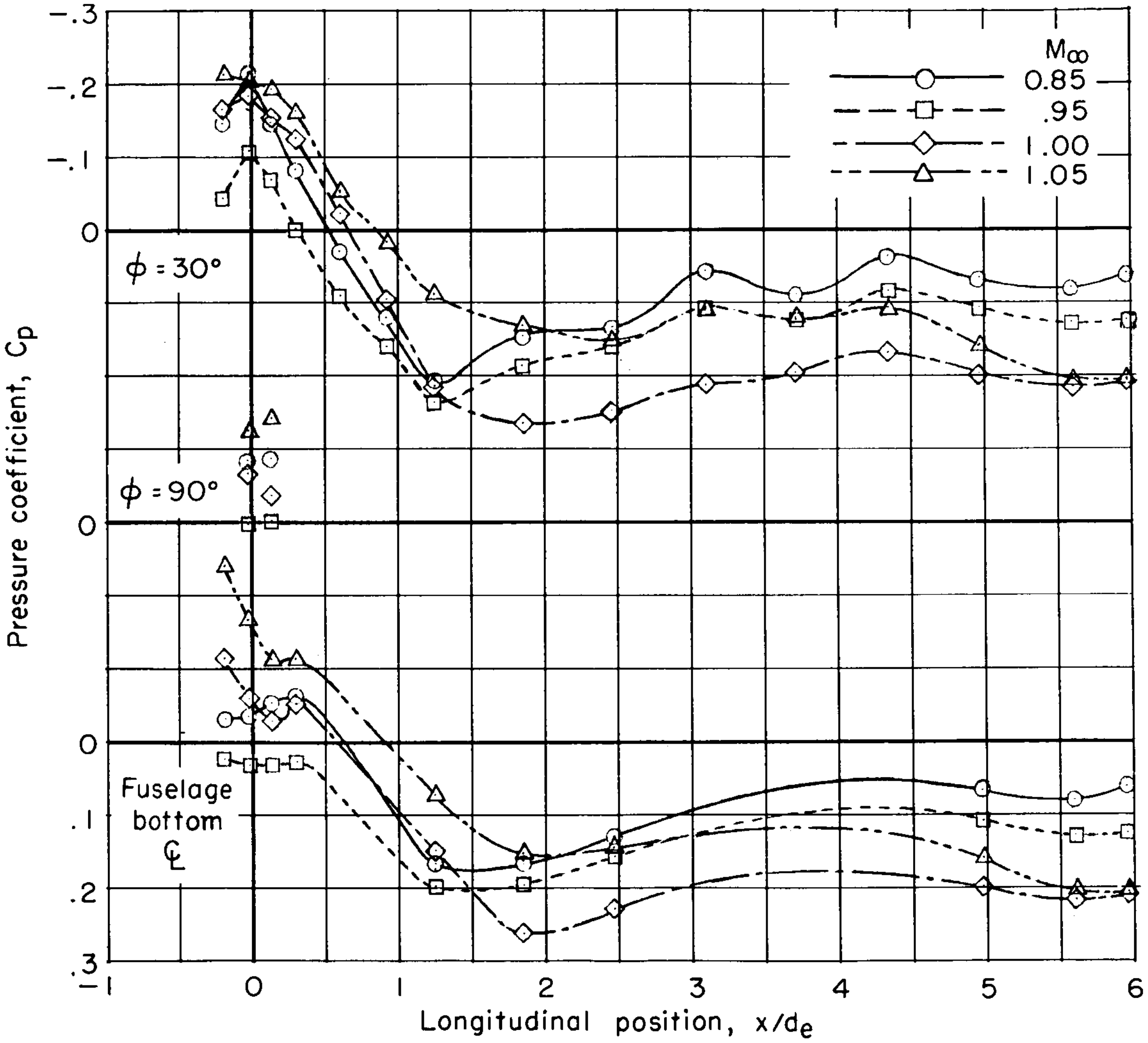

(g) $\alpha = 4^{\circ}; \frac{p_{t,j}}{p_{\infty}} = 5.$

Figure 14.- Continued.

[redacted]

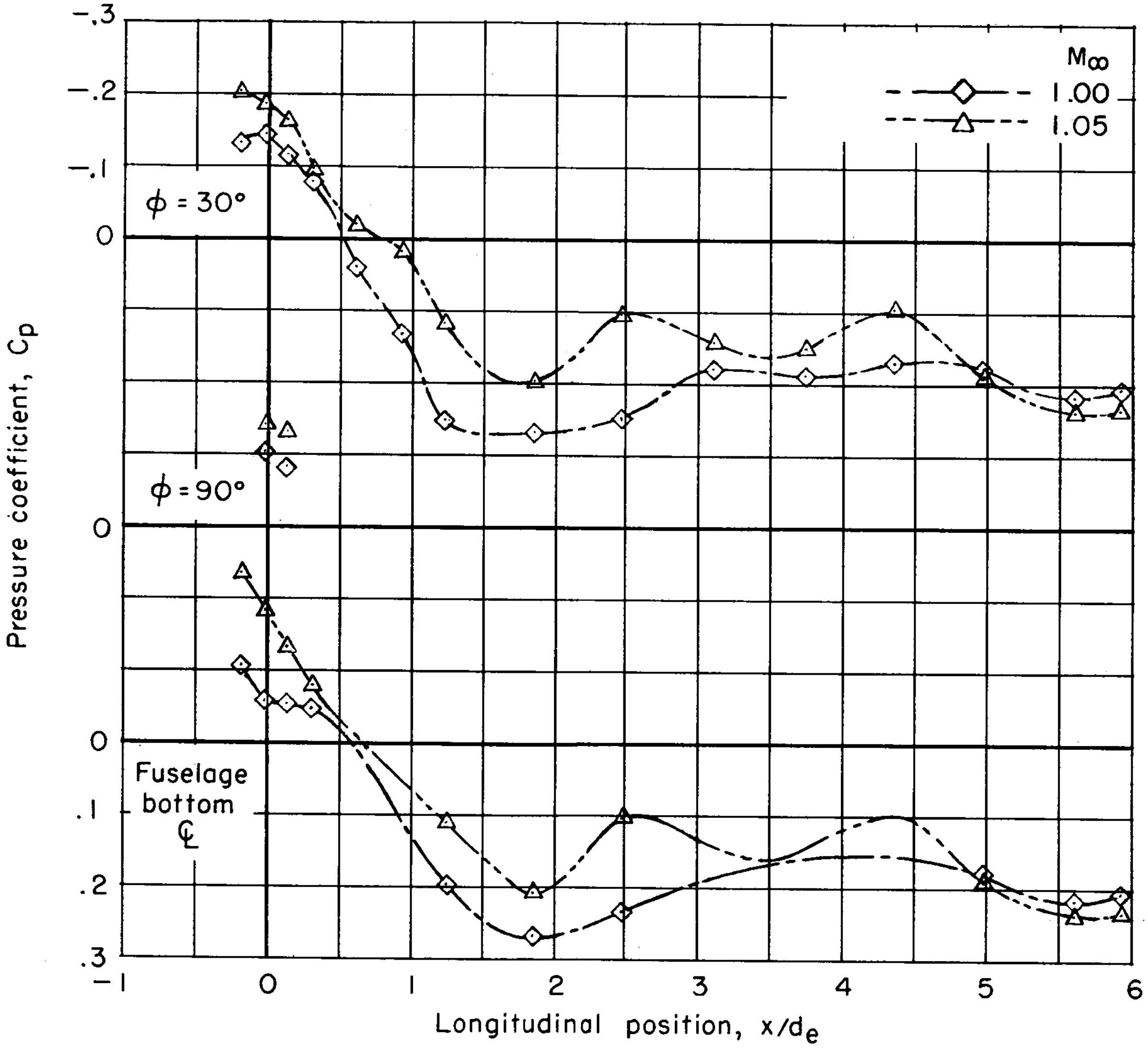

(h) $\alpha = 4^\circ$; $\dfrac{p_{t,j}}{p_\infty} = 7$.

Figure 14.- Concluded.

[redacted]

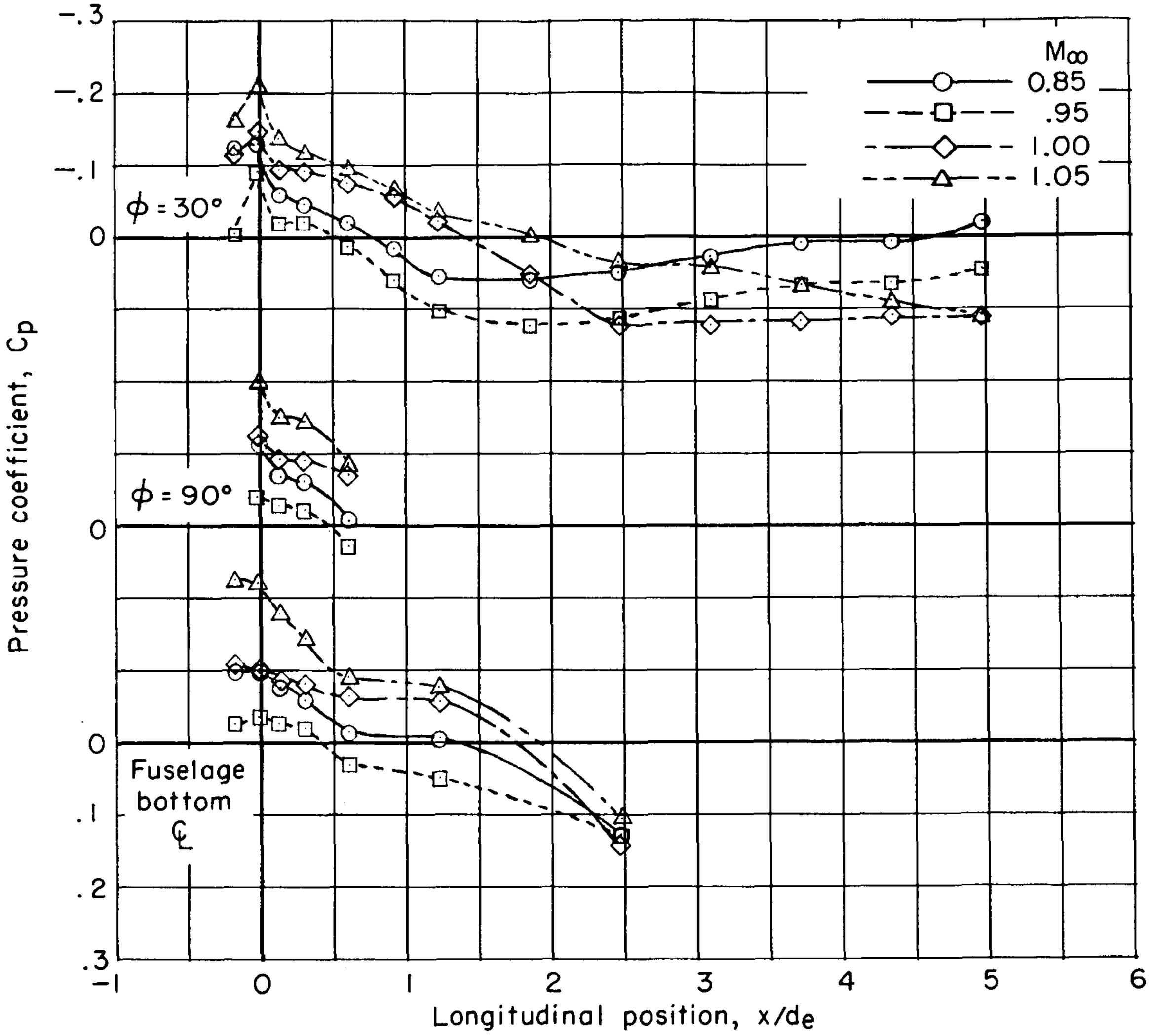

(a) $\alpha = 0^\circ$; $\frac{p_{t,j}}{p_\infty} = 1$.

Figure 15.- Variation of afterbody pressure distributions with Mach number for various jet pressure ratios and angles of attack. Configuration III.

[redacted]

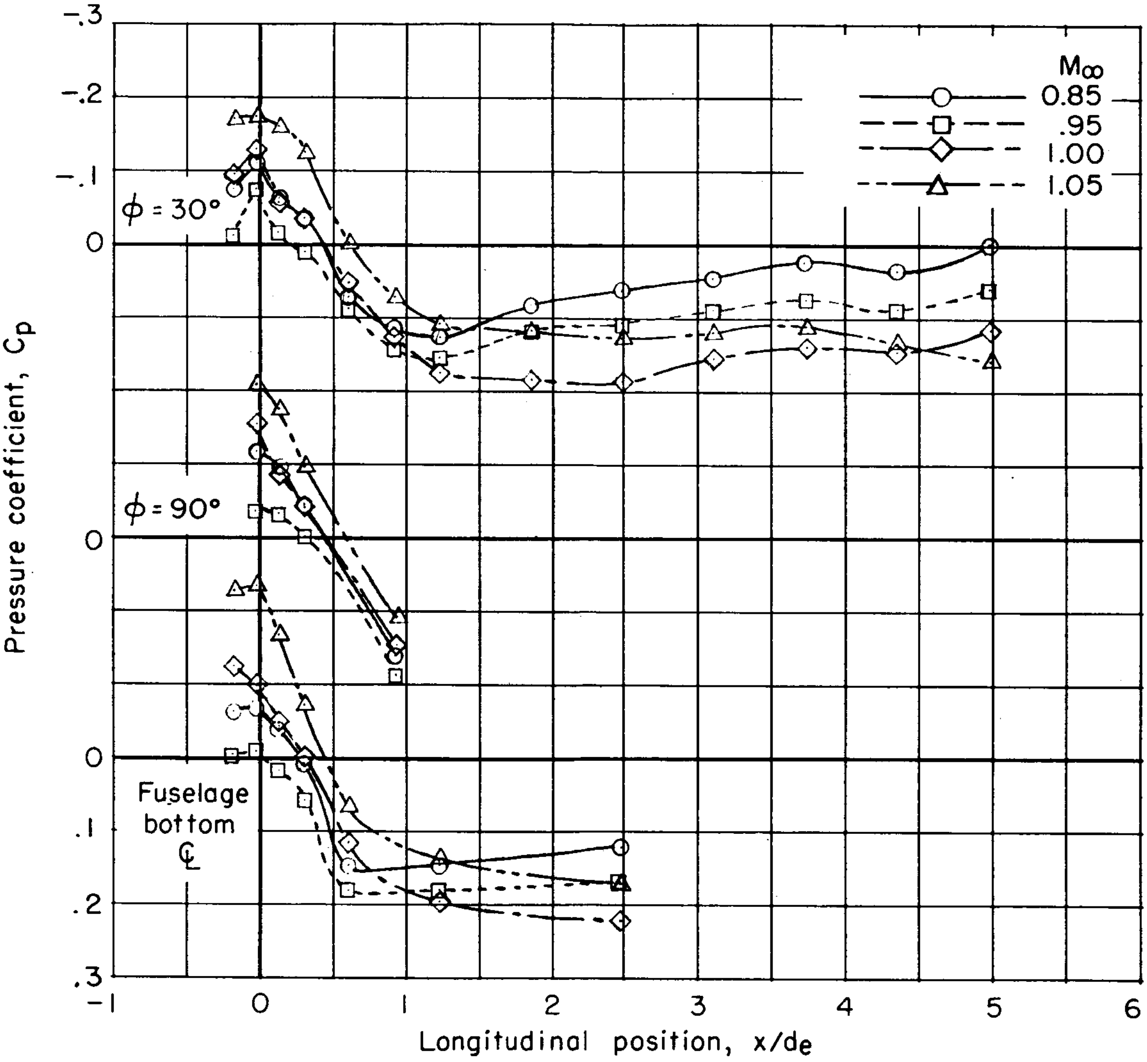

(b) $\alpha = 0^\circ$; $\frac{p_{t,j}}{p_\infty} = 3$.

Figure 15.- Continued.

[redacted]

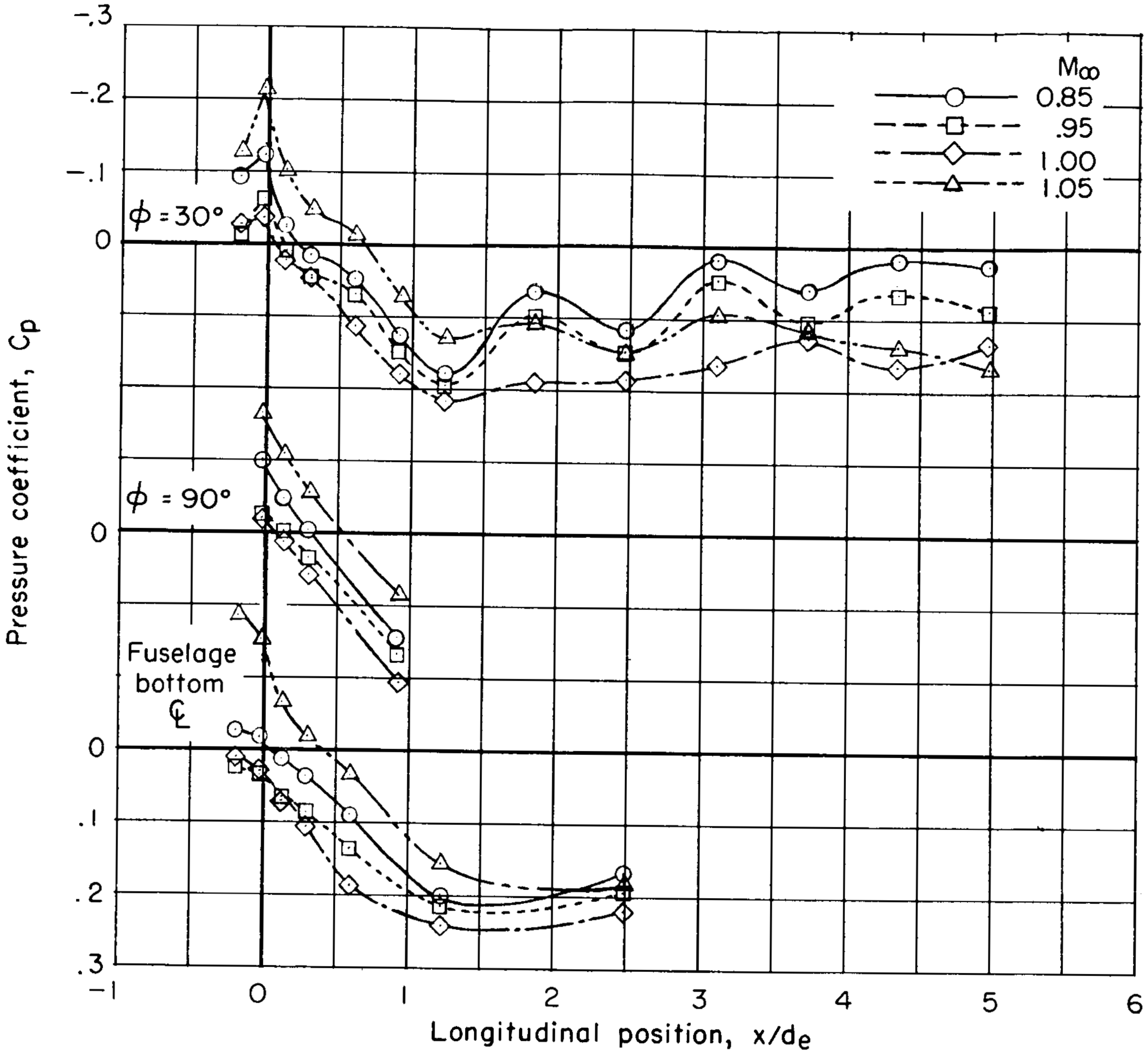

(c) $\alpha = 0^\circ$; $\frac{p_{t,j}}{p_\infty} = 5$.

Figure 15.- Continued.

[redacted]

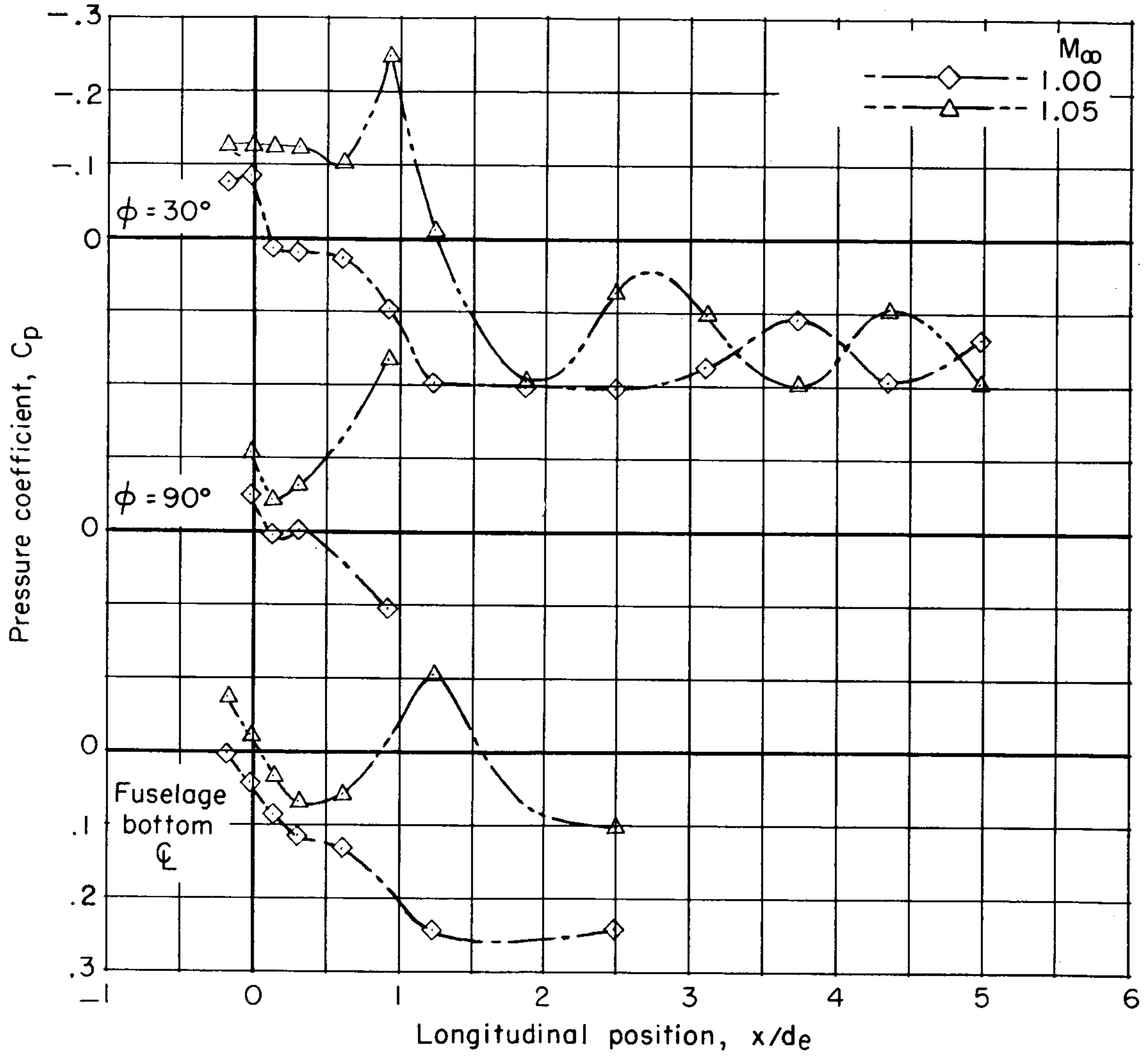

(d) $\alpha = 0^\circ$; $\frac{p_{t,j}}{p_\infty} = 7$.

Figure 15.- Continued.

[redacted]

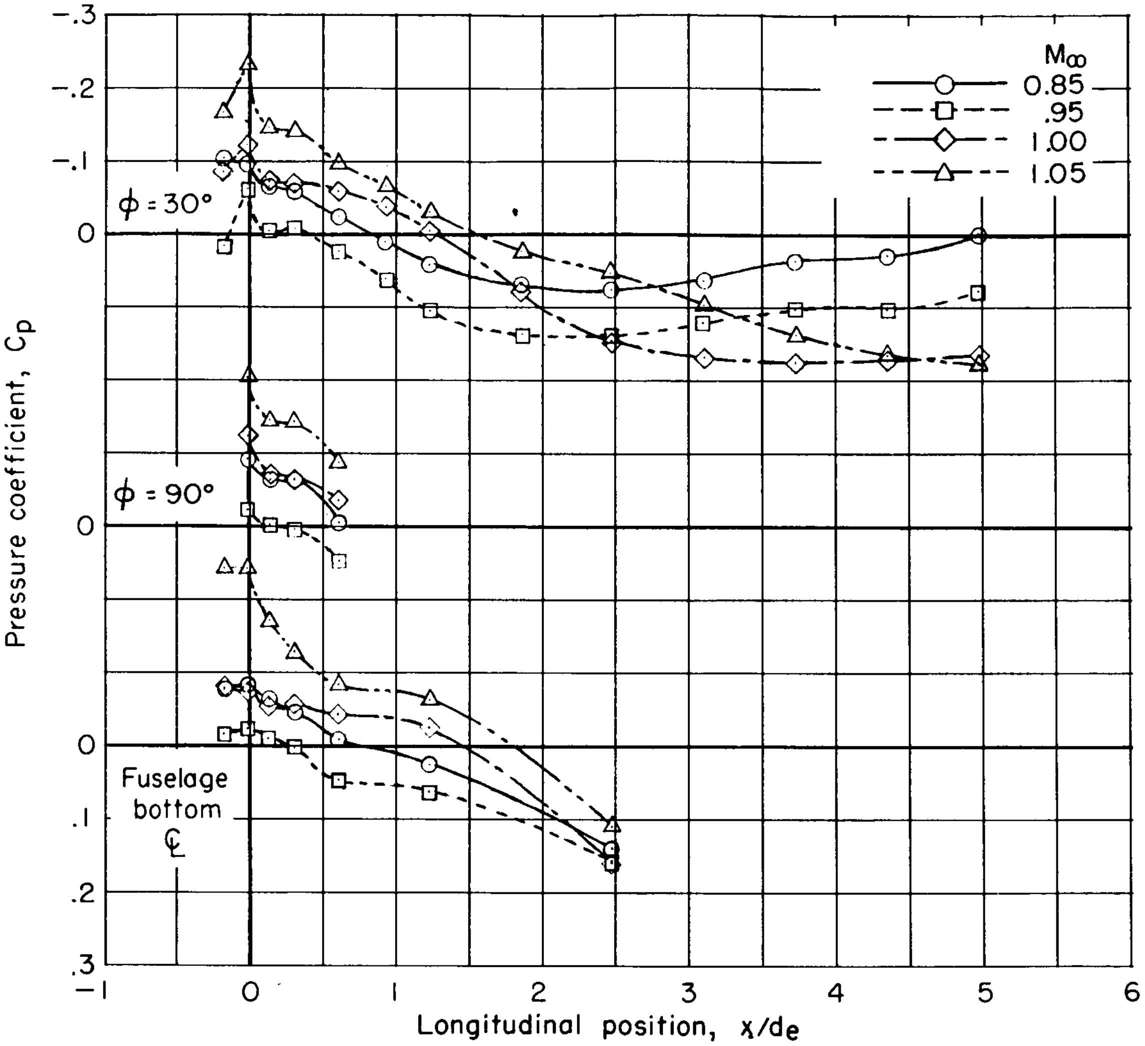

(e) $\alpha = 4^{\circ}; \frac{p_{t,j}}{p_\infty} = 1.$

Figure 15.- Continued.

[redacted]

DECLASSIFIED

[redacted]

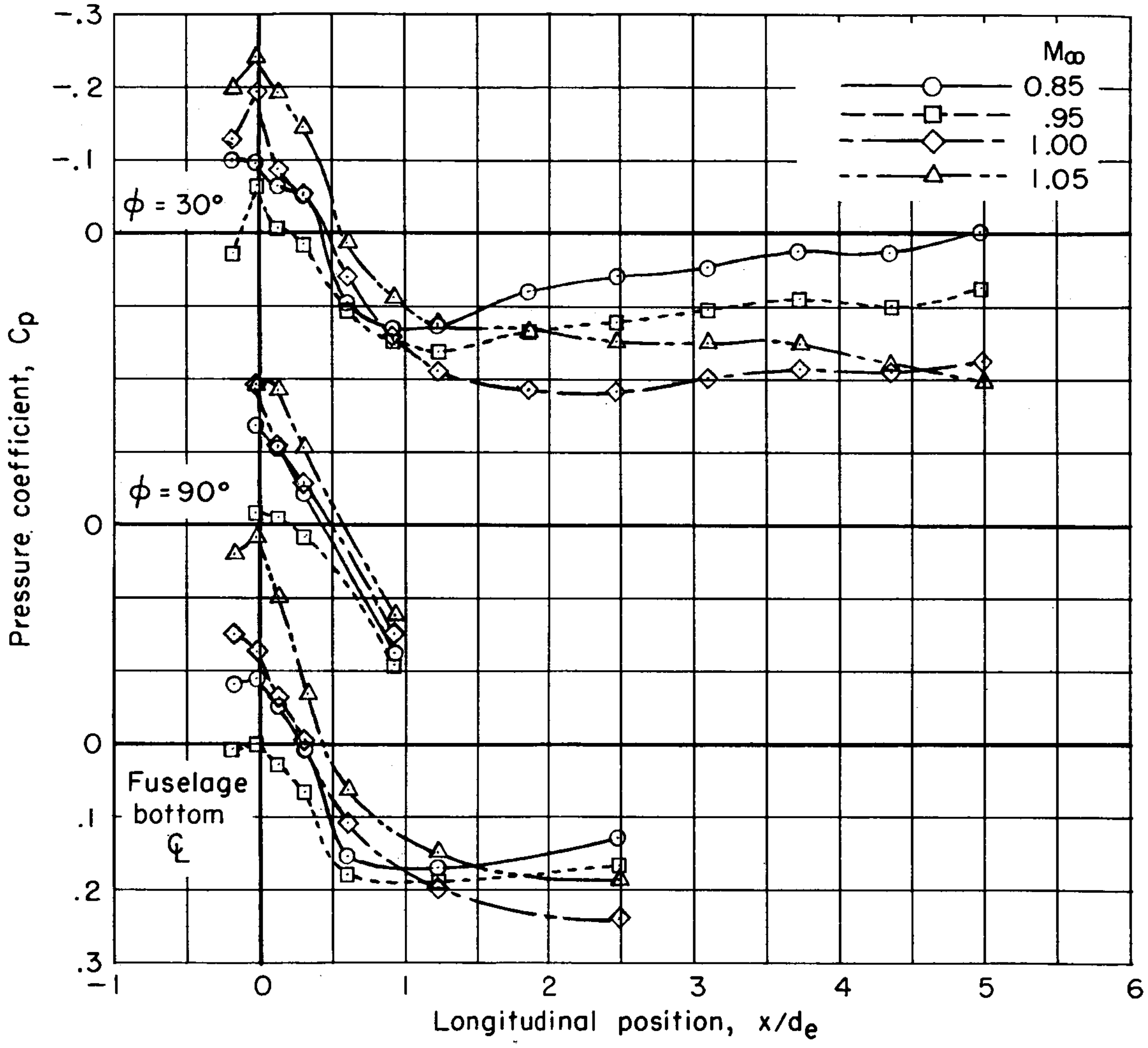

(f) $\alpha = 4^{\circ}$; $\frac{p_{t,j}}{p_{\infty}} = 3$.

Figure 15.- Continued.

[redacted]

UNCLASSIFIED

[redacted]

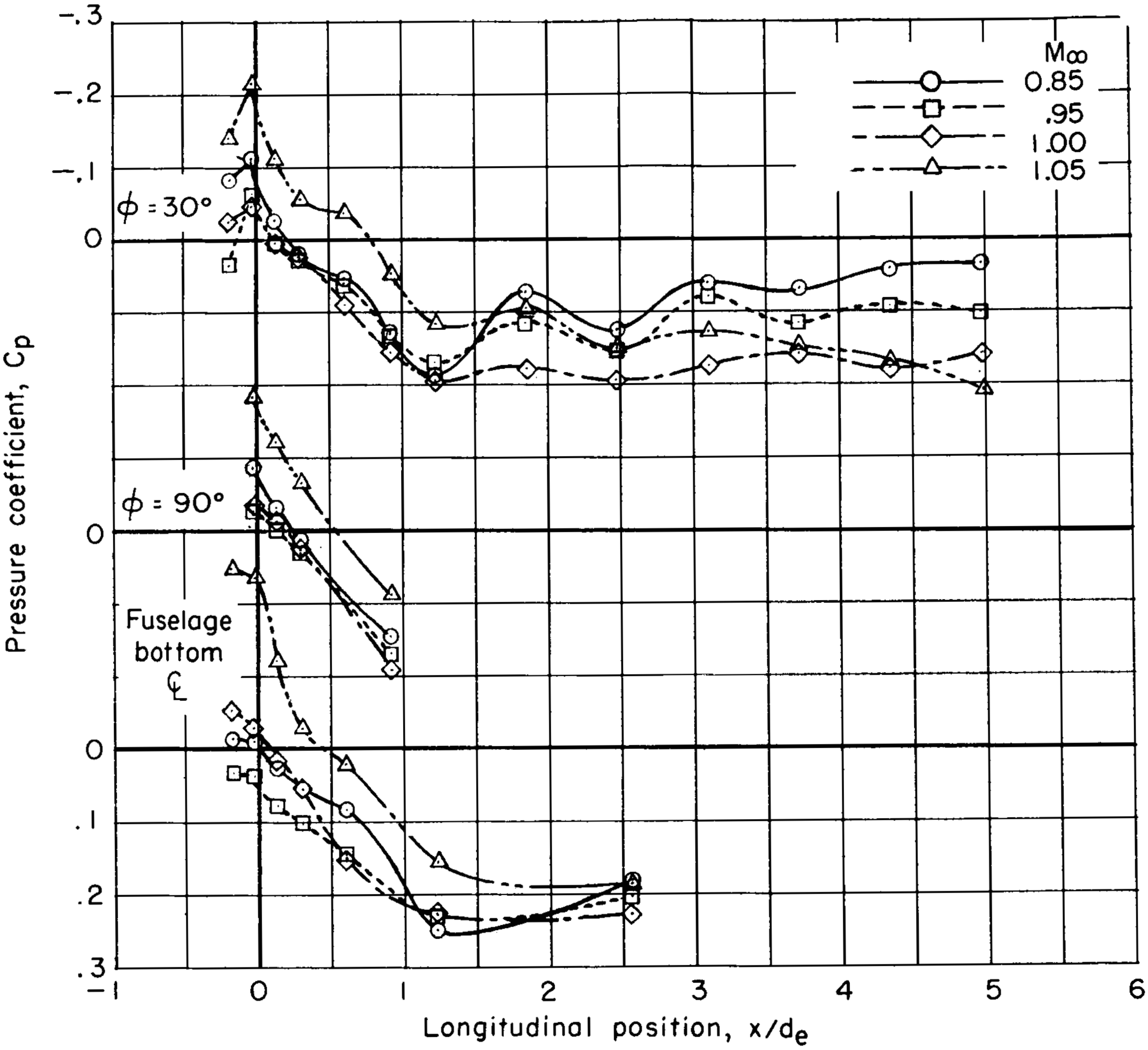

(g) $\alpha = 4^\circ$; $\dfrac{p_{t,j}}{p_\infty} = 5$.

Figure 15.- Continued.

[redacted]

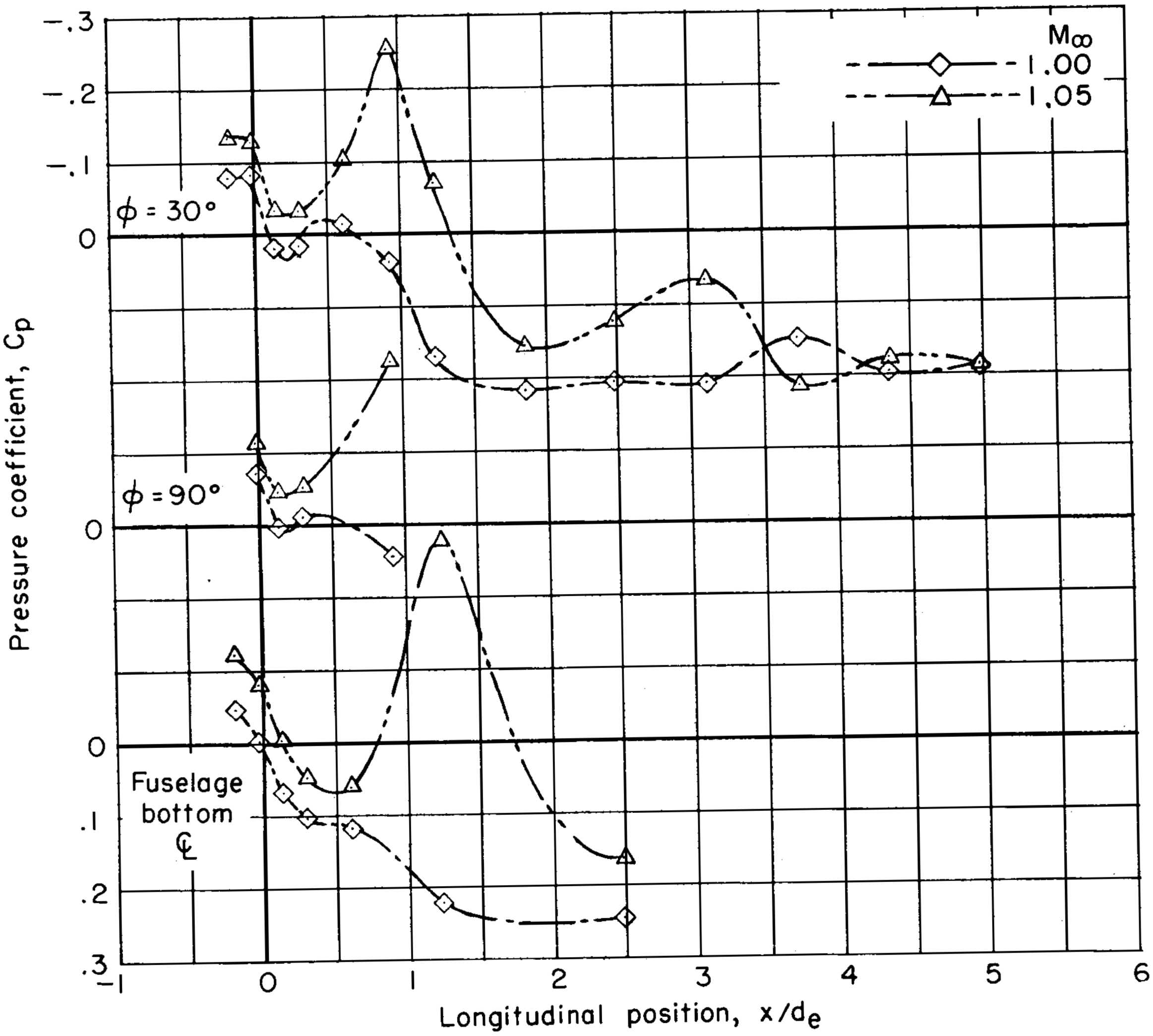

(h) $\alpha = 4^\circ$; $\frac{p_{t,j}}{p_\infty} = 7$.

Figure 15.- Concluded.

[redacted]

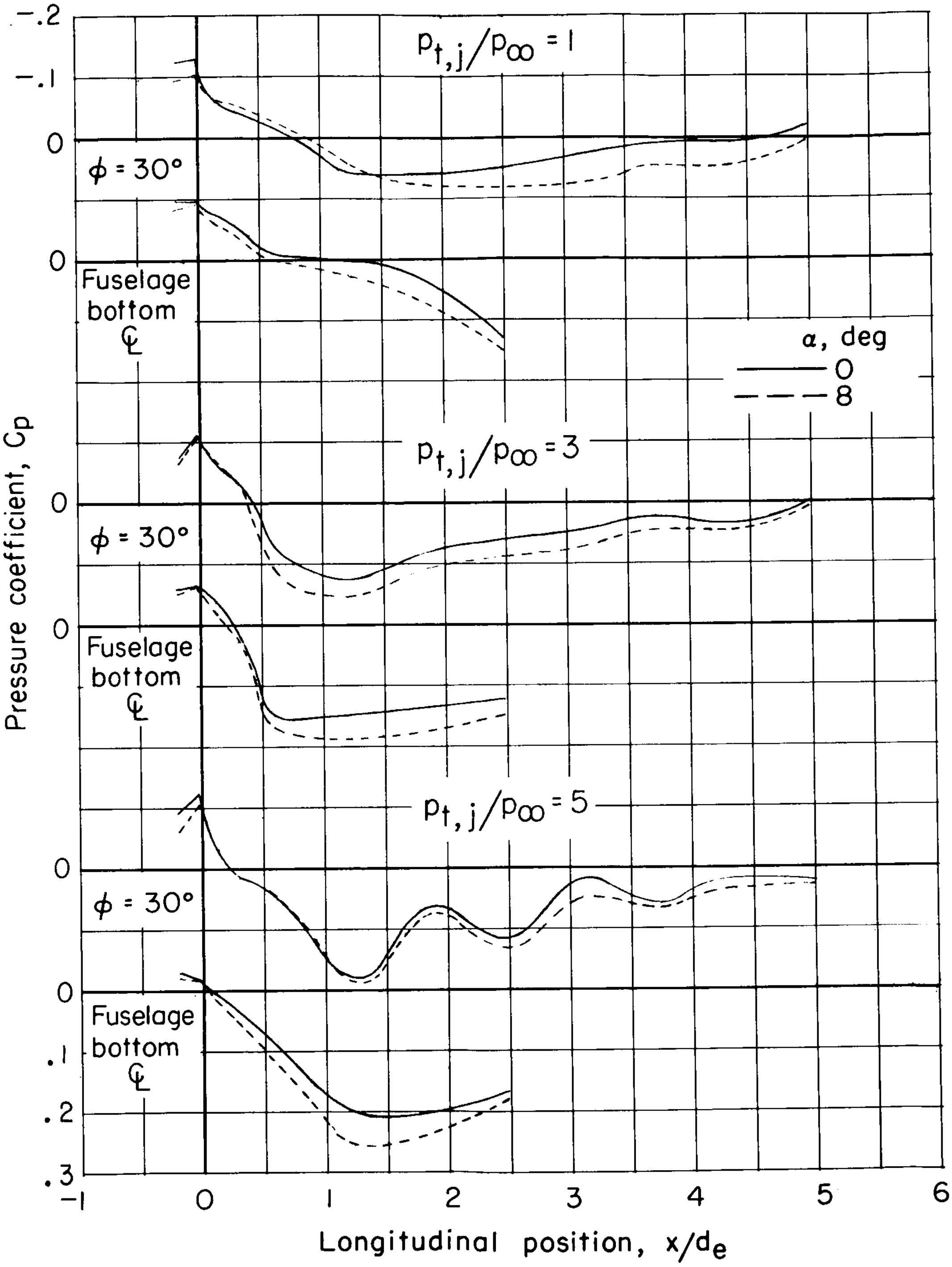

Figure 16.- Effect of angle of attack on the afterbody pressure distributions of configuration III. $M_\infty = 0.85$.

[redacted]

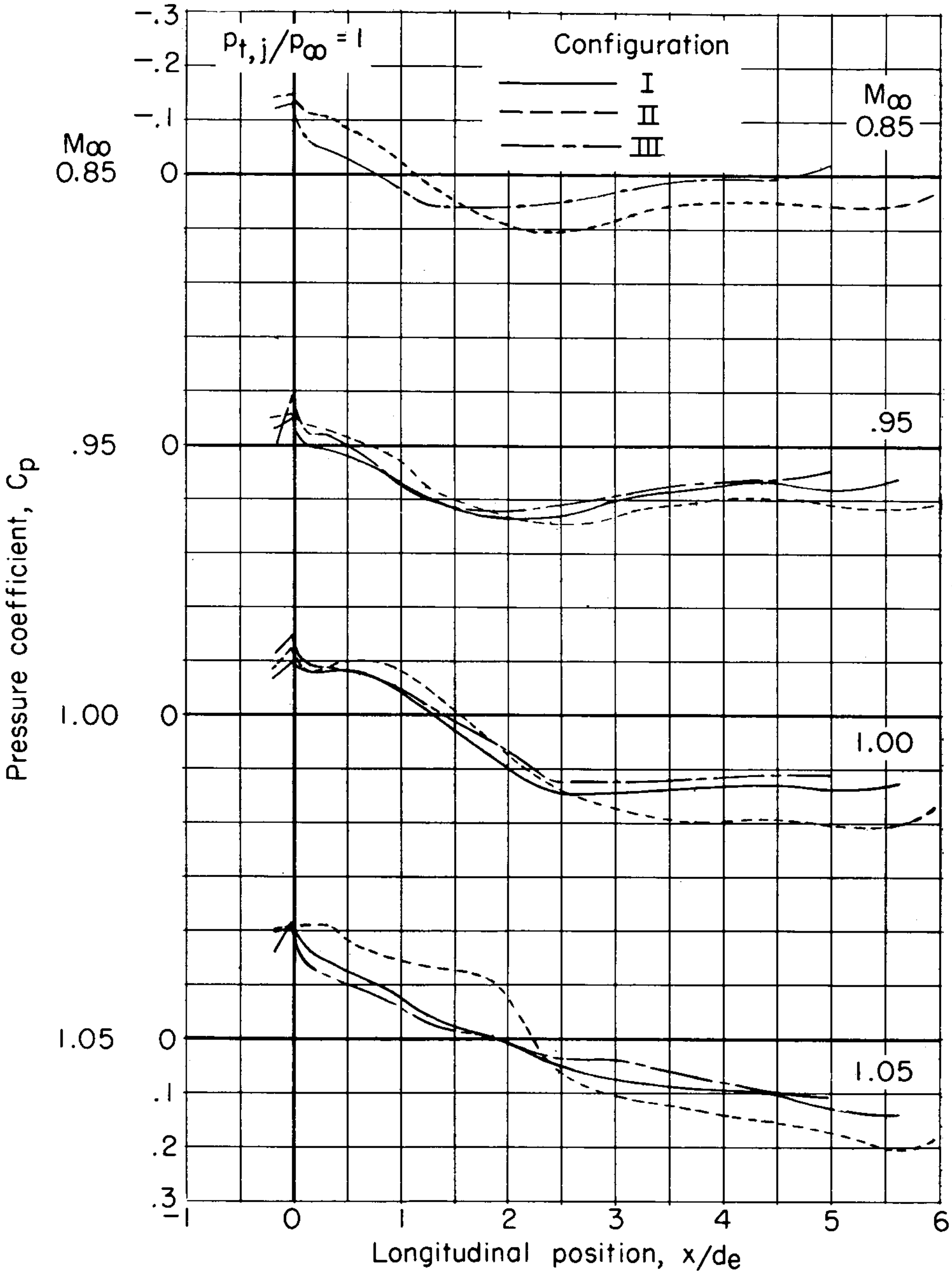

(a) $\frac{p_{t,j}}{p_\infty} = 1$.

Figure 17.- Comparison of afterbody pressures for three model configurations investigated, showing effect of geometry modifications. $\phi = 30^\circ$; $\alpha = 0^\circ$.

[redacted]

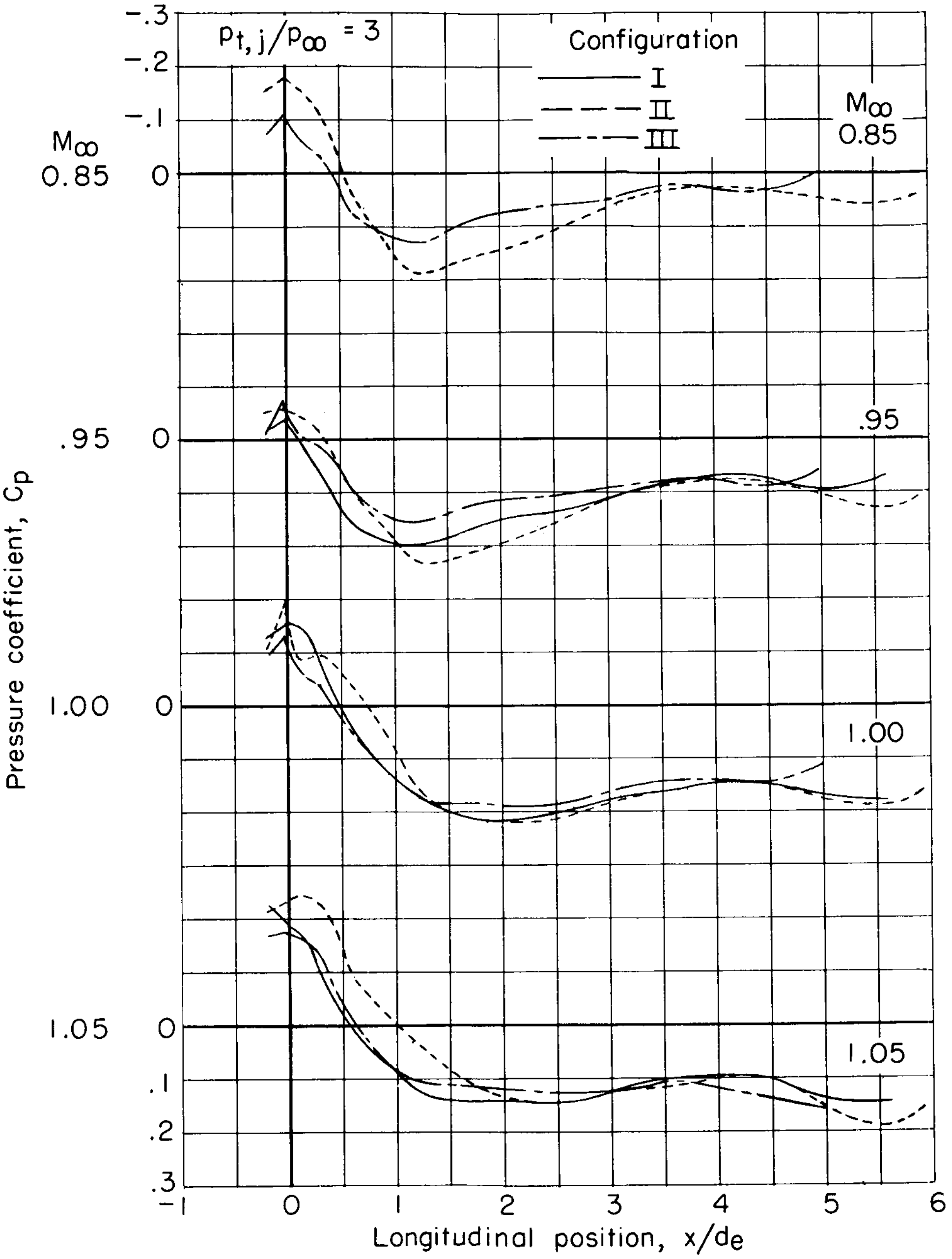

(b) $\frac{p_{t,j}}{p_\infty} = 3.$

Figure 17.- Continued.

[redacted]

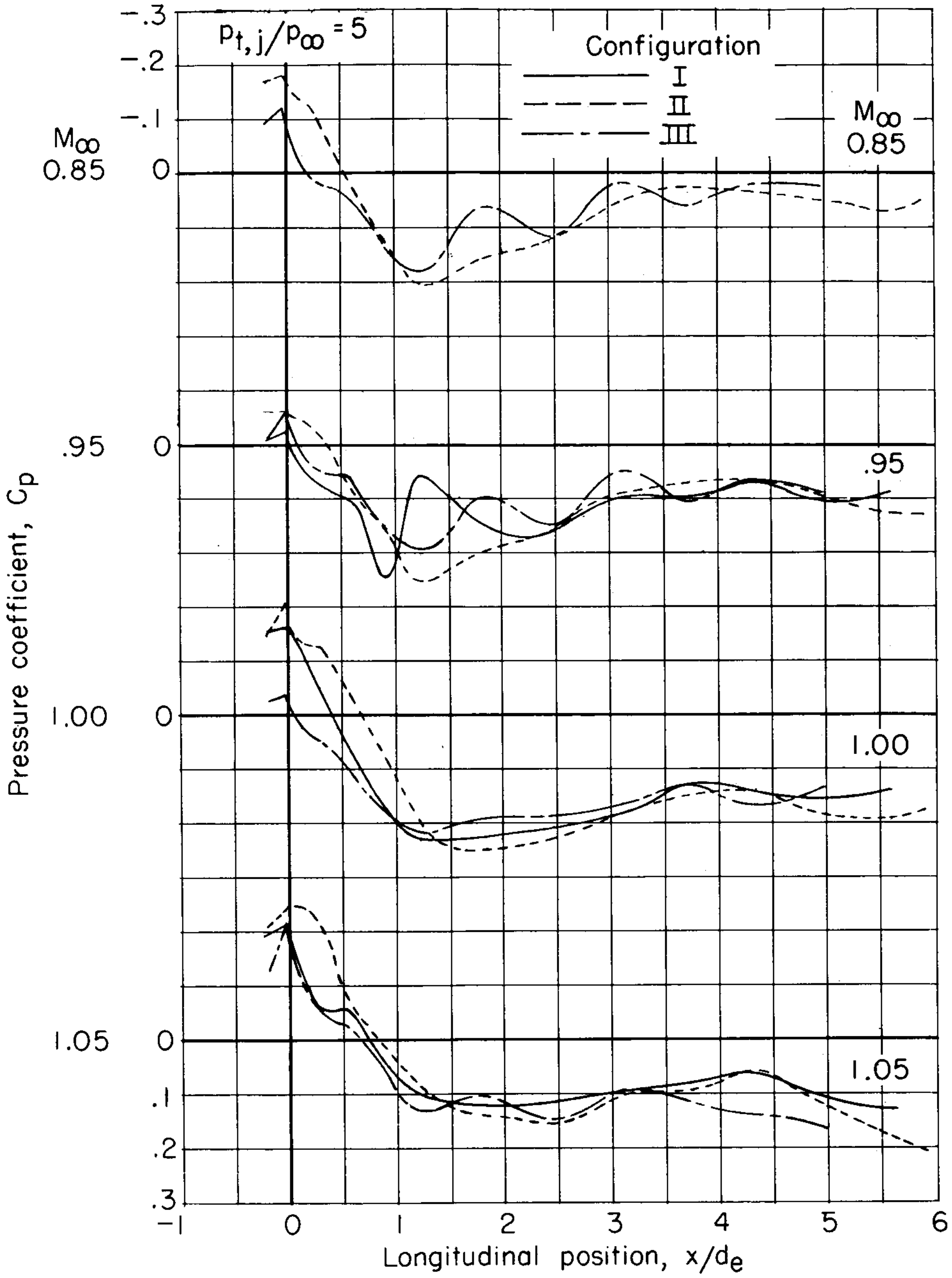

(c) $\frac{p_{t,j}}{p_\infty} = 5.$

Figure 17.- Continued.

[redacted]

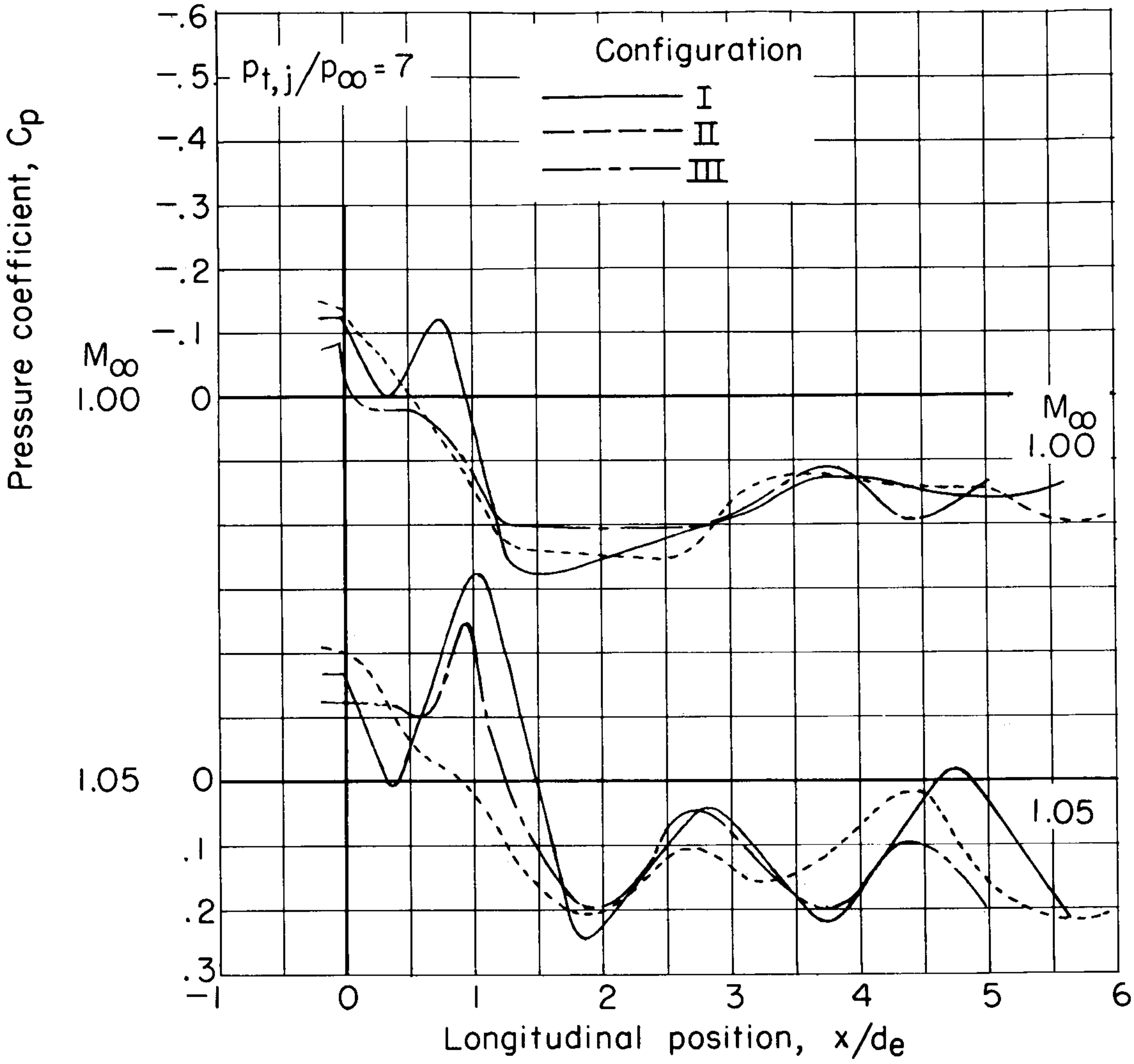

(d) $\frac{p_{t,j}}{p_\infty} = 7.$

Figure 17.- Concluded.

[redacted]

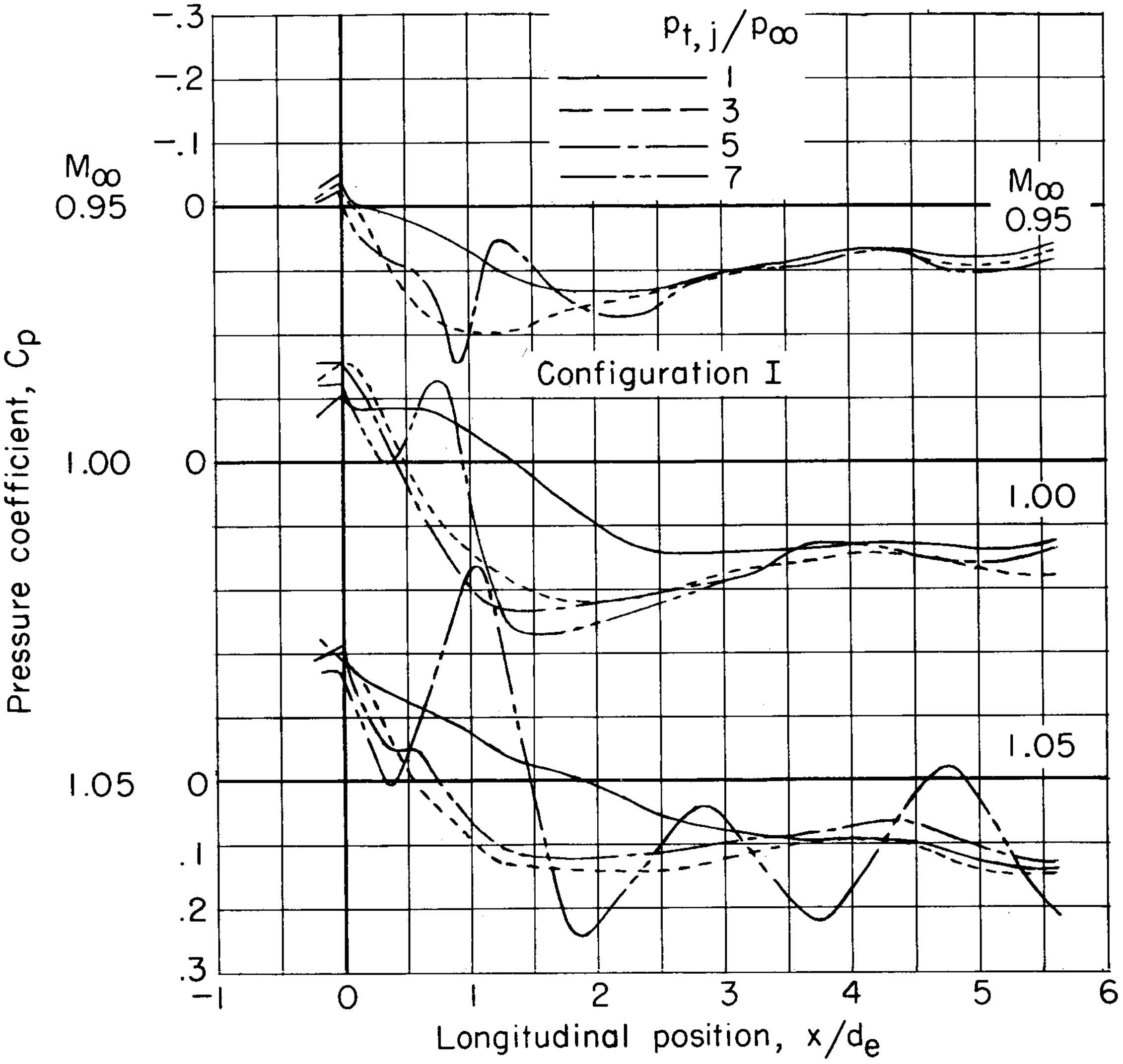

(a) Configuration I.

Figure 18.- Effect of jet pressure ratio on afterbody pressures. $\phi = 30^\circ$; $\alpha = 0^\circ$.

[redacted]

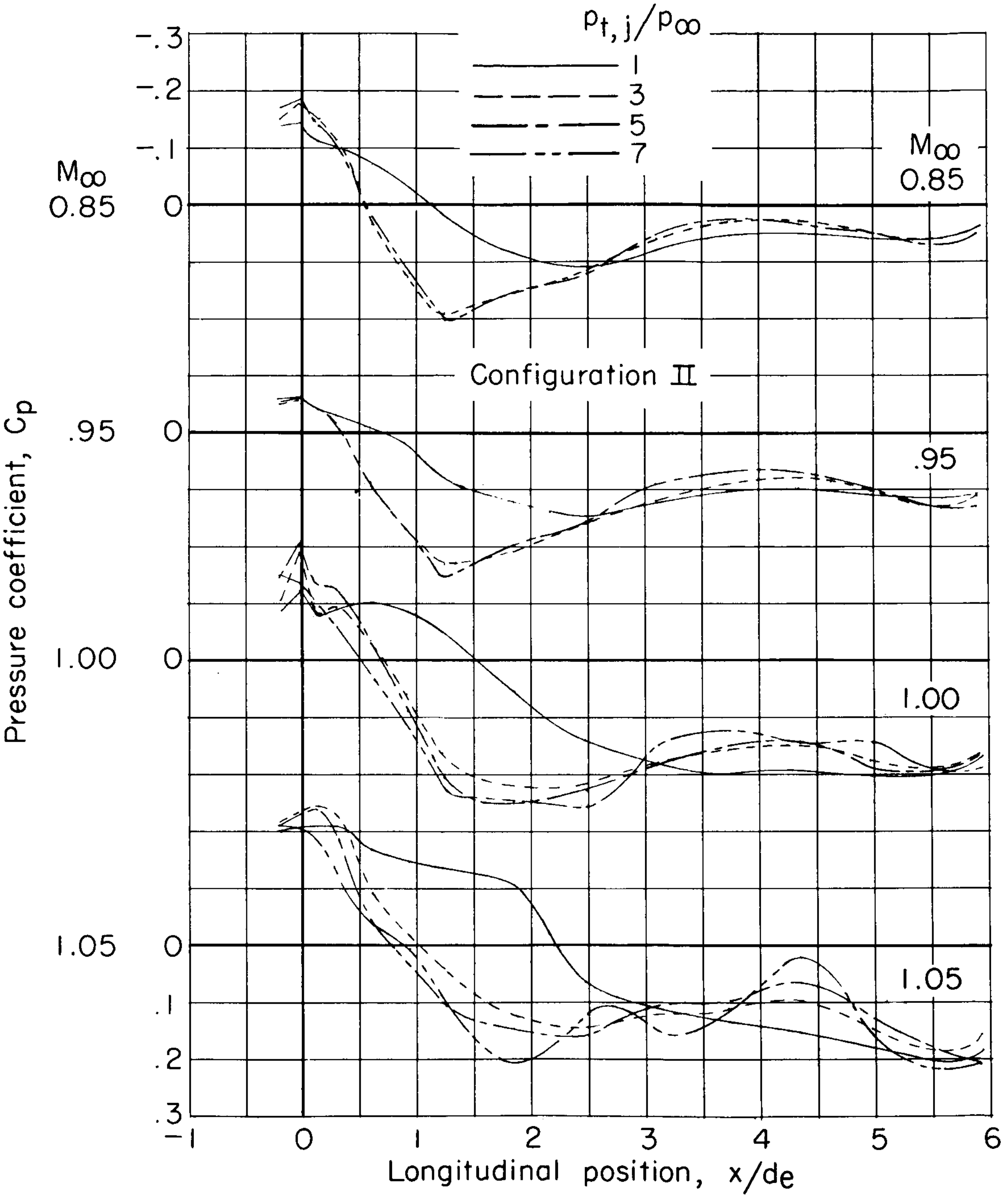

(b) Configuration II.

Figure 18.- Continued.

[redacted]

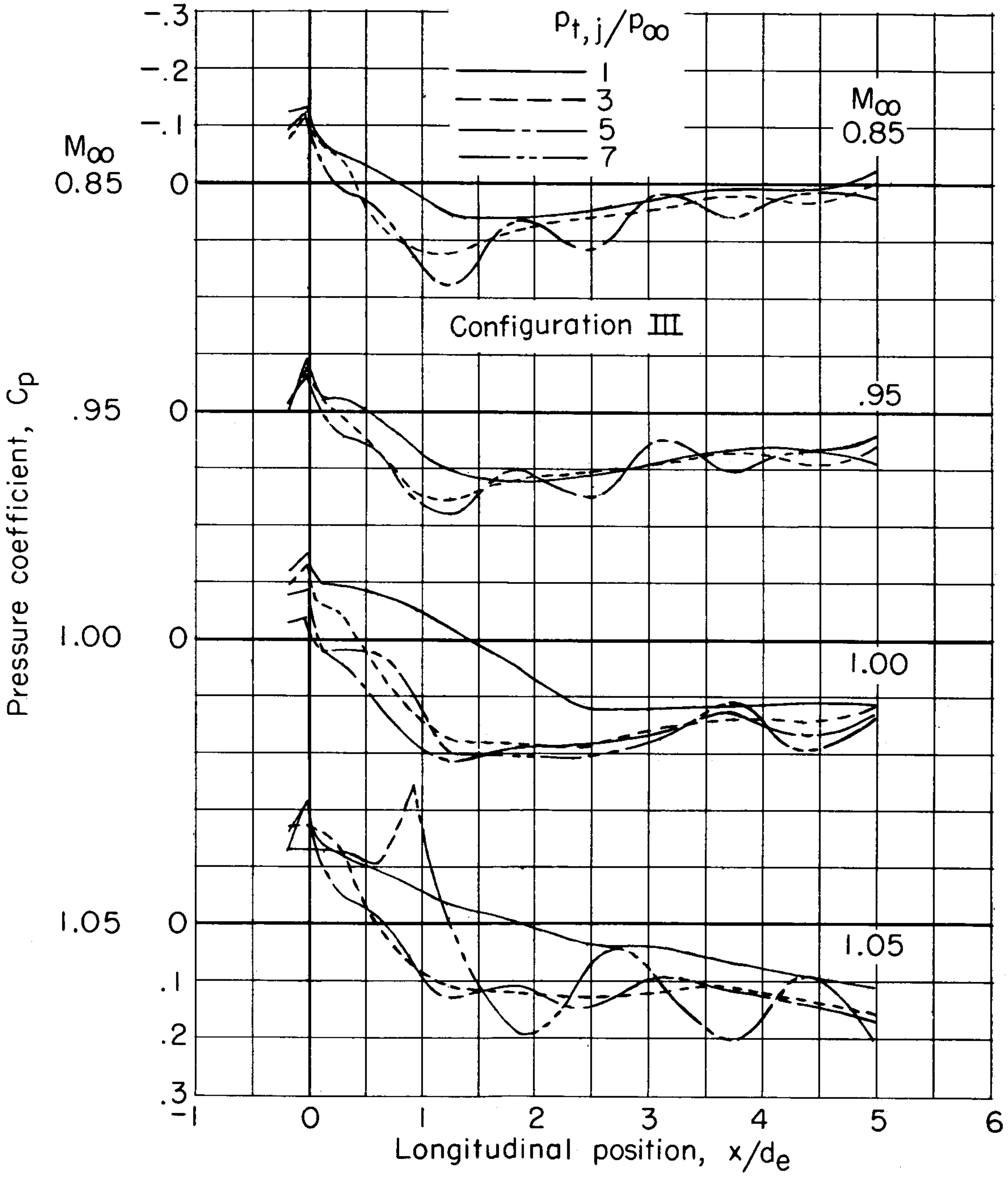

(c) Configuration III.

Figure 18.- Concluded.

[redacted]

UNCLASSIFIED

[redacted]

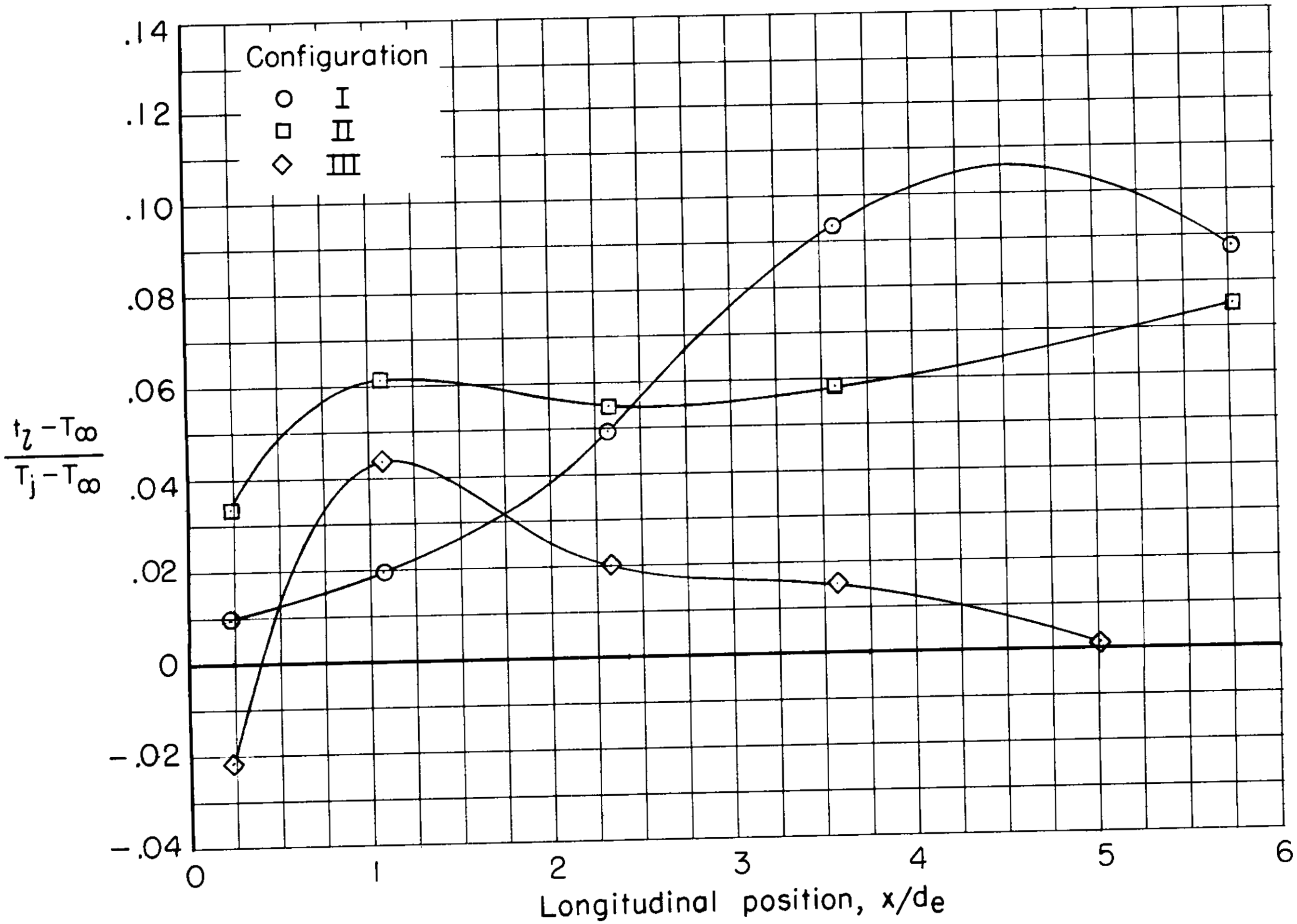

Figure 19.- Temperature parameter variation along row at $\phi = 30^\circ$ of the three different afterbodies. $M_\infty = 0.85$; $\alpha = 4^\circ$; $\frac{p_{t,j}}{p_\infty} = 2.7$.

[redacted]

DECLASSIFIED

[redacted]

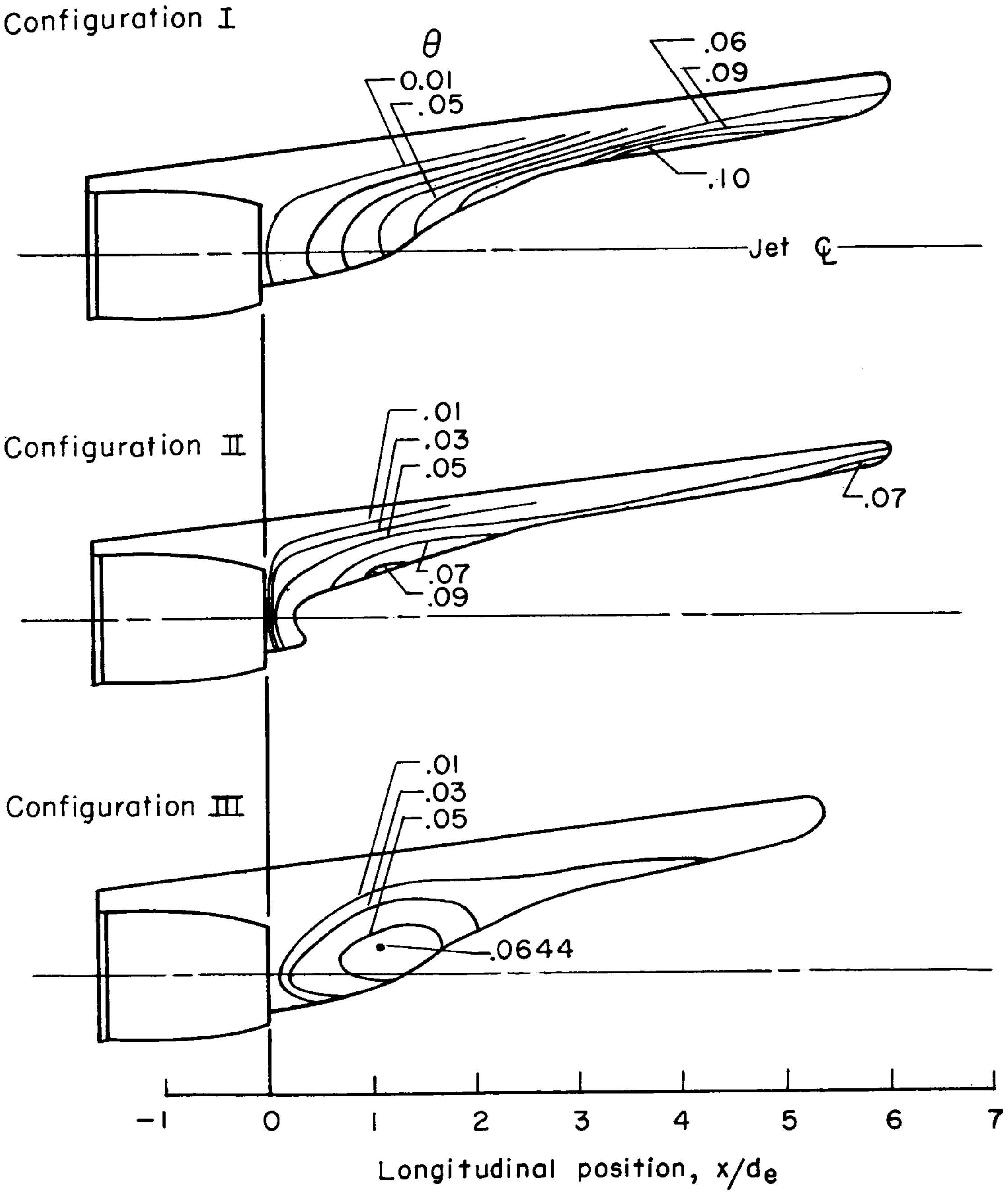

Figure 20.- Afterbody temperature distributions. $M_\infty = 0.85$; $\alpha = 4^\circ$; $\frac{p_{t,j}}{p_\infty} = 2.7$.

[redacted]

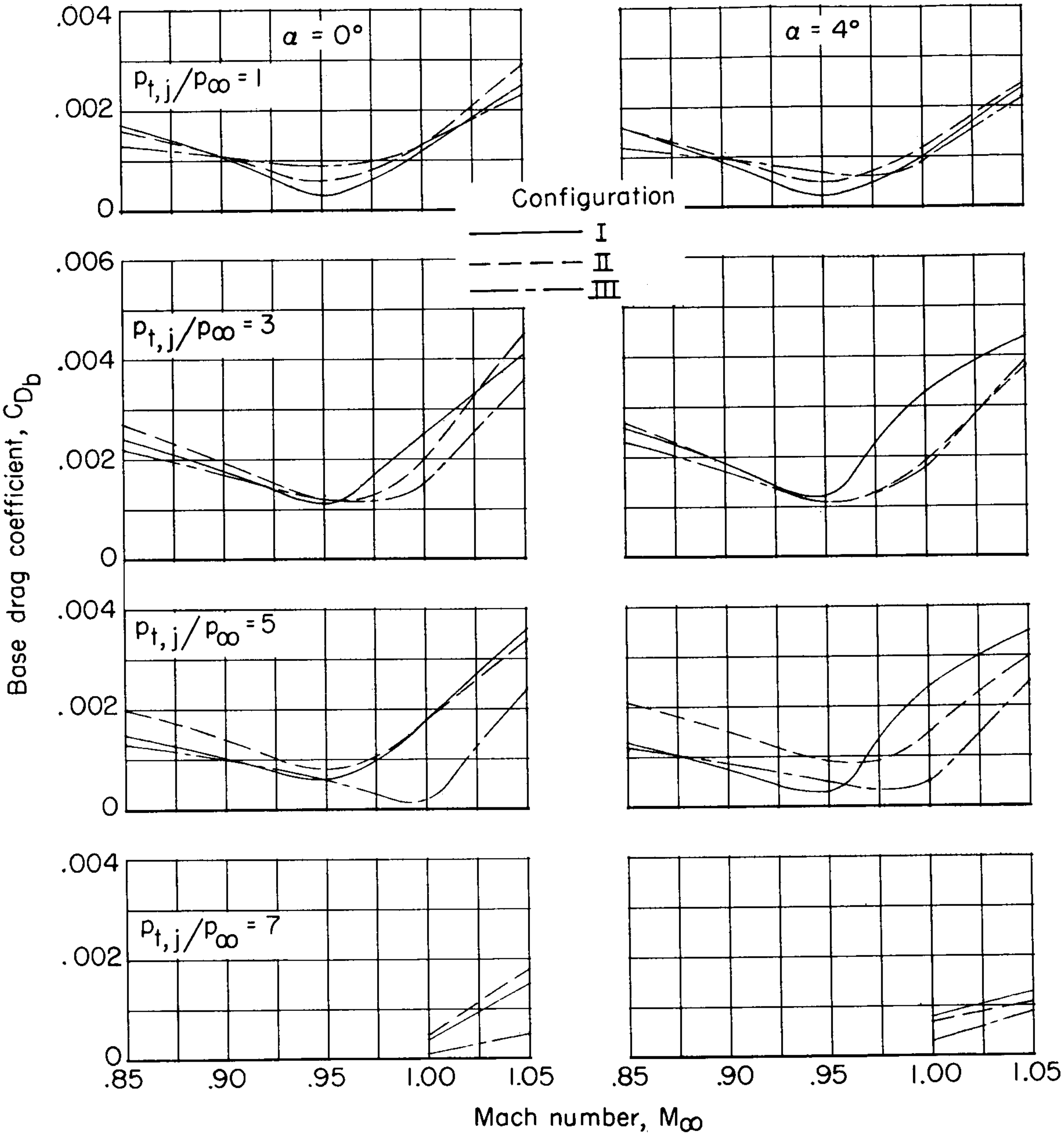

Figure 21.- Effect of model geometry on variation of base drag with Mach number.

[redacted]

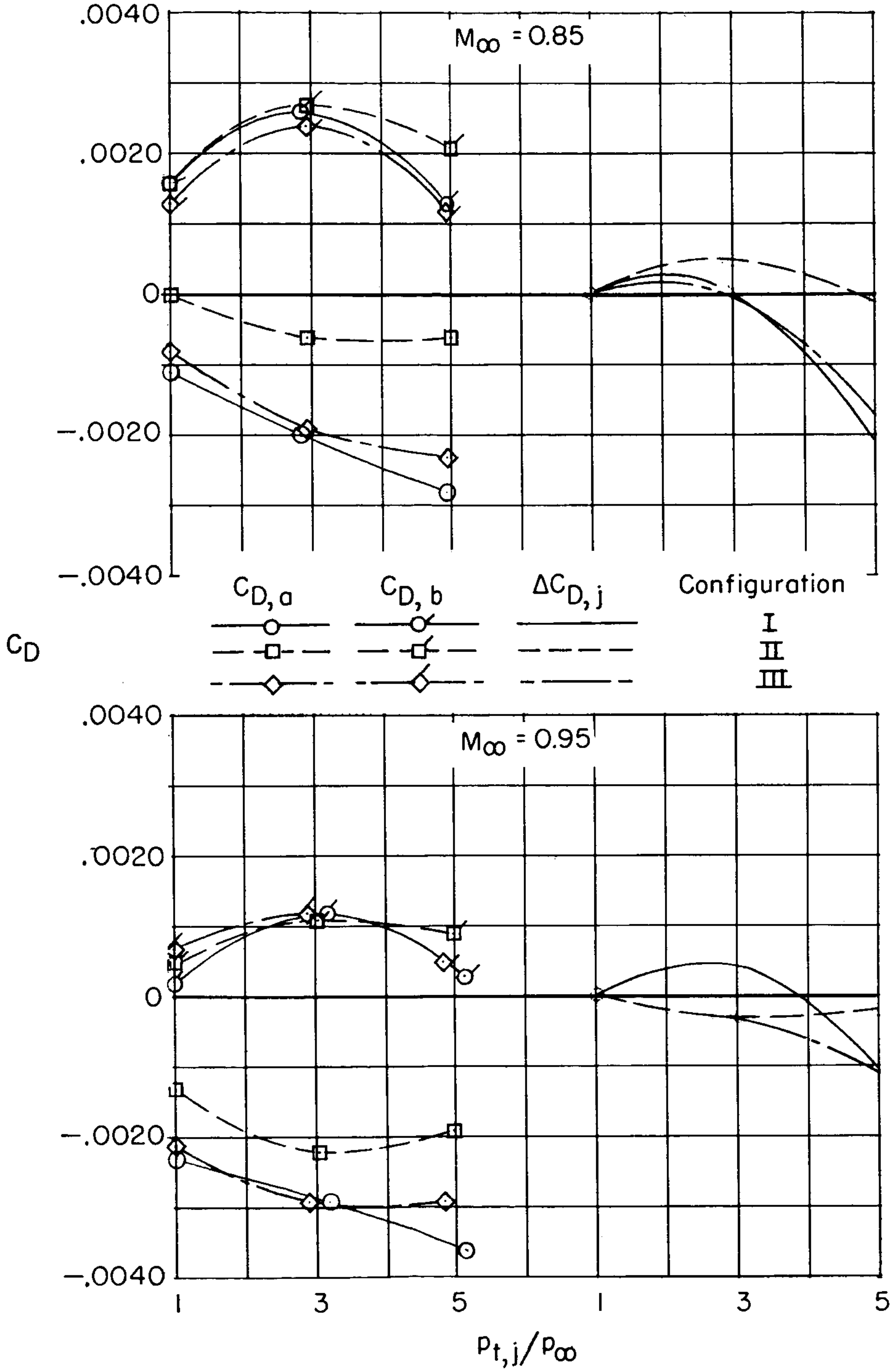

Figure 22.- Variation with jet pressure ratio of base, afterbody, and incremental drag. $\alpha = 4^\circ$.

[redacted]

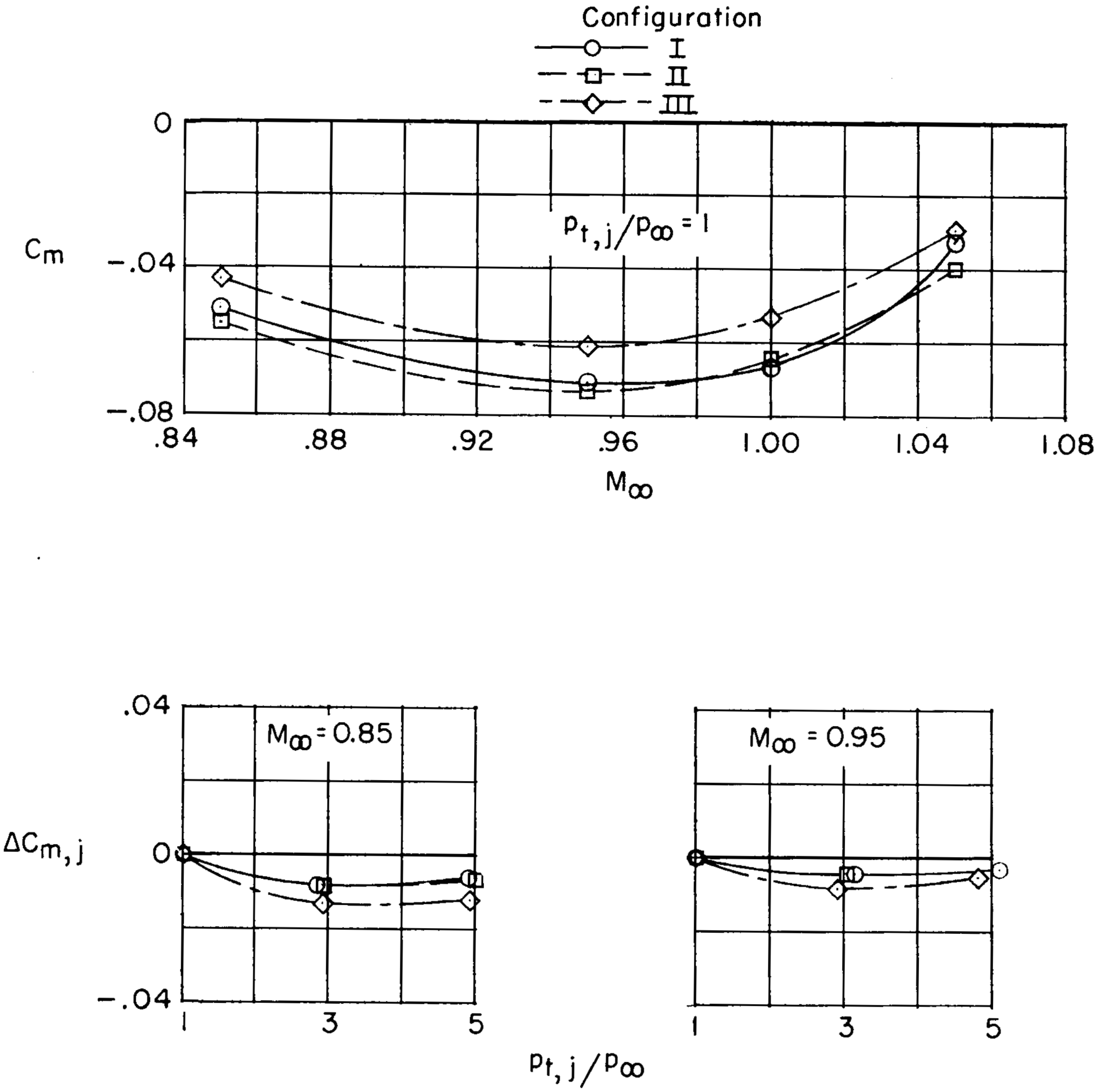

Figure 23.- Effect of configuration geometry on variation of fuselage-tail pitching-moment coefficient with Mach number and jet pressure ratio. $\alpha = 4^\circ$.

[redacted]

NASA - Langley Field, Va. L-112